University of Maribor Press

ISSN 1854-0171

ACTA GEOTECHNICA SLOVENICA

VOL. 19
2022/1

ACTA GEOTECHNICA SLOVENICA

ISSN: 1854-0171

Ustanovitelji — Founders

Univerza v Mariboru, Fakulteta za gradbeništvo, prometno inženirstvo in arhitekturo
University of Maribor, Faculty of Civil Engineering, Transportation Engineering and Architecture

Univerza v Ljubljani, Fakulteta za gradbeništvo in geodezijo
University of Ljubljana, Faculty of Civil and Geodetic Engineering

Univerza v Ljubljani, Naravoslovnotehniška fakulteta
University of Ljubljana, Faculty of Natural Sciences and Engineering

Slovensko geotehniško društvo
Slovenian Geotechnical Society

Društvo za podzemne in geotehniške konstrukcije
Society for Underground and Geotechnical Constructions

Izdajatelj — Publisher

Univerza v Mariboru, Fakulteta za gradbeništvo, prometno inženirstvo in arhitekturo
Faculty of Civil Engineering, Transportation Engineering and Architecture

Naklada — Circulation

200 izvodov - issues

Cena — Price

25 EUR/letnik - 25 EUR/vol.; (50 EUR for institutions/za institucije)

Tisk — Print

Design Studio d.o.o.

Revija redno izhaja dvakrat letno. Članki v reviji so recenzirani s strani priznanih mednarodnih strokovnjakov. Baze podatkov v katerih je revija indeksirana: SCIE - Science Citation Index Expanded, JCR – Journal Citation Reports / Science Edition, ICONDA - The international Construction database, GeoRef. Izid publikacije je finančno podprla Javna agencija za raziskovalno dejavnost Republike Slovenije iz naslova razpisa za sofinanciranje domačih periodičnih publikacij.

Založnik — Published by

Univerzitetna založba Univerze v Mariboru	University of Maribor Press
Slomškov trg 15, 2000 Maribor, Slovenija	Slomškov trg 15, 2000 Maribor, Slovenia
e-pošta: zalozba@um.si, http://press.um.si/, http://journals.um.si/	e-mail: zalozba@um.si, http://press.um.si/, http://journals.um.si/

Naslov uredništva — Address

ACTA GEOTECHNICA SLOVENICA
Univerza v Mariboru, Fakulteta za gradbeništvo, prometno inženirstvo in arhitekturo
Smetanova ulica 17, 2000 Maribor, Slovenija
Telefon / Telephone: +386 (0)2 22 94 300
Faks / Fax: +386 (0)2 25 24 179
E-pošta / E-mail: ags@um.si

Spletni naslov — web Address

http://www.fg.uni-mb.si/journal-ags/

The journal is published twice a year. Papers are peer reviewed by renowned international experts. Indexation data bases of the journal: SCIE - Science Citation Index Expanded, JCR – Journal Citation Reports / Science Edition, ICONDA- The international Construction database, GeoRef. The publication was financially supported by Slovenian Research Agency according to the Tender for co-financing of domestic periodicals.

ANALYSIS OF THE PILE SPACING AND EARTH PRESSURE OF SHEET PILE WALLS BASED ON THE SPATIAL SOIL ARCHING MODEL

ANALIZA RAZMIKA MED PILOTI IZ ZAGATNIC IN ZEMELJSKEGA TLAKA NA PODLAGI MODELA ZEMLJINSKEGA PROSTORSKEGA LOČNEGA UČINKA

Hongbo Zhang
Shandong University,
School of Qilu Transportation
Jinan 250061, P.R. China
E-mail: zhanghongbo@sdu.edu.cn

Mingpeng Liu
Shandong University,
School of Qilu Transportation
Jinan 250061, P.R. China
E-mail: 1398404100@qq.com

Zhikun Liu
Shandong University,
School of Qilu Transportation
Jinan 250061, P.R. China
E-mail: 1392738429@qq.com

Xiaoliang Li
Shandong Hi-Speed Group Co., Ltd.
Jinan 250101, P.R. China
E-mail: lixiaoliang_sd@163.com

Xiaowei Liu
Shandong Provincial Communications Planning and Design Institute Co., Ltd.
Jinan 250031, P.R. China
E-mail: liuxiaowei_sdh@163.com

Jianqing Wu *(corresponding author)*
Shandong University,
School of Qilu Transportation
Jinan 250061, P.R. China
E-mail: jianqingwusdu@sdu.edu.cn

Xiuguang Song
Shandong University,
School of Qilu Transportation
Jinan 250061, P.R. China
E-mail: songxiuguang@sdu.edu.cn

DOI https://doi.org/10.18690/actageotechslov.19.1.2-16.2022

Keywords

soil arching effect, spatial soil arching model, pile spacing, earth pressure, sheet pile walls

Abstract

Soil arching effect is an important premise for which sheet pile walls can exert strong retaining abilities. It has previously been found that the spacing of the piles and the earth pressure are two important factors to consider in the designing of sheet pile walls and are closely related to the soil arching effect. This research proposed a spatial soil arching model according to the limit equilibrium theory and soil yielding criterion. An innovative method of pile spacing calculation was developed based on the proposed model. In addition, when cohesion was considered in the proposed spatial soil arching model, it was observed that the current method for earth pressure estimation on retaining plate

Ključne besede

ločni učinek tal, prostorski zemljinski model ločnega učinka, razmik pilotov, zemeljski tlak, piloti iz zagatnic

Izvleček

Zemljinski ločni učinek v tleh je pomembna predpostavka, pri kateri lahko piloti iz zagatnic izkazujejo močno sposobnost podpiranja. Predhodno so ugotovili, da sta razmik pilotov in zemeljski tlak dva pomembna dejavnika, ki ju je treba upoštevati pri načrtovanju pilotov iz zagatnic in sta tesno povezana z zemljinskim ločnim učinkom. V tej raziskavi je bil predlagan model zemljinskega prostorskega ločnega učinka po teoriji mejnega ravnovesja in kriteriju plastifikacije zemljine. Na podlagi predlaganega modela je bila razvita inovativna metoda izračuna razmika pilotov iz zagatnic. Ugotovljeno je bilo, da je, ob upoštevanju kohezije v predlaganem modelu zemljinskega prostorskega ločnega učinka, *was also improved. Finally, the stability status of the soil between the piles was analyzed based on this study's spatial soil arching model. It was found that when compared to the previous methods, the proposed method had made fewer assumptions and conformed better in practice.*

bila izboljšana tudi veljavna metoda za oceno zemeljskega tlaka na pritrdilni plošči. Na koncu te študije je bilo analizirano stanje stabilnosti zemljine med piloti iz zagatnic na podlagi modela zemljinskega prostorskega ločnega učinka. Ugotovljeno je bilo, da je potrebno v predlagani metodi v primerjavi s prejšnjimi metodami podati manj predpostavk in, da se rezultati bolje ujemajo z obnašanjem v praksi.

Symbol table

A	=	the area of the enclosed section ABCDE
a	=	the length of pile section
B	=	the length of semi-axis along Y direction
b	=	pile width
C	=	parameter
c	=	cohesion
d_z	=	micro-segment depth
F_N	=	the axis force in the arch foot
$f(z)$	=	the rise of soil arching
I_1	=	first invariant of stress tensor
J_2	=	second invariant of stress deviation
K_0	=	stationary earth pressure coefficient
k	=	parameter in Druker-Prager yield criterion
L	=	reasonable pile space
l	=	net distance of adjacent piles
P_1	=	the perimeter of the section BCD
P	=	the perimeter of the enclosed section ABCDE
$q(z)$	=	landslide thrust density
q'	=	the horizontal thrust on the middle wall
R_x	=	the reactive force acting on arch foot in X direction
R_y	=	the reactive force acting on arch foot in Y direction
$S(z)$	=	failure discriminant function
T	=	the axial force at the arch apex
t	=	the thickness of soil arch
z	=	depth
z_0	=	critical depth
α	=	parameter in Druker-Prager yield criterion
β	=	parameter, $\beta = 45° - \theta + \varphi/2$
γ	=	soil weight
δ	=	the friction angle between the wall back and soil
ζ	=	the coefficient of cohesion reduction
θ	=	the angle between axis at the arch foot and horizontal direction
θ_σ	=	stress Lode angle
λ	=	lateral pressure coefficient
σ_A	=	axis stress of point A
σ_B	=	axis stress of point B
σ_x	=	soil-pile reaction stress
σ_y	=	horizontal thrust of the soil inner the soil arching
σ_z	=	vertical thrust
ν	=	Poisson ratio
φ	=	friction angle

1 INTRODUCTION

Sheet pile walls have been widely used as continuous retaining structures in landslide control, excavation, and high fill subgrade processes [1]. In sheet pile wall designs, the pile spacing and earth pressure on the retaining plates are considered to be two important factors. For example, too large pile spacing can cause the collapse of soil between the piles. Meanwhile, material may be wasted if the spaces between the piles are too small. Therefore, a very important problem for engineers is how to select a reasonable pile spacing. The current designing methods are more dependent on experience and still lack a theoretical basis [2]. As for the earth pressure, there are mainly three methods currently used to determine earth pressure on retaining plates [2]: Classical earth pressure theory; simplified granary method; and the unloading arch theory. However, no uniform agreement has been reached regarding the performances of those three methods. The effects of pile spacing and earth pressure on retaining plates are closely related to soil arching effects. Furthermore, among the known influencing factors of pile spacing and earth pressure on sheet pile walls, soil arching effect has been proven to be very important [3].

Soil arching effects are widespread in the field of geotechnical engineering. Terzaghi [4] first verified the existence of soil arching using a trap-door test and defined it as the phenomenon of stress transformation from the yielding soil to the stationary soil. In another related study, Handy [5] found that soil arching was essentially the trajectory of minor principal stress within the soil. Dalvi and Prise [6] reported that soil arching was chain-shaped along the direction of major principal stress when the soil was in passive state. In addition, Bosscher and Gray [7], Wang and Yen [8] and Adachi et al. [9] verified the existence of soil arching effects between piles. Some previous studies (Zhao et al. [10]; Pardo and Sáez [11]; Ausilio et al. [12]) have also pointed out that the main contributions of piles are related to their supporting abilities when faced with soil arching effect. The soil arching effect produced by pile-soil reactions can effectively mobilize the soil strength and redistribute the stress. The premise for piles to exert supporting abilities when soil arching occurs includes the transference of the landslide thrust into the pile bodies and then delivering the stress to underground regions. The factors which are known to influence soil arching effects behind piles include the pile spacing, which have been proven to be very important (Li et al. [13]). Soil arching effects can also heavily influence the earth pressure on the retaining plates (Dong [14]).

By analyzing the relationships be soil arching effect and pile spacing, a large number of previous studies (Chen and Martin [15]; Liang and Yamin [16]; Şahin [17]; Yamin [18]) found that appropriate spacing of the piles was essential to the formation of soil arching effect. It was observed that when the pile spacing became larger, the piles could not take advantage of the soil arching effects and became unable to effectively control slope sliding. He et al. [19] also found observed this phenomenon using numerical simulations and pointed out when the pile spacings were 2 to 6 times the pile widths, soil arching effect could be fully exerted. In addition, based on the analyses of soil arching effect, methods were developed to calculate reasonable pile spacing. Some researchers (Chen et al. [20] Jiang et al. [21]; Wu et al. [22]; Qiu et al. [23]) hypothesized that the pile-end soil arching or the friction soil arching bears all the thrust. Therefore, reasonable pile spacing could be determined according to Mohr-Coulomb strength criterion. In another related study, as derived from soil mechanics and elastic theories, Li et al. [24] established a soil arching model and the maximum pile spacing was proposed according to the Mohr-Coulomb criterion. Also, Zhang et al. [25] deduced a novel method of calculating the maximum and minimum pile spacing which considered the soil arching effect. However, the aforementioned calculation models mainly regarded the soil arching model as a plane strain problem and assumed that the soil arching effect was infinitely distributed along pile depths. Moreover, the classic soil pressure theory, unloading arch theory, and simplified granary method, which are the primary methods used to calculate the earth pressure on retaining plates, are all plane strain models.

However, Eskisar et al. [26], Risio et al. [27], and Vermeer et al. [28] found that the soil arching behind piles presented variations along the depth. Therefore, the plane-strain models of pile space calculations were determined to be unsuitable, and the scope of their applications were also very limited. Zhang et al. [29] assumed that the shape of soil arching was parabola and established a spatial soil arching model to calculate reasonable pile spacing. However, that study could not successfully satisfy the limit equilibrium theory. Furthermore, Zhang et al. [3] pointed out that the shape of soil arching should not be parabolic. Li et al. [30] presented a flattened ellipsoid model in order to describe the three-dimensional characteristics of sliding mass for colluvial landslides and also proposed a formula to determine effective pile spacing. However, his research neglected to explore the factor of soil mass yielding. Huang et al. [31] determined that the earth pressure calculated using the unloading arch theory and the simplified granary method was greater than the obtained measured values. In summary, the above-mentioned studies showed that there was a lack of effective models for the calculations of pile spacing and earth pressure on retaining plates. Therefore, establishing an effective spatial soil arching model was considered to be very essential.

In this study, a spatial soil arching model was developed based on the limited equilibrium theory. A calculation method for reasonable pile spacing and earth pressure on sheet pile walls was established based on a spatial soil arching model. Due to the complexity of the formulas, a set of Matlab programming was also employed to deter-

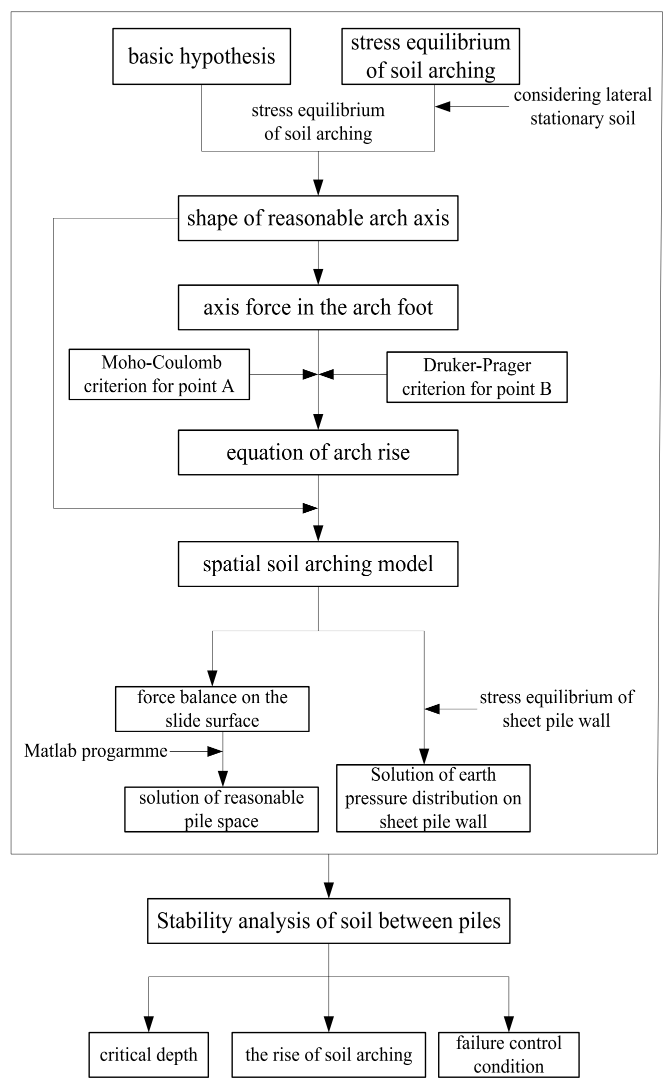

Figure 1. Flow chart of the derivation of the equations.

mine the numerical solutions of the those equations. Finally, the rationality of the model was verified by a case study, and the stability of the soil between the piles was analyzed according to the proposed spatial soil arching model. It was found that when compared with previous methods, the proposed method made fewer assumptions and conformed better in practice. In order to illustrate the logic of the derivation of the equations in this paper, this study's flow chart is detailed in Figure 1.

2 CALCULATION MODEL

2.1 Basic hypothesis

In this research investigation, rectangular-section piles were chosen as the basic scenario since they are widely used in support engineering projects. The other-type sections were equivalent to rectangle sections. Many previous studies have proposed that landslide thrust is simultaneously supported by both end-bearing soil arching and friction soil arching (Wu et al. [22]; Qiu et al. [23]). However, it has been observed that the bearing capacities of friction arches are quite small when compared to end-bearing arches (Yang et al. [32]). Moreover, based on the mechanics principle, friction arching does not directly undertake landslide thrust and its force is the smaller principal stress of end-bearing arching. Therefore, it has been concluded that friction soil arching makes little contribution to the stability of the soil between piles. In practical projects, the soil between the piles can be easily destroyed. However, the soil outside the arch-shape zone usually remains stable, as shown in Figure 2. Therefore, based on the aforementioned findings, it is reasonable and safe to ignore friction soil archings. The following hypotheses were made in this study:

1) Small deformation hypothesis;
2) End-bearing soil arching is considered but friction soil arching between the piles is ignored;

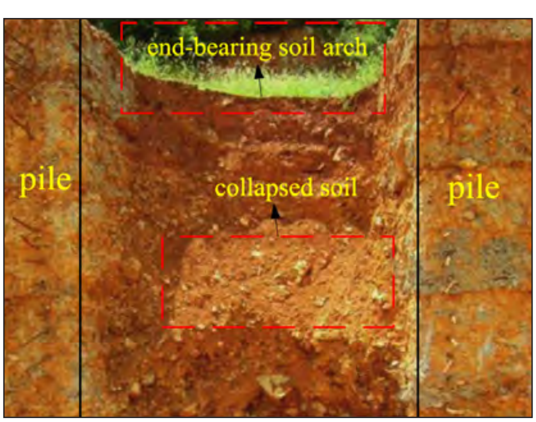

Figure 2. Destruction of the soil between the piles.

3) The axial stress on the reasonable arch axis is the direction of the major principal stress, and there is no shear stress or tensile stress perpendicular to the plane of the reasonable arch axis;
4) The soil reaching yield state is considered to be the destruction of the soil.

2.2 Mechanical analysis of the soil arching

A sketch map of the piles and the end-bearing soil arching is shown in Figure 3. In the figure, the parameters b and l are defined as the width of pile and the net distance of adjacent piles, respectively. The stationary soil behind the piles, which produced lateral earth pressure for the soil arching, was also considered.

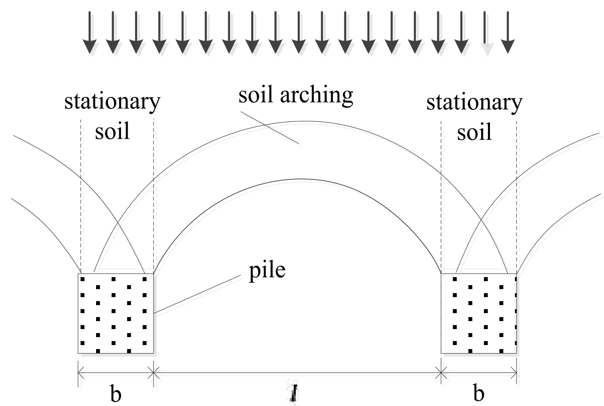

Figure 3. Schematic diagram of the end-bearing soil arching.

A stress diagram of the soil arching and coordinate schematic is presented in Figure 4.

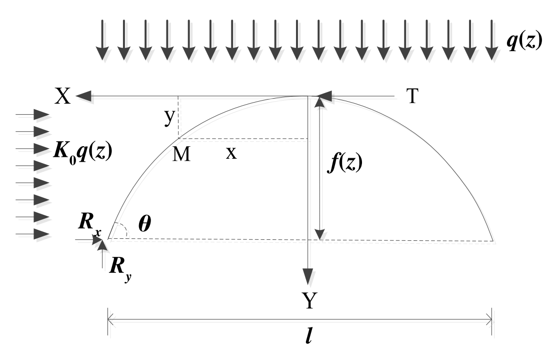

Figure 4. Stress diagram of the soil arching.

Based on the above-mentioned hypotheses, soil arching is subjected to the landslide thrust density $q(z)$ which is distributed uniformly on the arch. Generally speaking, $q(z)$ varies along with depth. The stationary soil behind the piles then produces lateral earth pressure $K_0q(z)$, where K_0 is the stationary earth pressure coefficient and is expressed as $K_0 = v/(1 - v)$; v is the Poisson ratio; and K_0 could be approximately determined by $K_0 \approx 1 - \sin\varphi$. Also, the lateral earth pressure will be uniformly distributed along the side of the soil arch. For analysis convenience, a coordinate system with the apex as the coordinate origin was established. The reactive force acting on the arch foot in the X and Y direction were R_x and R_y , respectively. The axial force at the arch apex was T. The rise of the soil arching was denoted as $f(z)$, which was a function varied with depth z. The left semi-arch was selected for this study's mechanical analysis. As a result, the equilibrium equation along the X direction was as follows:

$$K_0 q(z) f(z) + R_x = T \qquad (1)$$

Then, considering the force balance along the Y direction of the entire left semi-arch, the following equation was obtained:

$$R_y = \frac{q(z)l}{2} \qquad (2)$$

Subsequently, according to the moment balance of the arch apex, Eq. (3) can be obtained:

$$R_x f(z) - R_y \frac{l}{2} + \frac{K_0 q(z) f^2(z)}{2} + \frac{q(z) l^2}{8} = 0 \qquad (3)$$

For an arbitrary point M, the following equation could be acquired according to the moment balance:

$$\frac{q(z)x^2}{2} + \frac{K_0 q(z) y^2}{2} - Ty = 0 \qquad (4)$$

Therefore, by substituting Eqs. (1), (2), (3) into Eq. (4), Eq. (5) was obtained:

$$\frac{x^2}{\left(B\sqrt{K_0}\right)^2} + \frac{(y-B)^2}{B^2} = 1 \qquad (5)$$

Where

$$B = \frac{f(z)}{2} + \frac{l^2}{8 f(z) K_0} \qquad (6)$$

Eq. (5) indicates that the shape of reasonable arch axis can form part of the elliptic curve at any depth. The length of the semi-axis in the X direction is $B\sqrt{K_0}$, while the length of the semi-axis along Y direction is B. It was obvious that the parameter B was the function of $f(z)$. Therefore, the shape of the soil arching varied with the depth of the ground. It was concluded that the soil arching of the piles was actually a three-dimensional problem rather than a plane strain problem.

2.3 Yielding criterion of the soil arching

According to the mechanical features of the arches, the axial stress at the arch foot will be higher than that of the arch apex. Therefore, the soil in the arch foot can yield preceding to the arch apex. As a result, the stress conditions at arch foot should be considered while that at the arch apex can be neglected. A diagram of the axis force in an arch foot at any depth is detailed in Figure 5. In the figure, the thickness of soil arch is marked as t; the angle between the axis at the arch foot and horizontal direction is noted as θ. As a result, $\tan\theta$ and the axis force F_N in the arch foot at any depth can be written as follows:

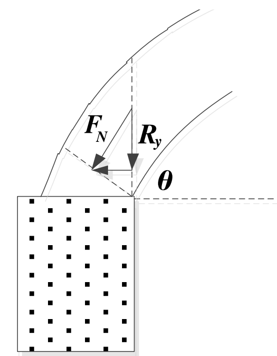

Figure 5. Axial force in an arch foot at any depth.

$$\tan\theta = \left.\frac{dy}{dx}\right|_{x=\frac{l}{2}, y=f(z)} = \left.-\frac{x}{K_0(y-B)}\right|_{x=\frac{l}{2}, y=f(z)} = \frac{4f(z)l}{l^2 - 4K_0 f^2(z)} \qquad (7)$$

$$\left.F_N\right|_{x=\frac{l}{2}} = \frac{R_y}{\sin\theta} = \frac{q(z)l}{2}\sqrt{1+\left[\frac{l^2 - 4K_0 f^2(z)}{4f(z)l}\right]^2} \qquad (8)$$

The axial force can be regarded as the integral of axial stress along the soil arch thickness. In the figure, the inner-edge point and the outer-edge point of the arch foot are indicated by A and B, respectively. Therefore, according to the limit equilibrium theory, the axis stress of point $A(\sigma_A)$ and point $B(\sigma_B)$ will be generally unequal for their different stress states. For calculation convenience, the

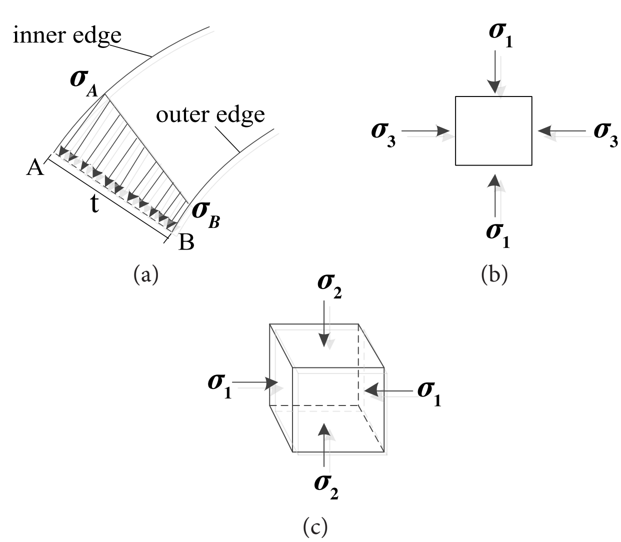

Figure 6. Stress conditions of the soil arch foot:
(a) Distribution of the axial stress; (b) Stress state of Point A;
(c) Stress state of Point B.

distribution of the axis stress from Point A to Point B was assumed to be linear, as presented in Figure 6(a).

Point A was squeezed by surrounding soil and was considered to be within a stable zone. Since Point A directly bore the landslide thrust, this was determined to be the major cause of its yielding, and the influencing effect of gravity could be neglected. The state of Point A was assumed to be a plane stress state, as shown in Figure 6(b). Its minor principal stress was landslide stress $q(z)$ and the major principal stress was arch axis stress σ_A. Therefore, according to the Moho-Coulomb yield criterion, Eq. (9) was obtained as follows:

$$\sigma_A = q(z)\tan^2(45^\circ + \frac{\varphi}{2}) + 2c\tan(45^\circ + \frac{\varphi}{2}) \qquad (9)$$

In regard to Point B, due to the fact that its inner face was a precipitous face, gravity may have also affected the yielding of the soil. Therefore, considering the spatial stress state of Point B, its major principal stress, intermediate principal stress, and minor principal stress were σ_B, γz, and 0, respectively, as shown in Figure 6(c). In the current study, in order to consider the influencing effects of gravity on soil yielding, the Druker-Prager yield criterion was employed for the analysis process as follows:

$$\alpha I_1 - \sqrt{J_2} + k = 0 \qquad (10)$$

Where α and k represent the parameters; I_1 is the first invariant of stress tensor; and J_2 indicates the second invariant of stress deviation. In this investigation, the generalized Mises yield condition was adopted. Therefore, considering the compression failure of the soil, the stress Lode angle was determined to be $\theta_\sigma = -\pi/6$, and the following equations were obtained:

$$\alpha = \frac{2\sin\varphi}{\sqrt{3}(3-\sin\varphi)}, \quad k = \frac{6c\cos\varphi}{\sqrt{3}(3-\sin\varphi)} \qquad (11)$$

$$\begin{cases} I_1 = \sigma_1 + \sigma_2 + \sigma_3 = \sigma_B + \gamma z \\ J_2 = \dfrac{(\sigma_1-\sigma_2)^2 + (\sigma_1-\sigma_3)^2 + (\sigma_2-\sigma_3)^2}{6} = \dfrac{1}{3}[\sigma_B^2 + (\gamma z)^2 - \sigma_B \gamma z] \end{cases} \qquad (12)$$

Then, by substituting Eq. (11) and Eq. (12) into Eq. (10), Eq. (13) could be obtained as follows:

$$\begin{cases} \sigma_B = \dfrac{\gamma z(1+6\alpha^2) + 6\alpha k + \sqrt{3S(z)}}{2(1-3\alpha^2)} \\ S(z) = z^2(12\alpha^2\gamma^2 - \gamma^2) + 12\alpha k\gamma z + 4k^2 \end{cases} \qquad (13)$$

Subsequently, according to the axial force balance at the arch foot, Eq. (14) could be obtained:

$$\frac{\sigma_A + \sigma_B}{2} t = \sigma_N t = F_N \qquad (14)$$

Where σ_N represents the mean axis stress and was expressed as:

$$\sigma_N = \frac{(\sigma_A + \sigma_B)}{2} \qquad (15)$$

2.4 Spatial soil arching model

The thickness of the soil arch was then assumed to be equal to the width of pile b. Therefore, by substituting Eqs. (9), (13), and (14) into Eq. (8), Eq. (16) was obtained:

$$f(z) = \frac{l}{2K_0}\left\{\left[-\sqrt{\left(\frac{2\sigma_N b}{q(z)l}\right)^2 - 1}\right] + \sqrt{\left(\frac{2\sigma_N b}{q(z)l}\right)^2 - 1 + K_0}\right\} \qquad (16)$$

According to Eq. (16), the rising of the soil arch was related to the depth, soil properties, and design parameters, and $f(z)$ could be considered as the rise of arch when the soil arching effects were fully exerted.

In the current study, Eq. (17) (consisting of Eq. (5), Eq. (6), and Eq. (16)) was used to determine the distribution of the spatial soil arch surface. However, in order to acquire the spatial surface of the soil arch, it was first required to obtain some parameters, and the related parameters are listed in Table 1. Then, Matlab programming was employed to image the spatial soil arch surface.

$$\begin{cases} f(z) = \dfrac{l}{2K_0}\left\{\left[-\sqrt{\left(\dfrac{2\sigma_N b}{q(z)l}\right)^2 - 1}\right] + \sqrt{\left(\dfrac{2\sigma_N b}{q(z)l}\right)^2 - 1 + K_0}\right\} \\ \dfrac{x^2}{\left(B\sqrt{K_0}\right)^2} + \dfrac{(y-B)^2}{B^2} = 1 \\ B = \dfrac{f(z)}{2} + \dfrac{l^2}{8f(z)K_0} \end{cases} \qquad (17)$$

Table 1. Parameter values.

Parameter	Value
Cohesion, c	30 kPa
Internal friction angle, φ	25º
Unit weight, γ	18 kN/m
Net pile distance, l	4 m
The width of piles, b	1 m
Landslide thrust density, $q(z) = q$	$q(z)$ = 100 kPa

The spatial soil arching surface after the y coordinate transformed is shown in Figure 7. As can be seen in the figure, in any $f(z)$-l plane, its shape was part of an ellipse. Also, the shape varied with the depth. The spatial surface reflected the actual surface where the soil arching was fully exerted. The soil reached a yielding state in the spatial soil arching surface. It should be mentioned that the soil arching effects were observed to be the most intense on that surface. The soil arching also existed at other positions but the axis stress was not as significant as the yield stress.

From a physical point of view, the soil arching effects were essentially the 'extrusion-caulking effects' of the soil particles (Dong [14]). It has been found that when subjected to thrust, soil particles will move and rearrange themselves to the most compact positions. Therefore, the spatial soil arching surface reflects the position where the extrusion-caulking effects are the most intense. Furthermore, the soil outside the soil arch surface will remain in a good state of stability. However, the soil inside the arch surface may be subjected to local collapse due to the difficulty in forming extrusion-caulking effects.

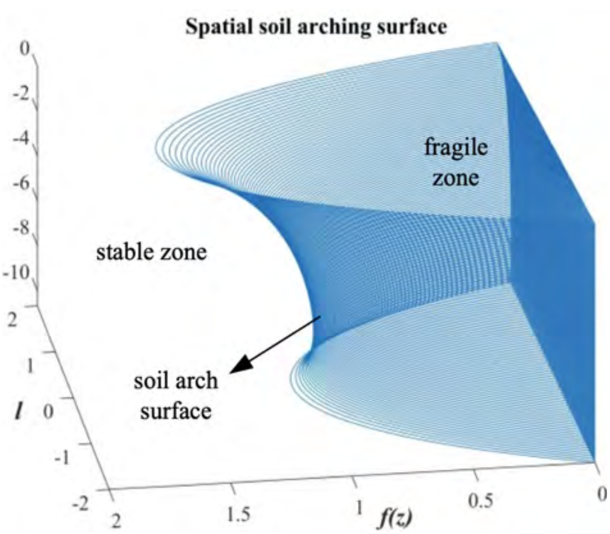

Figure 7. Spatial surface of the soil arch.

2.5 Determining the reasonable pile spacing

In the current study, the overall shear damage of the soil arch was considered in order to obtain the reasonable pile spacing. The limit equilibrium theory was used as a reference to determine that the angle of the slide surface of the soil arch and the major principal stress plane should be $45^o + \varphi/2$. Meanwhile, the stable compression zone behind the piles was assumed to be a keystone area, as detailed in Figure 8. It has been found that when the landslide thrust is significant, the soil arch can produce an overall shear damage phenomenon. Therefore, Eq. (18) was obtained based on the force balance on the slide surface:

$$\frac{2ct}{\sin(45^\circ-\varphi/2)}+[2\sigma_N t\sin(45^\circ-\varphi/2) \\ -q(z)l\sin\beta-K_0 q(z)t\frac{2ct}{\sin(45^\circ-\varphi/2)}\cos\beta]\tan\varphi \qquad (18) \\ =2\sigma\ \ t\cos(45^\circ\ \ \ \varphi/2)+q(z)l\cos\beta$$

Where

$$\beta=45^\circ-\theta+\varphi/2 \qquad (19)$$

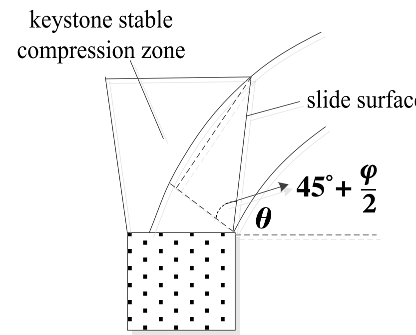

Figure 8. Compression zone at the arch foot.

For special engineer conditions in which the soil properties and pile sizes are known, the net pile distance l is related to depth z. In practice projects, if the pile spaces become too large, the soil between the piles may collapse. However, if the pile spacing is too small, materials may be wasted. The maximal pile space which can satisfy the stability requirements is considered to be the reasonable pile space. At any depth, Eq. (18) will need to be satisfied. Eq. (18) is the implicit function of l, which is difficult to directly obtain. Therefore, Matlab programming was also employed in this study to determine the numerical solution of l at any depth z. In a special depth z_1, z_2, ..., z_n, there must be a corresponding net pile space l_1, l_2, ..., l_n, solved from Eq. (18). Iterating could obtain the corresponding (i = 1, 2, 3, ..., n). Therefore, the minimum among l_1, l_2, ..., l_n, noted as l_{min}, will be the reasonable clear pile space. The reasonable pile space L is:

$$L=l_{\min}+b \qquad (20)$$

2.6 Calculating the earth pressure on the retaining plates

The simplified granary method simplifies the shape of soil arches into triangles and does not consider the friction of the soil structures. The unloading arch theory assumes that a soil arch is a parabolic arch, in which the arch foot is located at the retaining plates rather than the end-bearing soil arch of the piles (Li [2]). However, neither of the aforementioned two methods consider the applicability of cohesive soil. Therefore, a new method was introduced in this study to calculate the earth pressure acting on the retaining plates by considering the cohesion features based on a spatial soil arching model.

The hypothesis was that the horizontal thrust of the inner soil of the soil arching (σ_y) was evenly distributed

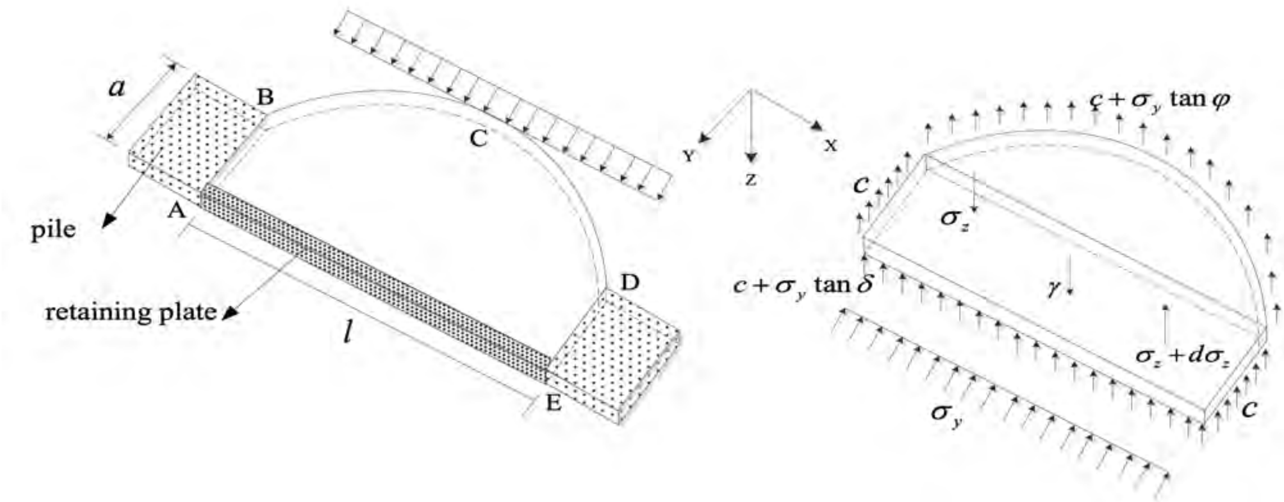

Figure 9. Stress illustration of the sheet pile walls.

on the walls and varied in the lateral pressure coefficient, $\lambda = \sigma_y / \sigma_z$. The friction stress produced by the soil-pile reaction stress σ_x and the thicknesses of the retaining plates could be ignored. A micro-segment *dz* with a distance *z* from the top was taken as the study object. The stress illustration is shown in Figure 9.

Then, from the vertical force balance, Eq. (21) could be obtained as follows:

$$\xi cPdz + l\sigma_y \tan\delta dz + P_1\sigma_y \tan\varphi dz + Ad\sigma_z = \gamma Adz \qquad (21)$$

Where *A* is the area of the enclosed Section ABCDE:

$$A = la + l\cdot f(z) - 2\int_0^{\frac{l}{2}} (B - \sqrt{B^2 - \frac{x^2}{K_0}})dx \qquad (22)$$

Also, P_1 is the perimeter of Section BCD:

$$P_1 = 2\int_0^{\frac{l}{2}} \sqrt{1 + \frac{x^2}{B^2 K_0{}^2 - K_0 x^2}}dx \qquad (23)$$

In the equation, *P* is the perimeter of the enclosed Section ABCDE:

$$P = 2a + l + P_1 \qquad (24)$$

In addition, σ_y represents the horizontal thrust, $\sigma_y = \lambda\sigma_z$; σ_z indicates the vertical thrust; δ denotes the friction angle between the wall back and soil; φ is the internal friction angle of soil; γ represents the soil weight; *c* is the cohesion; and ξ indicates the coefficient of cohesion reduction, and the cohesion cannot be fully exerted in the limited state. The value of ξ is determined by the engineering requirement; and *a* represents the length of the pile section.

Therefore, based on the above, Eq. (21) can be transferred into the following equation:

$$\frac{d\sigma_z}{dz} + C\sigma_z = \gamma - c\xi\frac{P}{A} \qquad (25)$$

Where

$$C = \frac{l\lambda\tan\delta + P_1\lambda\tan\varphi}{A} \qquad (26)$$

Subsequently, by solving Eq. (25) and substituting the boundary condition $\sigma_z = 0$ when $z = 0$, Eq. (27) was obtained as follows:

$$\sigma_z = \frac{\gamma - c\xi(P/A)}{C}(1 - e^{-Cz}) \qquad (27)$$

In addition, the horizontal thrust acting on the retaining plate was expressed as follows:

$$\sigma_y = \lambda\frac{\gamma - c\xi(P/A)}{C}(1 - e^{-Cz}) \qquad (28)$$

Then, the lateral pressure coefficient λ was determined using the aforementioned unloading arch method, which was expressed as:

$$\lambda = \frac{1 + \sin^2\varphi - 2\sqrt{\sin^2\varphi - \tan^2\delta\cos^2\varphi}}{4\tan^2\delta + \cos^2\varphi} \qquad (29)$$

Therefore, when the friction angle of wall back δ was zero, Eq. (29) could be simplified into Eq. (30) as follows:

$$\lambda = \frac{(1 - \sin\phi)^2}{\cos^2\phi} = \tan^2(45^\circ - \frac{\phi}{2}) \qquad (30)$$

Finally, Eq. (30) was determined to be the expression of the Rankine earth pressure coefficient.

In the current investigation, Eq. (28) was used to calculate the horizontal thrust acting on the retaining plates. However, σ_y was assumed to have a uniform distribution. In reality, the retaining plate was observed to mainly bear the lateral earth pressure generated by the collapsed inner soil and the soil arch. Therefore, the horizontal thrust along the pile-layout direction was not even. In addition, it was regarded as triangle distribution in which the maximal load was located at the middle point, while the loads on both sides were 0. The distribution mode of the horizontal thrust is detailed in Figure 10.

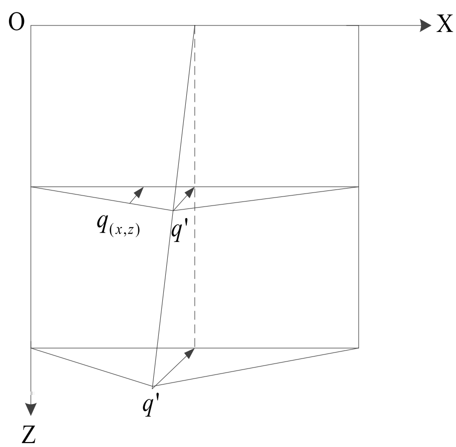

Figure 10. Distribution mode of the horizontal thrust.

Therefore, based on the above-mentioned findings, Eq. (31) was obtained:

$$\sigma_y l = \frac{q'}{2} l \qquad (31)$$

Where q' represents the horizontal thrust on the middle wall at depth z. The earth pressure at other points could then be solved using linear interpolation:

$$\begin{cases} q_{(x,z)} = \dfrac{4\sigma_y}{l} x, 0 \le x \le \dfrac{l}{2} \\ q_{(x,z)} = -\dfrac{4\sigma_y}{l}(x-l), \dfrac{l}{2} \le x \le l \end{cases} \qquad (32)$$

3 CASE STUDY

3.1 Project description

Maga landslide project located at Liupanshui Junction, Guizhou Province, China (Li [2]) was selected for evaluation in this study, as shown in Figure 11. It was determined that the upper layer of the slope was composed of residual clay (Q^{dl+el}), and the underlying bedrock was limestone of the Carboniferous Middle System Huanglong Group (C^{zhn}). Using a measurement process, the landslide thrust density acting on the excavation surface was confirmed to be $q(z)$ = 102.3 kPa and could be considered evenly distributed along the depths. After this study's comparison process was completed, a sheet pile wall was chosen as the retaining structure. The structure consisted of C30 concrete piles and retaining plates. The length of the cantilever part of piles was 10 m, and the typical section size of the piles measured 2 m × 2.5 m. According to the geotechnical testing results, the properties of the soil behind the sheet pile wall were as follows: the cohesion was c = 44.3 kPa; internal friction angle was $\varphi = 22^{o}$; and the soil unit weight was γ = 18.6 kN/m^3.

Figure 11. Landslide engineering project in Liupanshui Junction (Li [2]).

3.2 Determining the reasonable pile spacing

The method proposed in Section 2.5 was used to determine the reasonable pile spacing for the study object. For Eq. (18), the solution is in fact a numerical solution instead of an accurate analytical solution. However, in actual engineering projects, it is feasible to control the gap to less than 10^{-2} m. Therefore, Δz = 0.01 m and the reasonable net pile spacing can be deduced to be 5.84 m. The actual net pile spacing applied in this project was 6 m. The previous results calculated by other research studies are listed in Table 2 for purpose of comparison.

The parameters in Table 2 were all calculated when the soil arching had reached the ultimate state. Therefore, since the assumption conditions were different, the values of the net pile spacing varied significantly

Table 2. Comparison of the results obtained using different calculation models.

Calculation model by	Net pile space l (m)
Chen et al. [20]	3.56
Jiang et al. [21]	3.84
Wu et al. [22]	4.15
Qiu et al. [23]	9.25
Dong [14]	7.23
This research study	5.84

among the different studies. For example, considering spatial soil arching models and engineering experience, the pile spacing values in the references associated with Chen et al. [20], Jiang et al. [21], and Wu et al. [22] were relatively small. However, the results of Qiu et al. [23] was too large. The spatial soil arching model of Dong [14] adopted the Mohr-Coulomb criterion, but again the results were larger than the engineering design. It was observed that even after many years of operation, the sheet pile wall project had not suffered any damage. Therefore, the spatial soil arching model introduced in this research investigation was proven to conform better to realistic engineering applications.

3.3 Calculating the earth pressure on the retaining plates

The formulas detailed in Section 2.6 were used to calculate the uniform earth pressure on the retaining plates. However, due to the complexity of those formulas, Matlab programming was also employed. Then, the net pile distance was determined to be 5.84 m as previously stated and ξ was 0.3. The results calculated by other methods are also displayed in Figure 12 for comparison purposes.

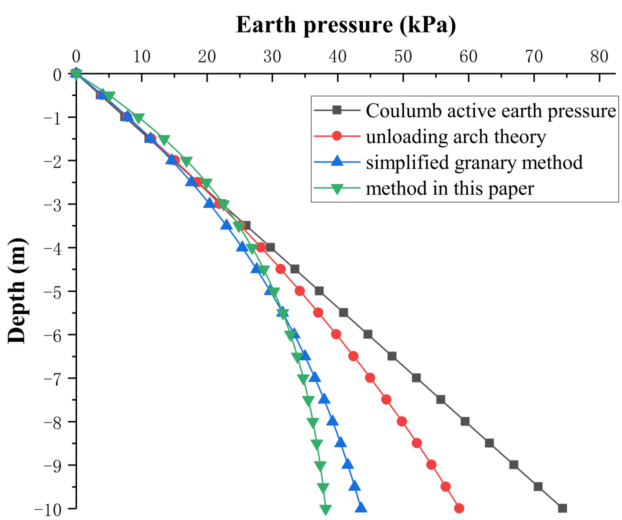

Figure 12. Comparison of earth pressure values obtained by the different methods.

The obtained results indicated that the four methods were similar when close to the tops of the piles. However, the gaps became larger with increasing depth. The earth pressure calculated by the Coulomb active earth pressure was the highest. This was due to the fact that the classical earth pressure did not consider the soil arching effects and the results were more conservative. The distribution law of the earth pressure by the method proposed in this study was similar to the simplified granary method and the unloading arch theory. However, due to the consideration of influencing effect of cohesion, the earth pressure value was less than that of the other two methods. The method proposed this study considered both the cohesion and realistic arch axis. Therefore, it was considered that this study's research conformed better to the actual conditions.

4 STABILITY ANALYSES OF THE SOIL BETWEEN THE PILES

4.1 Critical depths

As shown in Eq. (13), for special engineer conditions, the yield stress of outer soil-arch foot will only be related to the depth. This is due to the fact that the soil arching transfers the landslide into the axis stress of the arch. Therefore, the yield stress of B will only be impacted by gravity. In Eq. (13), $S(z)$ can be defined as a 'failure discriminant function'. When $S(z) \le 0$, the soil cannot reach a yielding state and will remain stable. However, if $S(z) > 0$, the soil in the outer arch-foot may produce yielding failure. Therefore, by ensuring $S(z) \le 0$, Eq. (33) was obtained:

$$z \le \frac{6\alpha k + 2k\sqrt{1-3\alpha^2}}{\gamma(1-12\alpha^2)} \qquad (33)$$

In Eq. (33), z is noted as z_0 when the equal sign is taken. The meaning of z_0 is the critical depth that the soil in the precipitous face can remain self-standing. Therefore, if the supporting heights of piles are lower than z_0, the soil between the piles may potentially remain stable. However, when the supporting heights of the piles without a retaining plate are higher than z_0, the soil between the piles could potentially partially collapse. Consequently, retaining plates between piles is considered to be necessary. Furthermore, this study's proposed formula had a certain application range for the condition of $z < z_0$.

As can be seen in Eq. (33), the critical depth was only related to the soil properties and the depth z. However, when the supporting depth exceeded the critical depth, it was observed that failure only occurred when the stress state of soil reached the yielding stress. Therefore, using the critical depth to judge whether a retaining plate is necessary is safer in practice. In order to analyze the parameter sensitivity of the critical depth, the variations of z_0 with the soil properties are detailed in Figures 13(a) to 13(c).

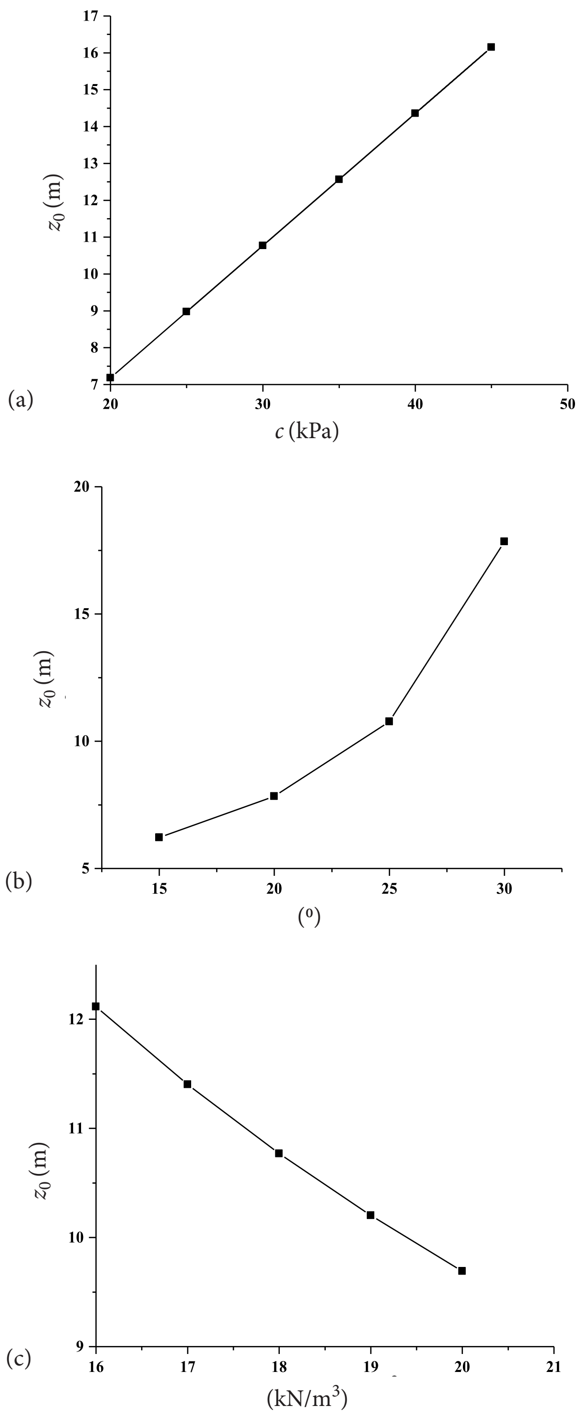

Figure 13. Influencing effects of the different parameters on the critical depth: (a) Influencing effects of the cohesion; (b) Influencing effects of the internal friction angles; (c) Influencing effects of the soil unit weights.

As shown in Figure 13, the critical depth majorly increased with increasing cohesion and internal friction angles. The values of c and φ were significant for the self-standing of the soil. It should be mentioned that the increment rate was faster for the φ, especially when the internal friction angles exceeded 25⁰. Therefore, increases in the internal friction angles could effectively improve the stability of the soil between the piles. However, it was found that z_0 decreased with the unit weight of the soil and it appeared that gravity dominated the yielding failure of the free-surface soil. This was determined to be due to the fact that the lateral pressure produced by gravity contributed a great deal to the failure of the soil. Generally speaking, the plane-strain soil arching models do not consider critical depth. The spatial soil arching model proposed in this study considered that the heights which the soil arching could exert were not infinite.

4.2 Rise of the soil arching

This study found that the rise of the soil arching $f(z)$ could potentially reflect the exertion extent of the soil arching. It was evident from Eq. (16) that the $f(z)$ was negatively related to the yielding stress σ_N. Therefore, a smaller arch rise would correspond to larger yielding stress. The larger yielding stress reflects superior soil properties. Moreover, a smaller rise also signifies less soil with weak extrusion-caulking effects along the inner soil arching surface. Therefore, a shorter arch rise indicates higher stability of the soil. In order to analyze the influencing effects of the various parameters on the arch rise, Figures 14(a) to 14(d) are graphed with some constant parameters derived from Table 1.

As can be seen in Figure 14, the rise of soil arching $f(z)$ first decreased and then increased slightly along the pile length. As shown in Figures 14(a) and 14(b), the $f(z)$ decreased with the increasing c as well as φ. Those results illustrated that the cohesion and internal friction angles contributed to the soil stability. The better the engineering properties of the soil, the greater of the stability of pile-soil structure.

As presented in Figure 14(c), the arch rise $f(z)$ increased with the increasing pile diameter ratio, l/b. It should be noted that when the net pile distance was 5 times that of the pile width, the value of $f(z)$ disappeared at the upper pile, which confirmed that the soil arching effects had vanished. The analysis results indicated that the soil arching effects realized their potential when l/b was less than 5. This conclusion agreed with many previous research study findings and engineering experiences (Adachi et al. [9]; Li [2]). Therefore, it was evident that larger pile spacing could adversely affect the stability of the soil. If the pile spacing was too large, the soil between the piles was prone to collapse failure. Therefore, proper design of the pile spacing should be considered as crucially important for the safety of such engineering projects.

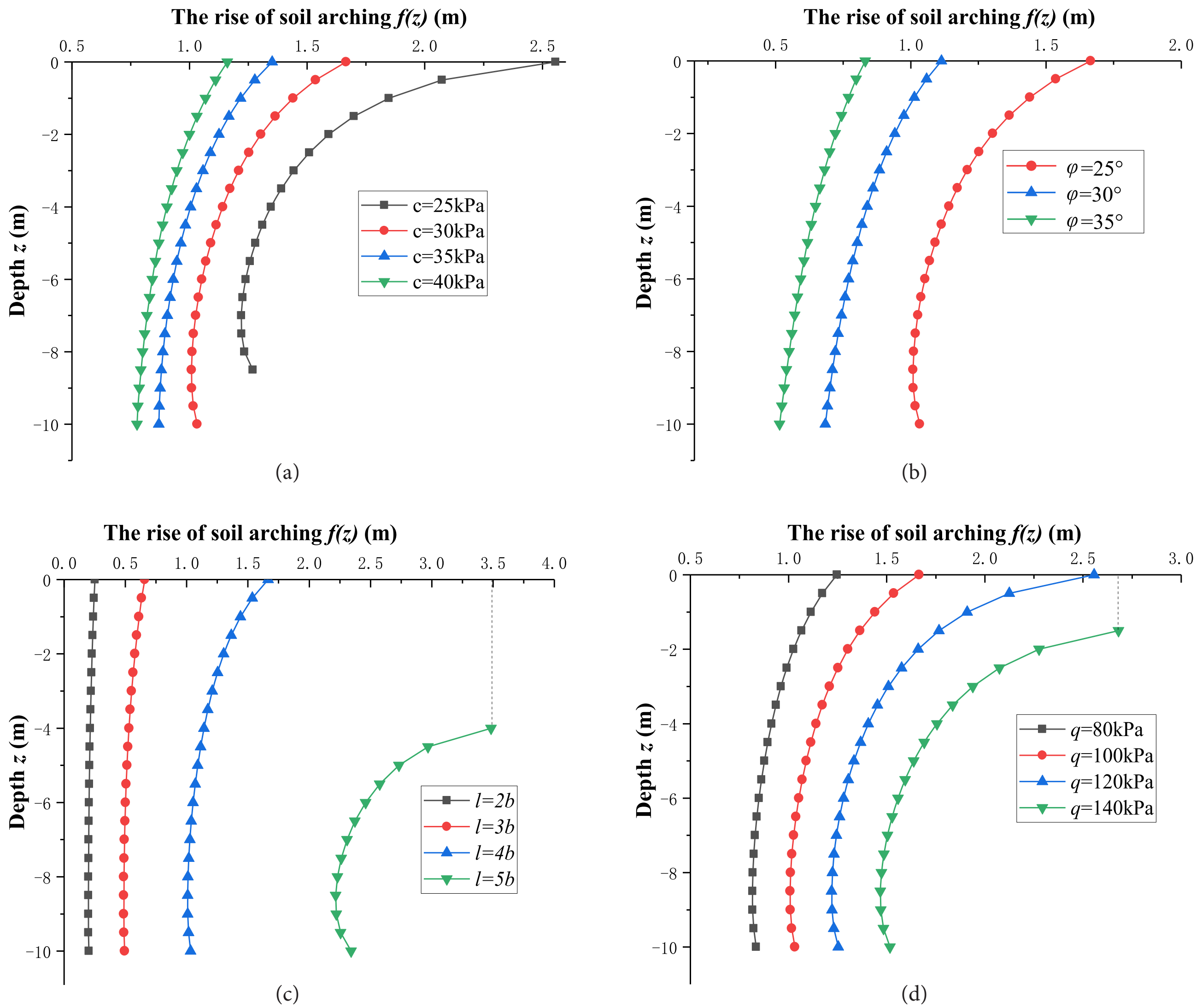

Figure 14. Influencing effects of the parameters on the rise of soil arching: (a) Influencing effects of of c on $f(z)$; (b) Influencing effects of φ on $f(z)$; (c) Influencing effects of l on $f(z)$; (d) Influencing effects of q on $f(z)$.

The influencing effects of landslide thrust q on the rise of the soil arching are presented in Figure 14(d). It was assumed that the landslide thrust was constant along the depths. It can be seen in the figure that the $f(z)$ was reduced as the q decreased, which indicated that greater landslide thrust damaged the stability of the soil between the piles. This conclusion also conformed to previous engineering practices. In addition, as detailed in Figure 14(d), when q = 140 kPa, the value of $f(z)$ also disappeared at the upper piles. Therefore, it was concluded that if the landslide thrust was too great, the soil arching effects may fade away. It should be noted that proper design can improve the abilities of soil-pile structures to withstand major landslide thrust.

The maximal landslide thrust density can be determined by the existence of soil arching. The sufficient exertion of the soil arching effects can be solved using Eq. (16). Therefore, the following formula should be satisfied:

$$\left(\frac{2\sigma_N b}{q(z)l}\right)^2 - 1 \geq 0 \qquad (34)$$

Then, Eq. (35) equation can be obtained:

$$\begin{cases} q(z) \leq \dfrac{b}{l - b\tan^2(45^\circ + \varphi/2)}\left[2c\tan(45^\circ + \varphi/2) + \dfrac{\gamma z(1+6\alpha^2) + 6\alpha k + 3\sqrt{S(z)}}{2(1-3\alpha^2)}\right] \\ S(z) = z^2(12\alpha^2\gamma^2 - \gamma^2) + 12\alpha k\gamma z + 4k^2 \\ \alpha = \dfrac{2\sin\varphi}{\sqrt{3}(3-\sin\varphi)}, k = \dfrac{6c\cos\varphi}{\sqrt{3}(3-\sin\varphi)} \end{cases} \qquad (35)$$

Eq. (35) can be used to estimate the maximal landslide thrust density at any depth. Eq. (35) can also be applied to judge whether a design condition is safe. If the actual landslide thrust is less than that calculated by Eq. (35), the design parameters are appropriate. Otherwise, the design parameters of the piles should be improved.

4.3 Failure control conditions

There are usually two destruction modes: partial plastic deformation and general shear failure. Partial plastic deformation usually appears as local collapses and those types of destruction often present relatively slight damage. Its corresponding controlling formulas are Eqs. (33) and (35). Eq. (33) can be used to solve the maximal height at which the free surface between piles will not fall. Eq. (35) determines the maximal landslide thrust density which a design condition of piles can undertake when yielding failure does not occur. Eqs. (33) and (35) together control the partial plastic deformation failure.

In regard to general shear failure, such a failure mode is usually accompanied with a large scale and heavy damages. Eq. (18) was established based on the limit state at which the soil arching is put out from the piles by the landslide. Therefore, Eq. (18) can be regarded as the controlling equation of general shear failure. In addition, the pile spacing described in Section 2.5 must be satisfied. If considering the safety factors, the reasonable pile space calculated can also be reduced.

In summary, in order to guarantee the soil between the piles will experience no damage, Eqs. (33), (35), and (18) must be satisfied simultaneously.

5 CONCLUSIONS

In accordance with the limit equilibrium theory, this study introduced a spatial soil arching model. Then, based on the spatial soil arching model, the reasonable pile spacing and the earth pressure on the retaining plates were determined. The method was coded in Matlab with a Graphical User Interface (GUI) for the purpose of realizing the automatic operations of the complex formulas utilized in this investigation. Therefore, considering the spatial soil arching model, the stability of soil between the piles was also analyzed. The major conclusions of this research were summarized as follows:

(1) Considering the horizontal stress produced by the soil behind the piles, the shape of the soil arching axis was shown to be a partial ellipse. In addition, by regarding the soil yielding stress as the axis stress of the soil arching, the rise of the soil arching was examined in detail. Subsequently, an effective spatial soil arching model was obtained.

(2) When the soil arching effects generated general shear failure, the stress balance in the limit state of the soil arching was the control condition. A theory which could be used to calculate the reasonable pile spacing was deduced. The results from this investigation's case study showed that the proposed method displayed better rationality when compared with previous related research studies.

(3) It was found that by considering the spatial soil arching model and the influencing effects of cohesion, the proposed method's estimates of the earth pressure values were improved. The calculation results showed a good conformity with practical engineering projects.

(4) On the basis of the spatial soil arching, analyses of the stability of the soil between piles were completed. Then, corresponding controlling equations were established for the possible failure modes.

The proposed spatial soil arching model considered the spatial distributions of the soil arching and was found to conform better to the actual situations. Programmed numerical computations based on Matlab were developed in order to extend the calculation method to future engineering applications.

It should be mentioned that this research ignored the influencing effects of the friction soil arching between the piles. In addition, it was also found to not be practical to assume the thicknesses of the soil arching as the widths of the piles. In the future, it was recommended that further experiments be conducted for the purpose of exploring the real thicknesses of the soil arching. Furthermore, this research did not consider the foundation reactions on the piles, which should also be further investigated in future studies.

Declarations

Funding: This research was supported in part by the Key Research and Development Program of Shandong Province (No. 2019GSF109045); Qilu Young Scholar Program of Shandong University (201999000171); and the Natural Science Foundation of Jiangsu Province (BK2020040885).

REFERENCES

[1] Guharay A, Baidya DK. 2015. Reliability-Based Analysis of Cantilever Sheet Pile Walls Backfilled with Different Soil Types Using the Finite-Element Approach. International Journal of Geomechanics,

15(6).06015001. doi: 10.1061/(ASCE)GM.1943-5622.0000475
[2] Li Haiguang. 2016. Design of new supporting structure and engineering examples. People's Communications Publishing House, Beijing, China.
[3] Zhang H, Chen J, Ma H, et al. 2019. A New Method to Determine a Reasonable Pile Spacing of Stabilizing Piles and Earth Pressure on Sheet Piles. Journal of Engineering Science & Technology Review, 12(1):37-44. doi: 10.25103/jestr.121.05
[4] Terzaghi K. 1936. Stress distribution in dry and in saturated sand above a yielding trap-door. In: Proc. 1st Int. Conf. Soil Mech., Harvard University, Cambridge, Mass., 1:307-311.
[5] Handy RL. 1985. The arch in soil arching. Journal of Geotechnical Engineering, 111(3): 302-318. doi: 10.1061/(ASCE)0733-9410(1985)111:3(302)
[6] Dalvi RS, Pise PJ. 2012. Analysis of Arching in Soil-Passive State. Indian Geotechnical Journal, 42(2):106-112. doi: 10.1007/s40098-012-0004-8.
[7] Bosscher PJ, Gray DH. 1986. Soil arching in sandy slopes. Journal of Geotechnical Engineering, 112(6):626-645. doi: 10.1061/(ASCE)0733-9410(1986)112:6(626)
[8] Wang WL, Yen BC. 1974. Soil arching in slopes. Journal of Geotechnical Engineering, 100:61-78. doi: 10.1016/0148-9062(74)90721-9
[9] Adachi T, Kimura M, Tada S. 1989. Analysis on the preventive mechanism of landslide stabilizing piles. International symposium on numerical models in geomechanics. (NUMOG III). 1989;691-698.
[10] Zhao L, Zhou W, Geng X, et al. 2019. A closed-form solution for columnsupported embankments with geosynthetic reinforcement. Geotextiles and Geomembranes, 47(3):389-401. doi: 10.1016/j.geotexmem.2019.01.006
[11] Pardo G S, Sáez E. 2014. Experimental and numerical study of arching soil effect in coarse sand. Computers and Geotechnics, 57:75-84. doi: 10.1016/j.compgeo.2014.01.005
[12] Ausilio E, Conte E, Dente G. 2001. Stability analysis of slopes reinforced with piles. Computers and Geotechnics, 28(8):591-611. doi: 10.1016/S0266-352X(01)00013-1
[13] Li C, Tang H, Hu X, et al. 2013. Numerical modelling study of the load sharing law of anti-sliding piles based on the soil arching effect for Erliban landslide, China. KSCE Journal of Civil Engineering, 17(6):1251-1262. doi: 10.1007/s12205-013-0074-x
[14] Dong Jie. 2009. Study on Three-dimensional Soil Arching Effect of Cantilever Piles and Ground Resisting Force Acted on Its Build-in Zone. PhD Thesis, Chongqing University, Chongqing, China.
[15] Chen CY, Martin GR. 2002. Soil-structure interaction for landslide stabilizing piles. Computers and Geotechnics, 29(5):363-366. doi: 10.1016/S0266-352X(01)00035-0
[16] Liang RY, Yamin M. 2010. Three-dimensional finite element study of arching behavior in slope drilled shafts system. International Journal for Numerical and Analytical Methods in Geomechanics, 34(11):1157-1168. doi: 10.1002/nag.851
[17] Şahin, A. 2011. Mathematical models and solution algorithms for computational design of RC piles under structural effects. Applied Mathematical Modeling, 35(7):3611-3638. doi: 10.1016/j.apm.2011.01.037
[18] Yamin M. 2007. Landslide stabilization using a single row of rock-socketed drilled shafts and analysis of laterally loaded drilled shafts using shaft deflection data. PhD Thesis, The University of Akron, Akron, USA.
[19] He GF, Li ZG, Yuan Y, et al. 2018. Optimization analysis of the factors affecting the soil arching effect between landslide stabilizing piles. Natural Resource Modeling, 31(2): e12148. doi: 10.1111/nrm.12148
[20] Chen G, Zou L, Wang Q, et al. 2020. Pile-Spacing Calculation of Anti-Slide Pile Based on Soil Arching Effect. Advances in Civil Engineering, 2020(6269):1-6. doi: 10.1155/2020/7149379
[21] Jiang L, Huang R, Jiang Z. 2006. Analysis of Soil Arching Effects between Adjacent Piles and Their Spacing in Cohesive Soils. Rock and Soil Mechanics, 27(3): 445-450. doi: 10.16285/j.rsm.2006.03.022.html
[22] Wu J, Li C, Liu Q, et al. 2017. Optimal isosceles trapezoid cross section of laterally loaded piles based on friction soil arching. KSCE Journal of Civil Engineering, 21(7):2655-2664. doi: 10.1007/s12205-017-1311-5
[23] Qiu ZY, Han TC, Dou HQ. 2016. Analysis of spacing between anti-slide piles considering soil arch on lateral sides and back. Journal of Zhejiang University (Engineering Science), 50(3):559-565. doi: 10.3785/j.issn.1008-973X.2016.03.021
[24] Li SJ, Chen J, Feng XT. 2011. Analytic solution to soil arching effect and its application based on interaction of slope soil and piles. Materials Research Innovations, 15(sup1): s578-581. doi: 10.1179/143307511X12858957676876
[25] Zhang H, Li C, Yao W, et al. 2019. A Novel Approach for Determining Pile Spacing considering Interactions among Multilayered Sliding Masses in Colluvial Landslides. KSCE Journal of

Civil Engineering, 23(9):3935-3950. doi: 10.1007/s12205-019-0459-6

[26] Eskisar T, Otani J, Hironaka J. 2012. Visualization of soil arching on reinforced embankment with rigid pile foundation using X-ray CT. Geotextiles and Geomembranes, 32: 44-454. doi: 10.1016/j.geotexmem.2011.12.002

[27] Risio MD, Bellotti G, Panizzo A, et al. 2009. Three-dimensional experiments on landslide generated waves at a sloping coast. Coastal Engineering, 56(5-6):659-671. doi: 10.1016/j.coastaleng.2009.01.009

[28] Vermeer PA, Punlor A, Ruse N. 2001. Arching effects behind a soldier pile wall. Computers and Geotechnics, 28(6-7):379-396. doi: 10.1016/S0266-352X(01)00010-6

[29] Zhang YX, Dong J, Wen HY, et al. 2009. Research on three-dimensional soil arching effect and appropriate spacing of cantilever anti-slide piles with consideration of geostatic stress. China Journal of Highway and Transport, 22(2):18-25. doi: 10.19721/j.cnki.1001-7372.2009.02.004

[30] Li C, Wu J, Tang H, et al. 2015. A novel optimal plane arrangement of stabilizing piles based on soil arching effect and stability limit for 3D colluvial landslides. Engineering Geology, 195:236-47. doi: 10.1016/j.enggeo.2015.06.018https://s100.copyright.com/AppDispatchServlet?publisherName=ELS&contentID=S0266114411001373&orderBeanReset=true

[31] Huang ZY, Zhang YX, Dong J. 2013. Experimental study of soil arching and transfer behavior of earth pressure about sheet-pile walls. Rock and Soil Mechanics, 34(007):1887-1892. doi: 10.16285/j.rsm.2013.07.040.html

[32] Yang M, Yao LK, Wang GJ. 2007. Study on effect of width and space of anti-slide piles on soil arching between piles. Chinese Journal of Geotechnical Engineering, 29(10):1477-1482. doi: 10.3321/j.issn:1000-4548.2007.10.008

LANDSLIDE STABILITY BASED ON A LIMIT-EQUILIBRIUM ANALYSIS: A CASE STUDY

ANALIZA STABILNOSTI PLAZU, KI TEMELJI NA ANALIZI MEJNEGA RAVNOTEŽJA, ŠTUDIJA PRIMERA

Pınar Sezin Öztürk Kardoğan
Gazi University,
Faculty of Technology,
Department of Civil Engineering
Ankara, Turkey
E-mail: sezinozturk@gazi.edu.tr

Ahmet Erdağ *(corresponding author)*
Gazi University,
Faculty of Technology,
Department of Civil Engineering
Ankara, Turkey
E-mail: ahmeterdag@gazi.edu.tr

Hasan Emre Demirci
İzmir Katip Çelebi University,
Faculty of Engineering and Architecture,
Department of Civil Engineering
İzmir, Turkey
E-mail: hasanemre.demirci@ikcu.edu.tr

DOI https://doi.org/10.18690/actageotechslov.19.1.17-29.2022

Keywords

landslides, slope stability, Limit-equilibrium method, Kars Dam

Abstract

Landslides are natural hazards that are commonly observed in nature. They generally cause loss of life and property, because they can severely damage engineering structures such as dams, highways, railways, pipelines, and buildings. The potential zones of landslides need to be specified and their failure mechanisms need to be understood to mitigate the effects of landslides on societies, economies, and industries. Therefore, potential landslide zones need attention, specifically for engineering structures with large investment values. The identification of zones with a high potential risk of the occurrence of landslides is essential to avoid possible losses due to landslides. An analysis of the landslide susceptibility of potential areas results in the safer application and performance of engineering projects, and it helps engineers to take important measures regarding potential landslide damage. In this paper, a landslide failure that occurred during the construction of the transmission line of the Kars Dam is presented and possible measurements to avoid landslide damage on the transmission line are investigated. Slope-stability analyses were performed using the limit-equilibrium method, and as a result of the analysis, two different engineering solutions are proposed to avoid landslide movements. A cost analysis for the proposed solutions is also made to specify the optimum solution by considering both safety and costs.

Ključne besede

plazovi, stabilnost pobočja, metoda mejnega ravnovesja, jez Kars

Izvleček

Plazovi so naravne nesreče, ki jih v naravi pogosto opazimo. Ker močno poškodujejo inženirske konstrukcije, kot so jezovi, avtoceste, železnice, cevovodi in zgradbe, na splošno povzročajo škodo na premoženju ali celo izgubo življenj. Da bi ublažili učinke plazov na družbo, gospodarstvo in industrijo je potrebno določiti možna območja zemeljskih plazov in razumeti njihove porušne mehanizme. Zato je treba še posebno pozornost nameniti potencialnim plazovitim območjem ob inženirskih objektih z velikimi naložbenimi vrednostmi. Identifikacija območij z visokim potencialnim tveganjem za nastanek zemeljskih plazov je bistvenega pomena, da se izognemo morebitnim škodam zaradi zemeljskih plazov. Analiza občutljivosti potencialnih območij na zemeljske plazove omogoča varnejšo uporabo in izvedbo inženirskih projektov ter pomaga inženirjem, da sprejmejo bistvene ukrepe za zmanjšanje morebitne škode zaradi plazu. V prispevku je predstavljena porušitev zaradi plazu, ki je nastala pri gradnji dovodnega kanala jezu Kars, in raziskane možne meritve za preprečevanje poškodb zemeljskega plazu na dovodnem kanalu. Analize stabilnosti pobočij so se izvedle z uporabo metode mejnega ravnovesja in kot rezultat analize sta predlagani dve različni inženirski rešitvi za preprečevanje premikov plazu. Izdelana je tudi stroškovna analiza za predlagani rešitvi, s čimer je bil določena optimalna rešitev ob upoštevanju varnosti in ekonomičnosti.

1 INTRODUCTION

Turkey is a developing country where many engineering projects are in progress due to its growing population and increasing public demands. The increase in population results in a rise in consumer demands for goods and energy. In Turkey, many projects related to the energy sector have been completed in recent years, while many of them are still under construction. The geology of the construction site is one of the most significant aspects to be considered during design and construction. Essential geological works need to be carried out before the construction and engineering structures are designed by considering important geological aspects. Otherwise, unexpected geological problems can occur during the construction. These geological problems influence the completion of the engineering works, and they also increase the project's costs. Landslides are one of the geological problems that are widely observed in the field. Landslides can occur at settlements that are located on slopes, at areas where the construction of highways and railways is in progress, and can also occur during the excavation of the toe of the slopes. In addition, earthquakes, excessive precipitation, and volcanic activities can trigger landslides. Table 1 summarises several landslide failures observed in the literature and their effects on society. As seen in the table, landslides cause a loss of property and life, killing thousands of people and destroying homes and infrastructures. Therefore, slope stabilization plays a key role in avoiding landslide movements. The main aim of slope stabilization is to obtain more stable and more economic slopes with minimum chances of failure.

In this study, a landslide failure that occurred during the construction of the transmission line of the Kars Dam is presented and two different engineering solutions to avoid landslide movements along the transmission line of the Kars Dam are proposed using a slope-stability analysis. Rocscience Slide 6.0 and Geo5 software were used to model the proposed engineering solutions. These two programs analyse the slope stability by using the Limit-Equilibrium Method. Safety factors are obtained for the proposed engineering solutions and their costs are compared. Finally, a convenient solution is proposed for this landslide problem based on the slope-stability and cost analyses.

2 FACTORS AFFECTING SLOPE STABILITY AND LANDSLIDES

There are several factors that cause landslides: (a) geological environment of the area, including geological structure, lithology, hydrogeological conditions and topography [9, 10, 11, 12, 13, 14] and (b) earthquakes [15, 16] human engineering activities [17, 18] and rainfall [1, 19, 20, 21, 22, 23] also significantly influence the development of landslides.

In addition, many studies have been carried out to evaluate the landslide hazard and produce susceptibility maps around the world by applying different methods [24]. Most of these studies used probabilistic models [25,26]. However, one of the other methods is the Geographic Information System (GIS), which is frequently applied and constantly improved [27].

The landslide failure investigated in this study is a landslide induced by human engineering activities. The failure occurred due to the excavation of the toe of the slope to construct a transmission line. In the following sections, the area of investigation is presented and the slope-stability analysis of the slope after the excavation of the transmission line is performed. Two different engineering solutions are proposed to avoid the potential landslide failure. A cost analysis of these two solutions is also made to specify an optimum solution by considering costs and safety.

Table 1. Several landslide failures observed in the literature and their effects on society and services.

Location	Year	Loss of Properties	Scale	References
Italy	1730	51 Fatalities	Major	[1]
Peruvian Andes	1970	Destroyed a city and killed more than 25,000 people	Major	[2]
Malesia	2000	Road damage	Medium	[3]
La Conchita in California	2005	Destroyed 13 houses, severely damaged 23 others, and killed 10 people	Medium	[4]
Leyte Island in the Philippines	2006	Buried more than 1100 people	Major	[5]
Malesia	2008	Damage of 14 units of bungalows	Major	[3]
Baguio-Philippines	2009	200 Fatalities	Major	[6]
India	2011	Road damage	Medium	[7]
Nepal	2015	Damage on 4 major highways	Medium	[8]

Figure 1. Google map showing the landslide movement that occurred next to the transmission line of the Kars Dam.

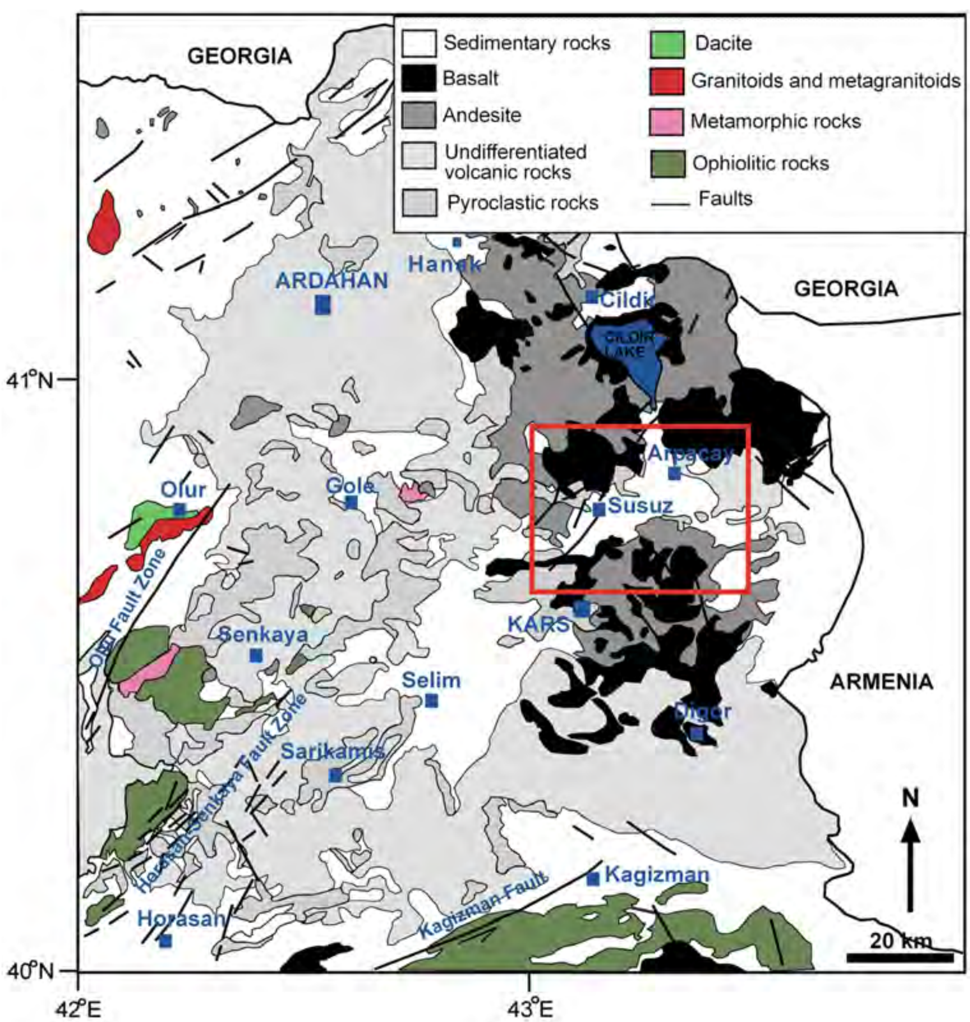

Figure 2. Geological maps of the study area.

3 MATERIAL AND METHOD

3.1 Study Area and Geological Properties

The area of the investigation is in the northeast of Kars, 18 km from the centre of Kars. The area is shown on the map in Figure 1 [28].

The Kars region, where a large part of the surface is covered by a volcano, looks like a plateau. The oldest rocks seen in the region are Paleozoic aged schists and marbles. The sequence starts with the Upper Cretaceous basal conglomerate and continues with limestone. Later Eocene sandstones and conglomerates are observed, intercalated with basic volcanic. Depth and surface eruptions are dominant in almost every geological period after the Palaeozoic. The most active period of volcanism is the Upper Pliocene and even Quaternary. Due to compressional movements in the general arc of the Lesser Caucasus, small faults that are vertical to the main structure have developed in the region. The geological map of the region is shown in Figure 2 [29].

The rocks outcropping throughout the region, including the project area, are evaluated according to the lithological, structural, stratigraphic and age order of the units. The formation names made in the studies carried out in the region can be followed easily from the literature, and the formation names and symbols specified in previous studies are used exactly. The locations of the rocks that affect the geological structure in the project area are in place since the Upper Miocene. The general geotechnical properties of the units according to their stratigraphic sequence are described below.

3.2 Brief description of the limit equilibrium

The Limit-Equilibrium Method (LEM) with the perfectly Mohr-Coulomb criterion has been widely used by geotechnical engineers for many years to analyse the stability of slopes [30]. Many researchers have used this method to study the stability of slopes and factors affecting stability [31, 32, 33, 34, 35, 36, 37] The method uses the theory of plasticity with the assumption that failure occurs at a critical plane in a slope, and it uses equilibrium equations for a sliding mass to solve the slope-stability problem. The LEM can be used for slope-stability problems with complicated loading conditions, homogeneous or heterogeneous soil profiles. Several methods are commonly used to analyse the stability of slopes: Fellenius (1936) [38], Bishop (1955) [39], Janbu (1973) [40], Spencer (1967) [41], and Morgenstern and Price (1965) [42].

4 ANALYSES

Figure 3 shows an idealized side view of the slope before the construction of the transmission line. The height of the slope is 13 m, and the inclination angle of the slope is 20º, as illustrated in the figure. An idealized side view of the slope after the excavation of the transmission line is illustrated in Figure 4. The dimensions of the transmission line are 5 m in width and 5 m in height, as seen in the figure. After the excavation of the transmission line, a landslide failure occurred in the slope next to the excavation of the transmission line. Figure 5 shows a photograph of the landslide failure developed in the slope.

The slope after the excavation of the transmission line is modelled by using Slide 6.0 software [43]. The soil parameters in the case where stability analyses were performed are given in Table 1.

Table 2. Geotechnical properties of the soil in the area of investigation.

Soil Properties	Values
Specific Gravity (G_s)	2.65
Atterberg Limits	
Liquid Limit (*LL*)	40 %
Plastic Limit (*PL*)	22 %
Plasticity Index (*PI*)	18 %
Engineering Properties	
Cohesion (c)	5 kPa
Angle of Internal Friction (Φ)	15°
Specific Bulk Density (γ)	17.9 kN/m^3
Poisson's Ratio (ν)	0.27

The geometry of the slope and the values of the factor of safety (FoS) for different methods are shown in Figure 6. These different methods are Bishop's method, Janbu's method, Fellenius' method, Spencer's method, and the GLE/Morgenstern-Price method. The values of the FoS for each method are summarised in Table 2. The values of the FoS range from 1.185 to 1.295, as seen in the table. The slope is considered as critically stable when the values of the FoS are very close to a value of 1.0 and less than a value of 1.5. Therefore, two different engineering solutions are proposed to avoid possible landslide risk in the slope: (1) stepped excavation to decrease the inclination angle of the slope and (2) construction of a retaining wall in front of the slope.

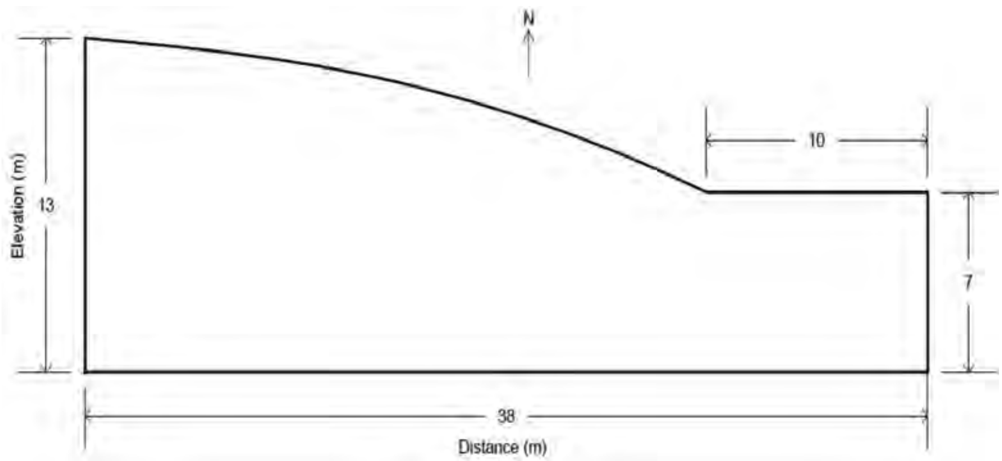

Figure 3. Idealized side view of the slope before the construction of the transmission line.

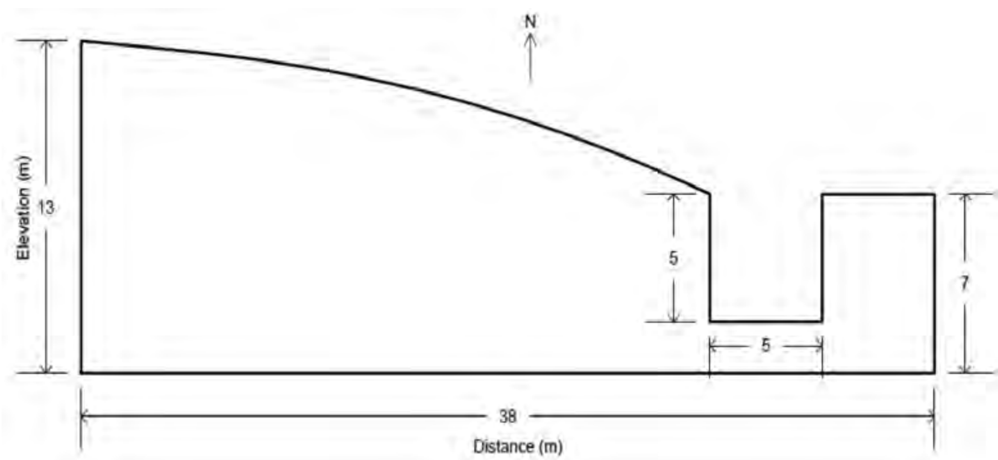

Figure 4. Idealized side view of the slope after the excavation of the transmission line.

Figure 5. Landslide failure occurred due to the excavation of the transmission line.

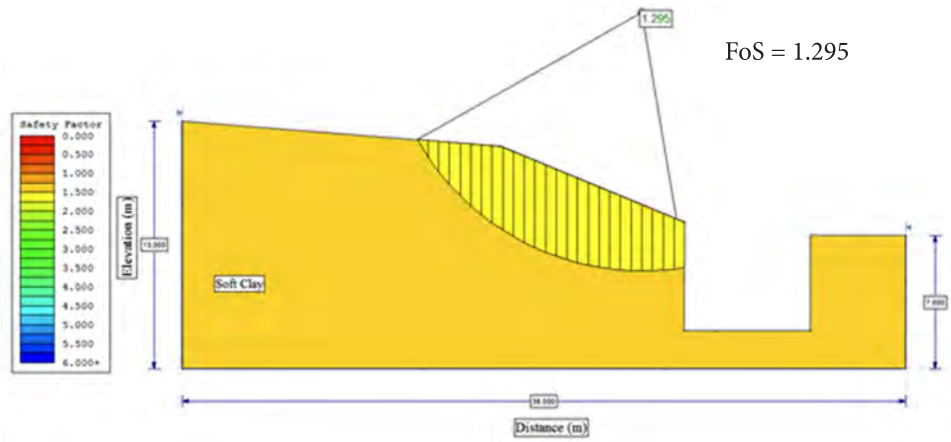
1.295
FoS = 1.295
Safety Factor
0.000
0.500
1.000
1.500
2.000
2.500
3.000
3.500
4.000
4.500
5.000
5.500
6.000+
Elevation (m)
Soft Clay
Distance (m)

a)

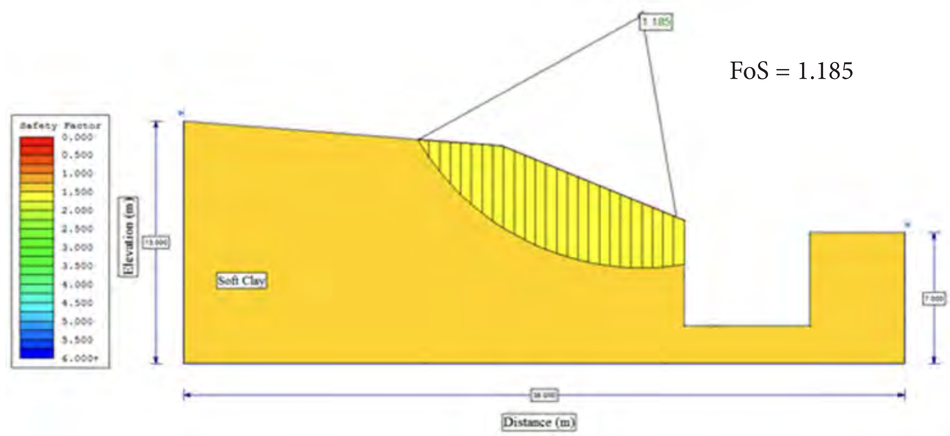
1.185
FoS = 1.185
Safety Factor
0.000
0.500
1.000
1.500
2.000
2.500
3.000
3.500
4.000
4.500
5.000
5.500
6.000+
Elevation (m)
Soft Clay
Distance (m)

b)

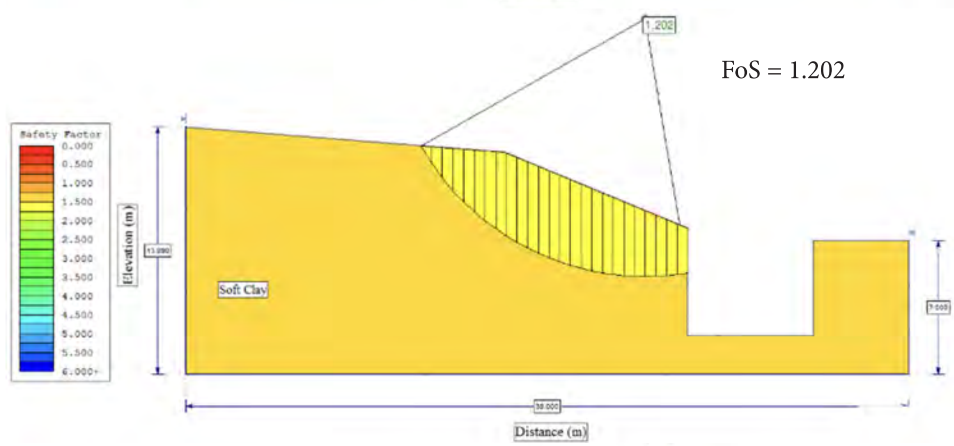
1.202
FoS = 1.202
Safety Factor
0.000
0.500
1.000
1.500
2.000
2.500
3.000
3.500
4.000
4.500
5.000
5.500
6.000+
Elevation (m)
Soft Clay
Distance (m)

c)

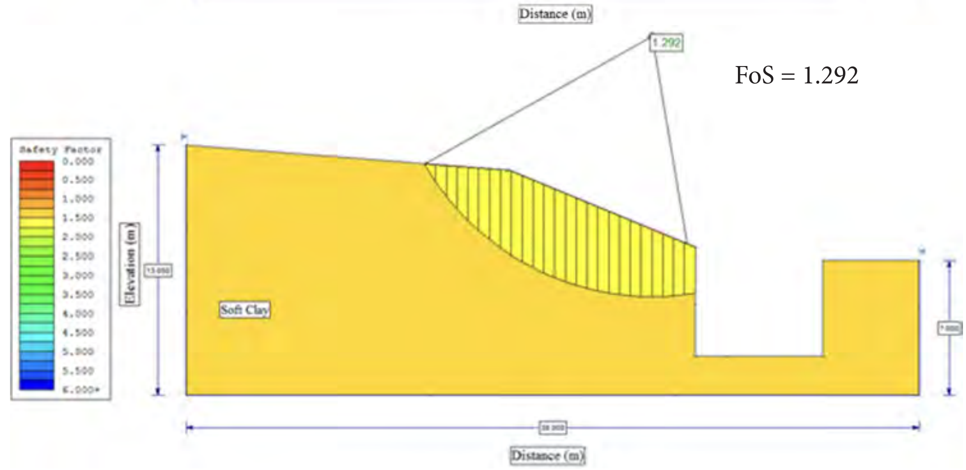
1.292
FoS = 1.292
Safety Factor
0.000
0.500
1.000
1.500
2.000
2.500
3.000
3.500
4.000
4.500
5.000
5.500
6.000+
Elevation (m)
Soft Clay
Distance (m)

d)

e)

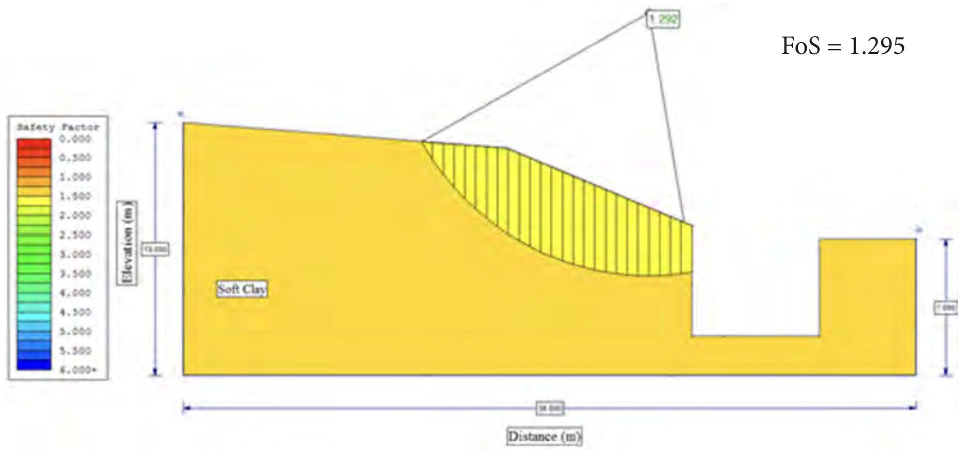

Figure 6. Analyzed slope: (a) Bishop's method, circular slip surface (b) Janbu Simplified method, circular slip surface (c) Fellenius, circular slip surface (d) Spencer method (e) GLE/Morgenstern-Price, circular slip surface.

Table 3. FoS obtained using different methods for the slope before the landslide.

Method	Computed FoS	Remarks
Bishop	1.295	Critically Stable
Janbu-simplified	1.185	
Fellenius	1.202	
Spencer	1.292	
GLE/Morgenstern-Price	1.292	

4.1 Engineering Solution 1

The side view of the slope after the stepped excavation is shown in Figure 6. All the dimensions of the new slope after the excavation can be seen in Figure 6. This problem is modelled using SLIDE 6.0 software. The model geometry used in the SLIDE 6.0 software for different methods and the values of the FoS for each method are shown in Figure 7. Table 3 summarises the values of the FoS calculated for different methods. The values of the FoS vary between 1.675 and 1.790, as seen in the table. As the values of the FoS are greater than 1.5, the new slope is considered stable.

4.2 Engineering Solution 2

The second engineering solution to stabilize the slope is to construct a retaining wall at the toe of the slope, next to the transmission line. The problem is modelled using Geo5 software and the model geometry used in the software is demonstrated in Figure 8 [44]. The cross-section of the retaining wall is shown in Figure 9 and its dimensions are also shown in the figure. Table 4 summarises the engineering properties of the material of the retaining wall. The values of the FoS are calculated by applying Geo5 software and these values for each method are summarised in Table 5. The values of the FoS range between 1.540 and 1.580, as seen in the table. After the construction of the retaining wall, the slope is considered stable (FoS > 1.540).

a)

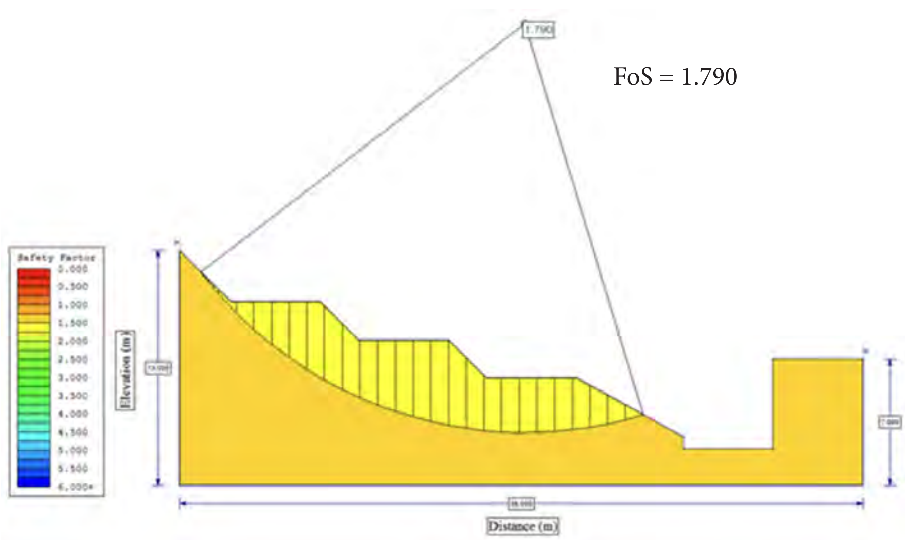

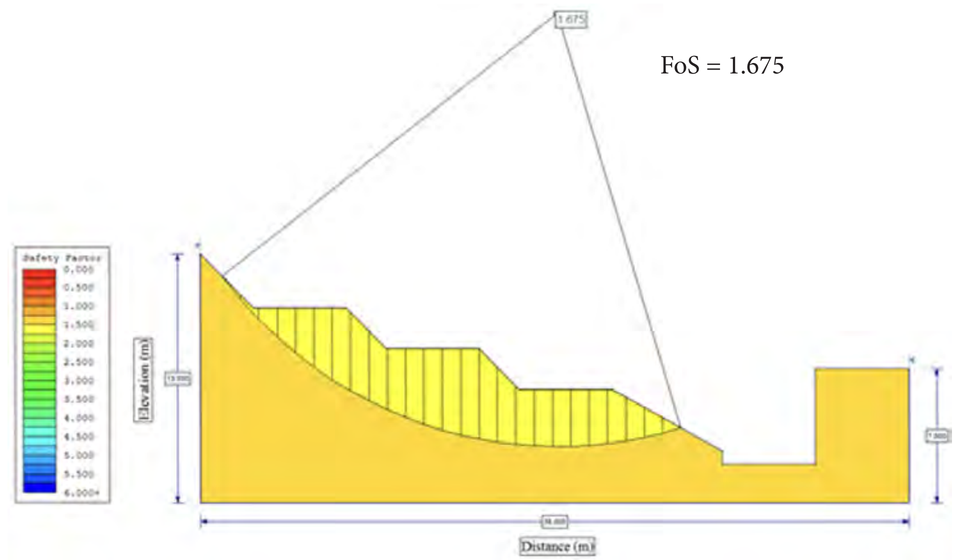
FoS = 1.675
1.675
Safety Factor
Elevation (m)
Distance (m)

b)

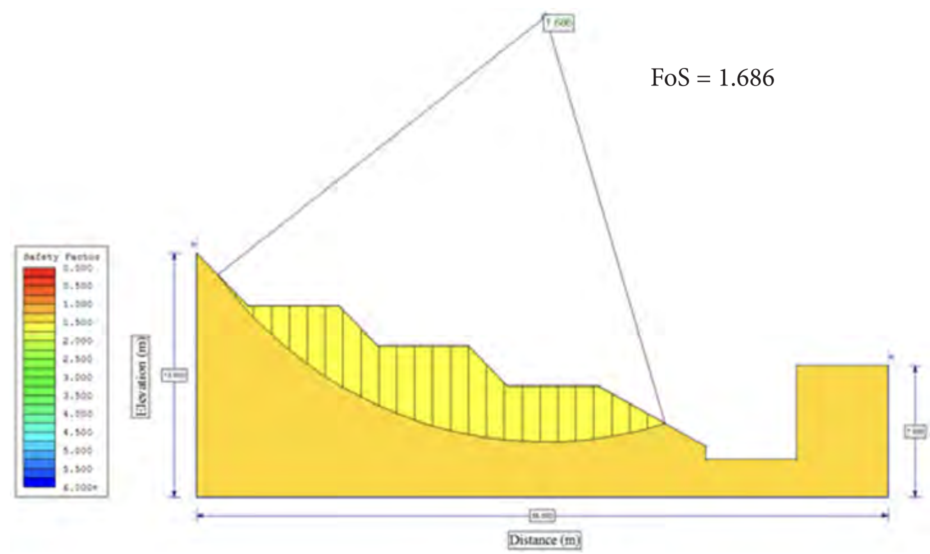
FoS = 1.686
Safety Factor
Elevation (m)
Distance (m)

c)

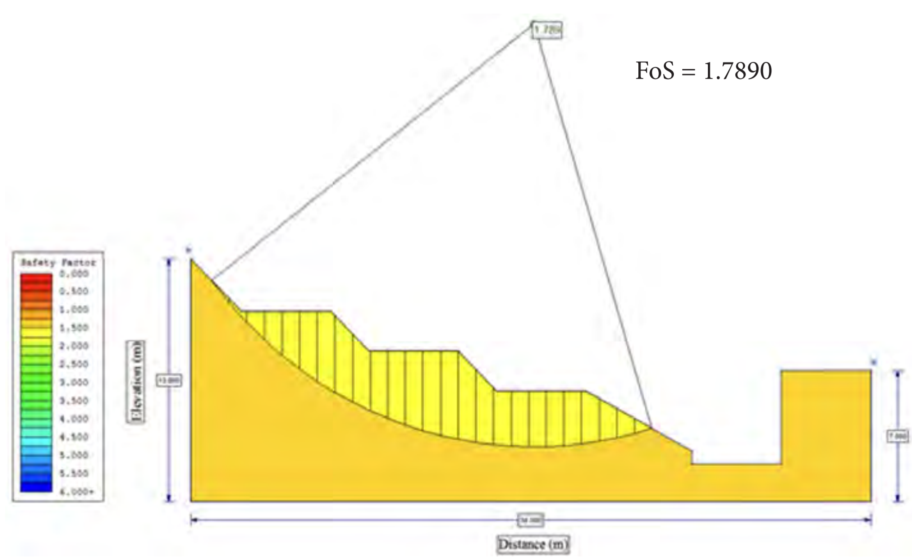
FoS = 1.7890
Safety Factor
Elevation (m)
Distance (m)

d)

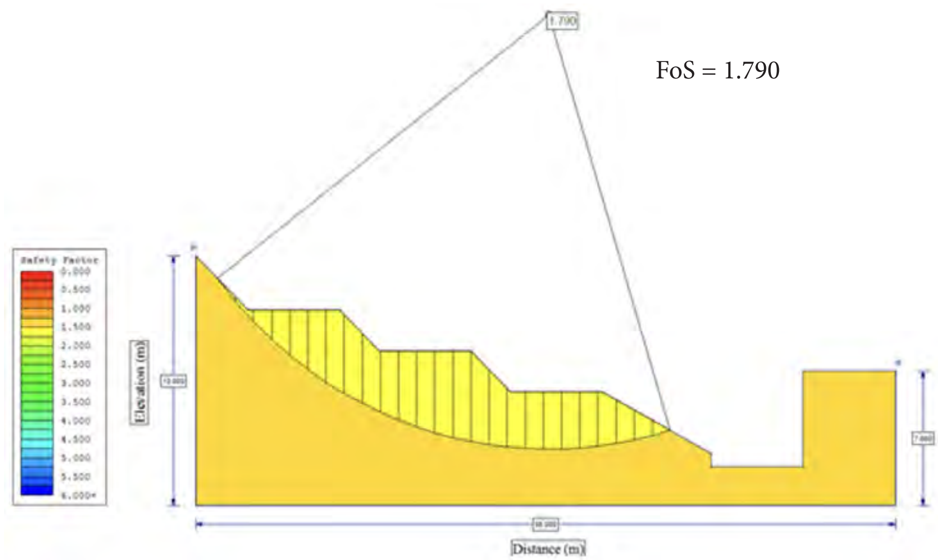

e)

Figure 7. Analysed slope: (a) Bishop's method, circular slip surface (b) Janbu Simplified method, circular slip surface, (c) Fellenius, circular slip surface, (d) Spencer method (e) GLE/Morgenstern-Price, circular slip surface.

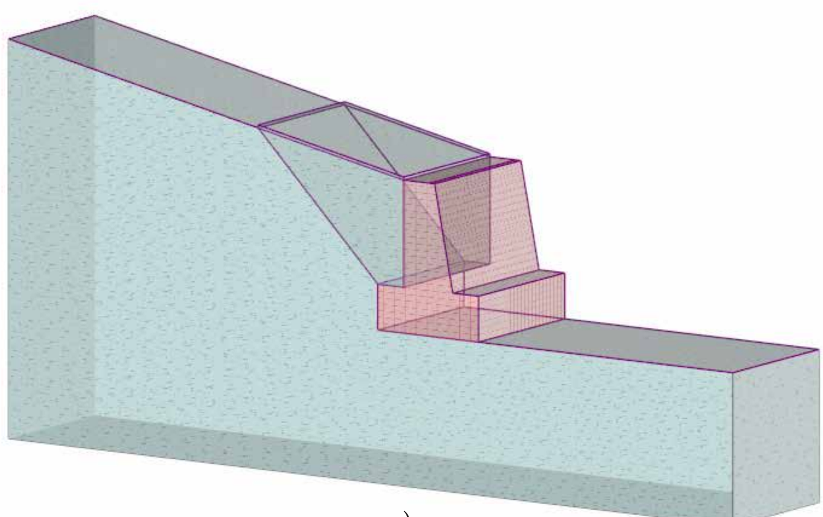

a)

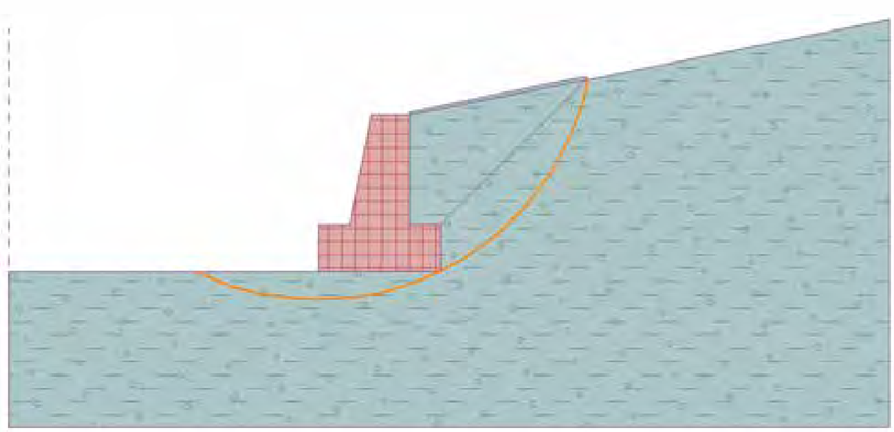

b)

Figure 8. Model geometry created in Geo5 software, a) three-dimensional visualization of the model, b) cross-section view of the model.

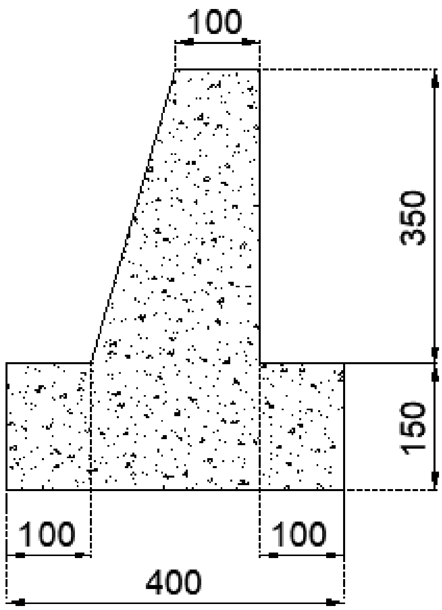

Figure 9. Cross-section of the retaining wall showing its dimensions (All dimensions are in cm).

Table 4. Engineering properties of the material of the retaining wall.

Concrete Class	Unit Weight (kN/m^3)	Young's Modulus (kN/m^2)	Poisson's Ratio	F_{ck} (MPa)	F_{yk} (MPa)
C 20/25	24	2.107	0.2	20	500

Table 5. FOS obtained using different methods for the retaining wall.

Method	Computed FoS
Bishop	1.580
Janbu-simplified	1.570
Fellenius	1.540
Spencer	1.570
GLE/Morgenstern-Price	1.570

5 COST ANALYSIS

A cost analysis for the proposed solutions was performed to identify the more economical solution. Table 6 and Table 7 summarise the works and the total costs for the proposed engineering solutions. The total costs are calculated for a 1-m unit length and the unit of currency is United States dollars (USD) in the analysis. As seen in Table 6, the total costs per unit length (USD/m) of the stepped excavation are calculated at 120.70 USD/m. Table 7 shows each work to be done for the construction of a retaining wall at the toe of the slope and their costs per unit length. The expense items can be grouped into six categories: (a) excavation, (b) concrete, (c) reinforcement, (d) labour cost, (e) backfill and compaction and (f) drainage works. The total costs for the construction of a retaining wall at the toe of the slope are calculated as 442.98 USD/m, as seen in Table 7. The first proposed solution – the stepped excavation – is much cheaper than the second proposed solution, which is the construction of a retaining wall at the toe of the slope.

Table 6. Total costs for the stepped excavation (costs per unit length).

Expense items	Cost (USD/m)
Excavation	120.70
	Total Cost = 120.70 USD/m

Table 7. Total costs for the construction of a retaining wall at the toe of the slope (costs per unit length).

Expense items	Cost (USD/m)
Excavation	11.27
Concrete	202.96
Reinforcement	134.72
Labour cost	88.01
Backfill and compaction	3.45
Drainage works	2.56
	Total Cost = 442.98 USD/m

It has been observed that slopes can be stable when inclined and stepped excavations are made in accordance with the technical conditions. It is also possible to detect this state of slopes using software programs. In this study, the cost of the stepped excavation was determined. For fine and coarse soils, excavation with machinery, loading on vehicles, transporting up to 25 meters, unloading, levelling, warehouse, and labour costs of 450 USD/m for 1 m^3.

According to the cost analysis, the retaining wall is more economical than the stepped excavation.

6 DISCUSSIONS AND CONCLUSIONS

A landslide failure occurred during the excavation of the transmission line of the Kars Dam. The landslide damaged the transmission line and stopped the excavation works for the transmission line. In this study, the slope stability after the excavation of the transmission line was investigated and it was found to be critically stable, since the value of the factor for the safety of the slope against failure is lower than 1.5. As a result of the slope-stability analysis, the landslide failure is predictable. Therefore, two different engineering solutions are proposed to avoid a possible landslide failure: (a) the stepped excavation to reduce the global inclination angle of the slope and (b) the construction of a retaining wall at the toe of the slope. A cost analysis of these proposed solutions is also made to specify a cheaper slope-stabilization method for this case. The slope-stability analysis shows that both engineering solutions can be used for the stabilization of the slope. The values of the factor of safety for the slope against the failure for both solutions are greater than 1.5. Therefore, both solutions can be used to avoid a possible landslide failure of the slope. Considering the cost analysis it is obvious that the stepped excavation is much cheaper than constructing a retaining wall at the toe of the slope. Specific to this problem, the stepped excavation is a better solution for the stabilization of the slope considering both safety and economy.

Data Availability Statement

All data, models and code generated or used during the study appear in the published article.

Acknowledgments

Finally, the authors would like to thank Selma Araz for providing data for this paper.

REFERENCES

[1] Guzzetti, F., Stark, C. P., Salvati, P. 2005. Evaluation of flood and landslide risk to the population of Italy. Environmental Management 36(1), 15-36. https://doi.org/10.1007/s00267-003-0257-1

[2] Plafker, G., Ericksen, G. E. 1978. Rockslides and avalanches 1 natural phenomena. Elsevier Scientific Publishing Company, England, 277-314.

[3] Akter, A., Johari, M., Mohd, M., Goto, M., Khanam, S., Parvez, A. 2019. Landslide disaster in Malaysia: an overview abstract. International Journal of Innovative Research and Development 8 (6), 292–302. https://doi.org/10.24940/ijird/2019/v8/i6/JUN19058

[4] Jibson, R. W. 2005. Landslide hazards at La Conchita, California. USGS Open-File Report 05-1067, 12.

[5] Evans, S. D., Guthrie, R.H., Roberts, N.J., Bishop, N.F. 2007. The disastrous 17 February 2006 rockslide-debris avalanche on Leyte Island, Philippines: a catastrophic landslide in tropical mountain terrain. Natural Hazards Earth System Science 7(1), 89-101. https://doi.org/10.5194/nhess-7-89-2007

[6] Inokuchi, T., Nakasu, T., Sato, T. 2011. Landslide disaster around Baguio city was caused by Typhoon Pepeng in 2009. Natural Disaster Research Report of the National Research Institute for Earth Science and Disaster Prevention 45, 35–41. https://doi.org/10.13140/RG.2.1.3866.0888.

[7] Martha, T.R., Govindharaj, K., B., Kumar, K.V. 2015. Damage and geological assessment of the 18 September 2011 Mw 6.9 earthquake in Sikkim, India using very high-resolution satellite data. Geoscience Frontiers 6(6), 793–805. https://doi.org/ 10.1016/j.gsf.2013.12.011

[8] Xu, C., Tian, Y., Zhou, B., Ran, H., Lyu, G. 2017. Landslide damage along Araniko highway and Pasang Lhamu highway and regional assessment of landslide hazard related to the Gorkha, Nepal earthquake of 25 April 2015. Geoenviromental Disasters 1–17. https://doi.org/10.1186/s40677-017-0078-9

[9] Montgomery, D.R. and Dietrich, W.E. 1994. A physically-based model for the topographic control on shallow landsliding. Water Resources Research 30(4), 1153–1171.https://doi.org/10.1016/j.enggeo.2004.01.011

[10] Malamud, B., D., Turcotte, D., L., Guzzetti, F., Reichenbach, P. 2004. Landslide inventories and their statistical properties. Earth Surface Processes and Landforms 29(6), 687–711. https://doi.org/10.1002/esp.1064

[11] Roering, J.J., Kirchner, J.W., Dietrich, W.E. 2005. Characterizing structural and lithologic controls on deep-seated landsliding: implications for topographic relief and landscape evolution in the Oregon Coast Range, USA. Geological Society of America Bulletin 117(5–6), 654–668. https://doi.org/10.1130/B25567.1

[12] Lourenço, D., N., Sassa, K., Fukuoka, H. 2006. Failure process and the hydrologic response of a two-layer physical model: implications for rainfall-induced landslides. Geomorphology 73(1–2), 115–130. https://doi.org/10.1016/j.geomorph.2005.06.004

[13] Vorpahl, P., Elsenbeer, H., Märker, M., Schröder, B. 2012. How can statistical models help to determine driving factors of landslides. Ecological Modelling 239, 27–39. https://doi.org/10.1016/j.ecolmodel.2011.12.007

[14] Zhang, F., Chen, W., Liu, G., Liang, S., Kang, C., He, F. 2012. Relationships between landslide types and

topographic attributes in a loess catchment, China. Journal of Mountain Science 9(06), 742–751. https://doi.org/10.1007/s11629-012-2377-7

[15] Rodriguez, C.E., Bommer, J.J., Chandler, R.J. 1999. Earthquake-induced landslides: 1980–1997. Soil Dynamics and Earthquake Engineering 18(5), 325-346. https://doi.org/10.1016/S0267-7261(99)00012-3

[16] Romeo, R. 2000. Seismically induced landslide displacements: a predictive model. Engineering Geology 58(3–4), 337–351. https://doi.org/10.1016/S0013-7952(00)00042-9

[17] Jaboyedoff, M., Michoud, M., Derron, M. H., Voumard, J., Leibundgut, G., Sudmeier-Rieux K., Nadim, F., Leroi, E. 2016. Human-induced landslides: toward the analysis of anthropogenic changes of the slope environment. International Journal of Rock Mechanics and Mining Sciences & Geomechanics Abstracts CRC Press 217-232. https://doi.org/10.1201/b21520-20

[18] Korucu, S. and Onur, M.İ. (2019). A landslide model study. International Conference on Innovation, Sustainability, Technology, and Education in Civil Engineering, İskenderun, Turkey.

[19] Mikoš, M., Četina, M., Brilly, M. 2004. Hydrologic conditions responsible for triggering the Stože landslide. Slovenia. Engineering Geology 73(3), 193–213. https://doi.org/10.1016/j.enggeo.2004.01.011

[20] Salciarini, D., Godt, J.W., Savage, W.Z., Conversini, P., Baum, R.L., Michael, J.A. 2006. Modeling regional initiation of rainfall-induced shallow landslides in the eastern Umbria region of central Italy. Landslides 3(3), 181–194. https://doi.org/10.1007/s10346-006-0037-0

[21] Guthrie, R.H. and Evans, S.G. 2010. Analysis of landslide frequencies and characteristics in a natural system, coastal British Columbia. Earth Surface Processes and Landforms 29(11), 1321–1339. https://doi.org/10.1002/esp.1095

[22] Jemec, M. and Komac, M. 2013. Rainfall patterns for shallow landsliding in perialpine Slovenia. Natural Hazards 67(3), 1011–1023. https://doi.org/10.1007/s11069-011-9882-9

[23] Bordoni, M., Meisina, C., Zizioli D., Valentino, R., Bittelli M., Chersich S. 2014. Rainfall-induced landslides: slope stability analysis through field monitoring. Landslide Science for a Safer Geoenvironment 273-279. https://doi.org/10.1007/978-3-319-04996-0_42

[24] Feizizadeh, B., Roodposhti, M. S., Jankowski, P., Blaschke, T. 2014. A GIS-based extended fuzzy multi-criteria evaluation for landslide susceptibility mapping. Computers and Geosciences 73, 208-221. https://doi.org/10.1016/j.cageo.2014.08.001.

[25] Lee, S., Dan, N. T. 2005. Probabilistic landslide susceptibility mapping in the Lai Chau province of Vietnam: focus on the relationship between tectonic fractures and landslides. Environmental Geology 48(6), 778-787. https://doi.org/10.1007/s00254-005-0019-x.

[26] Talaei, R. 2014. Landslide susceptibility zonation mapping using logistic regression and its validation in Hashtchin Region, northwest of Iran. Journal of the Geological Society of India 84(1). https://doi.org/68-86. 10.1007/s12594-014-0111-5.

[27] Aghlmand, M., Onur, M. İ., Talaei, R. (2020). The use of analytical hierarchy process and geographic information systems in production of landslide susceptibility maps. the use of analytical hierarchy process and geographic information systems in production of landslide susceptibility maps. European Journal of Science and Technology Special Issue 224-230 (in Turkish).

[28] Google Maps 2021. Study Area. Available from https://www.google.com/maps/search/Kars+baraj/@40.7259416,43.1459981,14z (Accessed 8 June 2021).

[29] Aydemir, A., Bilim, F., Avci, B., Kosaroglu, S. 2020. Geophysical investigation of the geothermal potential under the largest volcanic cover in Anatolia: Kars plateau, NE Turkey. Pure and Applied Geophysics 177(2), 919-939. https://doi.org/10.1007/s00024-019-02317-x.

[30] Hammouri, N.A., Malkawi, A.I.H., Yamin, M.M.A. 2008. Stability analysis of slopes using the finite element method and limiting equilibrium approach. Bulletin Engineering Geology and the Environment 67, 471–478. https://doi.org/10.1007/s10064-008-0156-z.

[31] Ting, J. M. 1983. Geometric concerns in slope stability analyses. Journal of Geotechnical and Geoenvironmental Engineering 109(11). https://doi.org/10.1061/(ASCE)0733-9410(1983)109:11(1487).

[32] Duncan, J. 1996. State of the art: limit equilibrium and finite element analysis of slopes. Journal of Geotechnical and Geoenvironmental Engineering ASCE 122(7), 578–584. https://doi.org/10.1061/(ASCE)0733-9410(1996)122:7(577).

[33] Yu, H., Salgado, R., Sloan, W., Kim, J. 1998. Limit analysis versus equilibrium for slope stability. Journal of Geotechnical and Geoenvironmental Engineering, ASCE 124(1), 1–11. https://doi.org/10.1061/(ASCE)1090-0241(1998)124:1(1).

[34] Stark, T.D., Eid, H.T. 1998. Performance of three-dimensional slope stability methods in practice. Journal of Geotechnical and Geoenvironmental

Engineering, 124(11). https://doi.org/10.1061/(ASCE)1090-0241(1998)124:11(1049)

[35] Kim, J., Salgado, R., Yu, H. 1999. Limit analysis of soil slopes subjected to pore-water pressures. Journal of Geotechnical and Geoenvironmental Engineering, ASCE 125(1), 49–58. https://doi.org/10.1061/(ASCE)1090-0241(1999)125:1(49).

[36] Kim, J., Salgado, R., Lee, J. 2002. Stability analysis of complex soil slopes using limit analysis. Journal of Geotechnical and Geoenvironmental Engineering, ASCE 128(7), 546–557. https://doi.org/10.1061/(ASCE)1090-0241(2002)128:7(546).

[37] Stark, T.D., Ricciardi, P.J., Sisk, R.D. 2018. Case Study: Vertical drain and stability analyses for a compacted embankment on soft soils. Journal of Geotechnical and Geoenvironmental Engineering 144(2). https://doi.org/10.1061/(ASCE)GT.1943-5606.0001786.

[38] Fellenius, W. 1936. Calculation of stability of earth dams. Transactions, 2nd congress large dams, Washington, DC: 445–462.

[39] Bishop, W. 1955. The use of the slip circle in the stability analysis of slopes. Geotechnique 5(1), 7–17. https://doi.org/10.1680/geot.1955.5.1.7

[40] Janbu, N. 1973. Slope stability computations, embankment- dam engineering: Casagrande volume. John Wiley & Sons, Inc., New York 47-86.

[41] Spencer, E. 1967. A method of analysis of the stability of embankments assuming parallel inter-slice forces. Geotechnique 15, 11–26. https://doi.org/10.1680/geot.1967.17.1.11.

[42] Morgenstern, R., Price, V. 1965. The analysis of the stability of general slip surfaces. Geotechnique 15(1), 79–93. https://doi.org/10.1680/geot.1965.15.1.79.

[43] SLIDE: 2D Limit Equilibrium Slope Stability for Soil and Rock Slopes. 2006

[44] Geo 5, (2016), User's Guide-Edition 2016, Fine Ltd., 1332p

SEISMIC ASSESSMENT OF THE LEVEE SYSTEMS IN SOUTHERN CALIFORNIA

POTRESNA OCENA SISTEMOV NASIPOV V JUŽNI KALIFORNIJI

Mehrad Kamalzare *(corresponding author)*
California State Polytechnic University,
Civil Engineering Department,
Pomona, California, USA
E-mail: mkamalzare@cpp.edu

Luis Daniel Salgado Nunes
California State Polytechnic University,
Civil Engineering Department,
Pomona, California, USA

Elaine Vo
California State Polytechnic University,
Civil Engineering Department,
Pomona, California, USA

DOI https://doi.org/10.18690/actageotechslov.19.1.30-47.2022

Keywords

levee, seismic load, slope stability, risk analyses

Abstract

Levees protect agricultural fields and urban areas from frequent flooding and natural hazards. They are structures that must be carefully designed and very well maintained. The United States Army Corps of Engineers is a federal agency under the Department of Defense, responsible for the design and construction of levees in the United States. Major construction of the Santa Ana River levee occurred during the 1990s. Susceptible analysis and inspections to evaluate the actual conditions of the levee's structure have been performed by Orange County Public Works and USACE personnel. Earthquakes are very common in the state of California. Regardless of having a large or small effect, seismic activities can impact on the majority of structures built on the Earth's surface. One of the most efficient ways to assess a levee's structure and verify how it would behave during a severe seismic activity is to create a model using the same or similar design parameters as the actual construction and simulate the action of seismic waves on the embankment. In this study, structural and geotechnical information for the Santa Ana levee was identified and gathered based on USACE design criteria and soil parameters, and then a model was created, representing three different sections of the levee system. Seismic loads were then simulated using a numerical model to perform calculations involving different scenarios to determine the factor of safety. The results are presented and opportunities for further research are discussed. This can help to predict the critical sections of the levee in case similar incidents occur.

Ključne besede

nasip, potresna obtežba, stabilnost pobočja. analiza tveganja

Izvleček

Nasipi ščitijo kmetijska zemljišča in mestna območja pred pogostimi poplavami in naravnimi nesrečami. So inženirski objekti, ki jih je treba skrbno načrtovati in zelo dobro vzdrževati. Inženirski korpus ameriške vojske je zvezna agencija v okviru Ministrstva za obrambo, odgovorna za načrtovanje in gradnjo nasipov v Združenih državah. Večja gradnja nasipa reke Santa Ana je bila izvedena v devetdesetih letih prejšnjega stoletja. Analize občutljivosti in inšpekcijski pregledi za oceno dejanskih pogojev konstrukcije nasipov je izvedlo osebje Orange County Public Works in USACE. Potresi v zvezni državi Kalifornija so stalni in zelo pogosti. Potresni učinki lahko vplivajo na večino konstrukcij zgrajenih na zemeljskem površju, ne glede na obsežnost učinka potresa. Eden od najučinkovitejših načinov za oceno konstrukcije nasipa in preverjanja, kako bi se obnašal pri močni potresni aktivnosti, je izdelava modela z uporabo enakih ali podobnih projektnih parametrov dejanske konstrukcije in simulacija delovanja potresnih valov na nasip. V tej študiji so bile identificirane in zbrane konstrukcijske in geotehnične informacije o nasipu Santa Ana na podlagi meril načrtovanja USACE in parametrov zemljin. Nato je bil ustvarjen model, ki predstavlja različne dele sistema nasipa. Z uporabo numeričnega modela so bile simulirane potresne obtežbe in izvedeni izračuni, ki so vključevali različne scenarije za določitev faktorja varnosti. Predstavljeni so bili rezultati in možnosti za nadaljnje raziskave. Ugotovitve lahko koristno uporabimo pri napovedovanju kritičnih odsekov nasipa v podobnih slučajih.

1 INTRODUCTION

The integrity of the state and national system of levees and embankment dams is a crucial component in ensuring the safety of protected communities. Levees are constructed along watercourses to provide protection against floods. The failure of such systems due to natural or man-made hazards can have monumental repercussions, sometimes with dramatic and unanticipated consequences for human life, property and the economy of the states and the country [1]. The failure of levees during hurricane Katrina in 2005, which led to the catastrophic flooding of New Orleans, is a highly illustrative example. About 2000 people lost their lives due to the failure of the levees that were protecting the city, and the property damage was estimated at $81 billion (2005 USD) [2].

There are several other examples that reveal the critical role of levees and embankment dams, and how their failure impacts on people's lives and properties. There are nearly 22,530 km of levees under the jurisdiction of the U.S. Army Corps of Engineers (USACE) in the US, but this does not include what is believed to be more than 160,000 additional km of levees not covered by the USACE safety program. Some are little more than mounds of earth piled up more than a century ago to protect farm fields. Others extend for kilometers and are made of concrete and steel, with sophisticated pump and drainage systems. They shield homes, businesses and infrastructure such as highways and power plants. Figure 1(a) shows, in red, that 881 counties with a total population of 160 million in the United States are protected by these levees. Figure 1(b) presents a closer look at the levees in southern California, and the potential flood areas are indicated by purple.

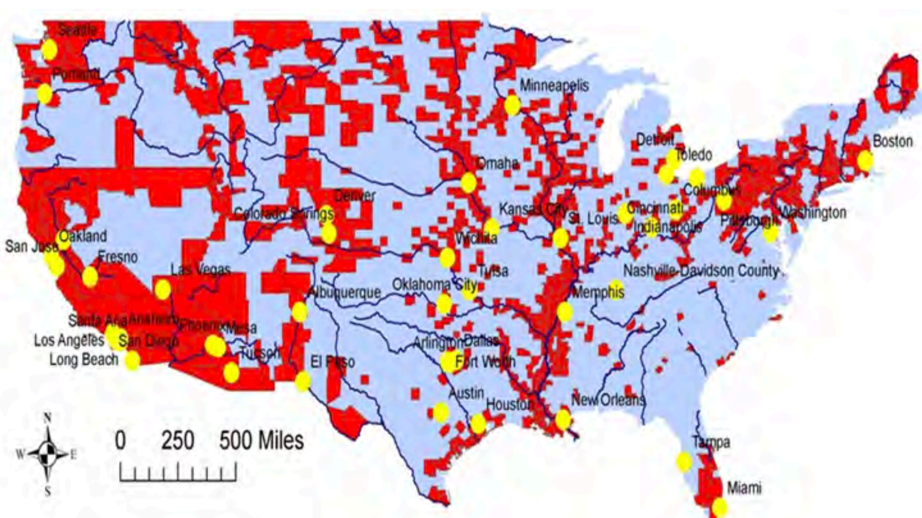

a)

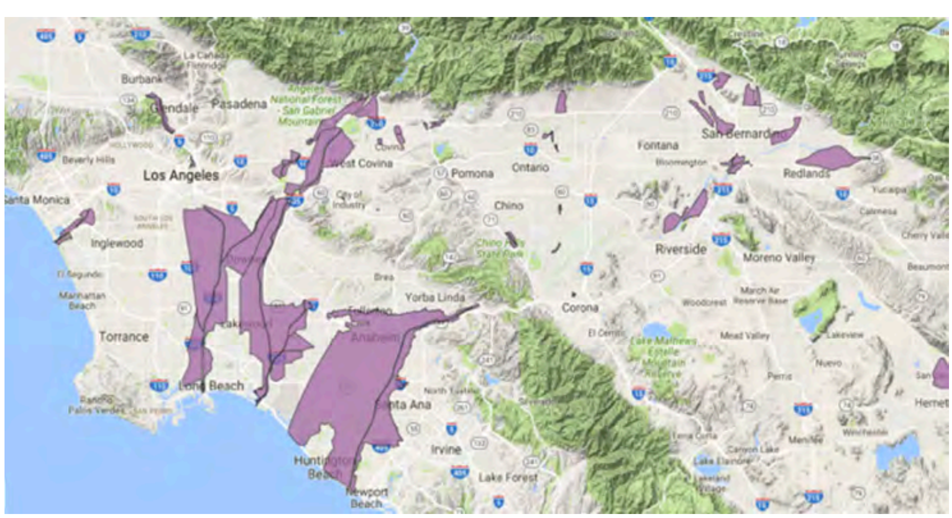

b)

Figure 1. Levee-protected areas: (a) national counties protected by levees, (b) areas in the Southern California protected by the levee system.

As can be seen from Figure 1(b), there are large areas of Orange County between the Los Angeles river and the Santa Ana river that are heavily populated and protected by levees. Although Southern California is at a lower risk of hurricane or typhoon compared to cities such as New Orleans, LA or Houston, TX, the existence of a large number of active faults, and the strong likelihood of earthquakes would make the assurance of a healthy and reliable levee system a very important matter for the State of California. In the case of an earthquake, the induced seismic forces, the failure of the slopes, and the ground rupture would be the main failure mechanisms. In the case of a hurricane or flood that happens relatively quickly, seepage and overtopping would be the most dominant and most probable failure mechanisms [3, 4, 5]. While other failure mechanisms require more time to significantly damage a levee, overtopping and seepage would erode the levee in a relatively short time, and the erosion would eventually lead to levee breach and failure [6]. Therefore, it is critical to investigate and assess the health of the system of levees in Southern California. This can help to identify the locations with the most critical problems in the levee system and accordingly take appropriate actions to minimize the risk of failure [7].

The objective of this project is to develop models that would simulate different failure seismic mechanisms of the levee and assess the outcome in order to verify the actual conditions of the levee system. The results can reveal the areas of the levees with higher risk in respect of overall stability, which can eventually lead to action plans for remediation and reduce the risk of failure in the case of an earthquake.

1.1 Historic background

The Santa Ana River Mainstream project is designed to provide flood protection for more than3.35 million residences and businesses in the Southern California communities of Orange, Riverside, and San Bernardino Counties. All three counties, collectively, are working closely with the U.S. Army Corps of Engineers (USACE) to design and construct the project [8].

A recommendation for the Santa Ana River Levee Mainstream Project emerged from studies involving the Federal Flood Control Act of 1936, together with the USACE, where it suggested a flood-control project to protect metropolitan Orange County and vicinal communities. The Los Angeles District Office then consolidated the studies in 1975. The goal of this study was to develop a plan to address the "Standard Project Flood", one that has about a half of one percent chance of occurring in any given year, or that statistically tends to occur about once every 200 years. The USACE was authorized by Congress in the Water Resources Development Act of 1976 to undertake the Phase 1 General Design Memorandum (GDM) for the project, which was completed in 1980. In 1986, the Phase 2 GDM (a more detailed study) was completed and submitted to Congress, requesting authorization for a "new construction start". The project was authorized for construction in 1988, and the three Local Sponsors (Flood Districts of Orange, Riverside and San Bernardino Counties) signed a Local Cooperation Agreement (LCA) with the USACE in 1989.

The LCA defined the roles and responsibilities for the project for the four parties. Construction began in 1989 with improvements to the Lower River near to the Pacific Ocean. The necessity of improvements and more specific studies towards the levee was found through technical analyses and inspections over the years. Nowadays, after more than 40 years, the improvements to the Santa Ana River system cover 120.7 km, from the headwaters of the Santa Ana River near Big Bear Lake to the mouth of the river at the Pacific Ocean between the cities of Newport Beach and Huntington Beach. Upon completion, the project will increase levels of flood protection to more than 3.35 million people and help to prevent over $40 billion in economic losses that could occur due to a major flooding event within the three-county area [9].

1.2. Literature review

It is important to understand the mechanisms of failure in a levee, the influence of flooding and how seismic forces impact on levees, and the negative effects on community and the economic losses. One of the studies of the probability of failure for Northern California Delta Levees was estimated by using simple statistical procedures based on empirical data. The levees, most of which are built on peat, are very variable with regard to composition, height and slope, and many reaches of the levees are only marginally stable. Factors affecting the likelihood of failure were mainly linked to the geometry and the heterogeneous mixture of various types of fill, including silt, sand and peat. To determine probabilistic studies, the author first combines information regarding the critical section of the levee with a factor of safety calculated using water-level data, the effective stress angle of friction, the levee's unit weight (seepage and levee-strength parameters). The author then uses these values and correlates with the peat-layer-thickness interval to formulate the average probability of failure [10].

Rapti et al. [11] simulated a levee-foundation system, and the influence of characteristics of the input ground motion, as well as of the position of the liquefied layer on the liquefaction-induced failure. The induced damage level (i.e., the induced crest settlements) in their studied levee model was strongly related to both the liquefaction apparition and the dissipation of excess pore-water pressure on the foundation. The respective role of the input ground-motion characteristics was a key component for soil-liquefaction apparition, as a long duration of the main shock can lead to important nonlinearity and extended soil liquefaction. A circular collapse surface was generated inside the liquefied region and extends toward the crest on both sides of the levee. Even so, when the liquefied layer was situated in depth, no significant effect on the levee's response was found. This research provided a reference case study for the seismic assessment of embankment-type structures subjected to earthquakes and proposed a high-performance computational framework that is accessible to engineers.

In recent decades we have seen a wide range of natural (e.g., floods and hurricanes) and technological disasters (e.g., hazardous material releases) in different countries. In particular, every year natural hazards have negative impacts on millions of people all over the world. Some natural hazards, which include a wide range of geophysical, meteorological, hydrological, climatological, or biological events that disturb human and natural environments, turn into disasters, causing physical impacts, such as injuries, casualties, and damage to property [12]. Levees are critical for providing protection against catastrophic flood events, and thus require continuous monitoring [13]. The long-term action of internal and external factors leads to constant seepage failures of soil-levee engineering, such as soil-flow failure and piping failure. It is very disadvantageous to the service safety of levee engineering. Most of the disastrous accidents are induced directly or indirectly by seepage. It has been known that the water–soil interaction with particle migration determines the occurrence and development of seepage failure [14].

The level of protection offered by an earthen levee is typically described in terms of flood-water level that the levee is capable of containing. If a larger flood occurs, floodwaters exceed the height of the levee and flow over its crest. As the water passes over the top, it can erode the levee, worsening the flooding and potentially causing a breach [15]. Waves overtopping a dike can cause erosion of the dike's cover, which can ultimately result in a dike breach. Flooding caused by a dike breach is one of the main hazards that can lead to large economic damage and human casualties worldwide as a result of serious inundations with disastrous effects. A recent example of such a disastrous event is Hurricane Katrina, which led to many dike breaches caused by wave overtopping. Due to these dike breaches, a large part of New Orleans was inundated [16]. There are several other studies that have shown flood impacts (risk and frequency) are even stronger nowadays, for several reasons, such as the increasing degree of urbanization, the existing infrastructure and possible disastrous impact of its effects on the environment, global warming, the increase in global atmospheric CO_2 concentration, etc. [17, 18, 19]. There is an emphasis on the importance of having a better understanding of the response of levees and dams to such events.

2 PROCEDURE AND THE STUDIED LEVEE

Since 1990 natural hazards have led to over 1.6 million fatalities globally, and economic losses are estimated at an average of around USD 260–310 billion per year. The scientific and policy communities recognize the need to reduce these risks [20]. Orange County Public Works states that the major flooding threat in Orange County is the Santa Ana River. In 1938 the Santa Ana River flooded parts of Anaheim, Santa Ana, and Garden Grove, reportedly killing more than 50 people. Although the Prado Dam helped to substantially reduce the flood damage, the 1969 storm caused the largest dollar loss in Orange County's history. Extensive efforts at flood protection have been made in the area in the past years; however, it appears that portions of the county, which would not be inundated by the river overflow during the 100-year event, could be subject to flooding from the overflow of storm-water drainage facilities that are presently inadequate for carrying the 100-year discharge. The East Garden Grove-Wintersburg Channel and Ocean View Channel system is one of the underlying channel systems of the Santa Ana River floodplain. This drainage system does not have the capacity to contain the 100-year flood because the channel banks and levees are overtopped at several locations [9].

These have made the Santa Ana levee system a crucial infrastructure for the region. In addition to these, seismic activities surrounding the Santa Ana Levee are also constant. A base local map (Figure 2) shows a scenario of how past and recent earthquakes are distributed along the Santa Ana River extension (and the Santa Ana levee system at the present time). The gray dots indicate the earthquake's position, and the size varies according to the quake's magnitude A 4.2 magnitude 3 km south of Fountain Valley, location 33.679°N 117.950°W, was found to be one of the biggest around the levee area in 1933 [21].

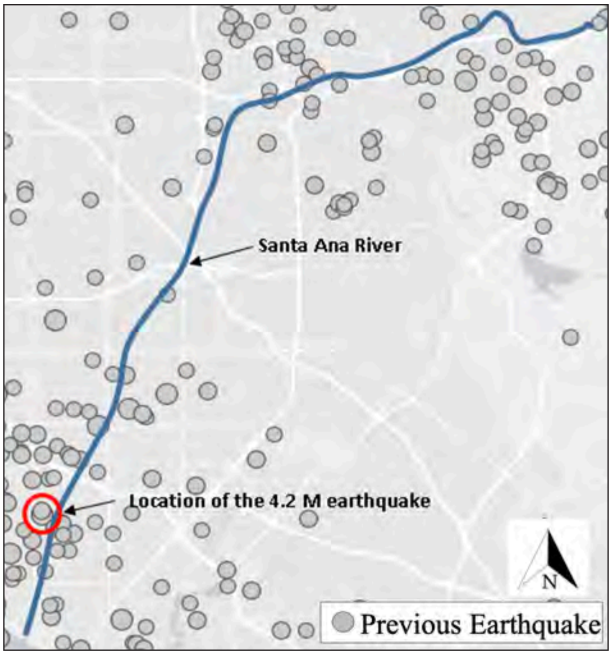

Figure 2. Previous earthquakes in the Orange County region.

Studies involving seismic activities and levee deformation gave support to the elaboration of this work concerning earthquake conditions and their implication for the structure of the levees. During the 1989 Loma Prieta earthquake, levees near Watsonville, California, spread laterally at multiple locations causing damage in an industrial facility and a dispute arose as to whether lateral spreading of the adjacent levee was the cause. In order to solve this conflict, stability analyses at four different pre-determined sites around the facility and for three sets of loading and soil-strength conditions were carried out. A first case analysis represents the pre-earthquake static loading conditions that aims to determine the factor of safety for several potential failure positions. A second case evaluates levee stability during an earthquake from pseudo-static procedures in which a horizontal seismic coefficient was applied to the potential sliding mass. The stability was evaluated based on the yield acceleration, as opposed to the factor of safety. The yield acceleration (k_y) is the horizontal acceleration (as a fraction of the vertical gravity force) at which the instability is initiated. After the initiation of the instability, movement then occurs along the critical failure surface. The estimated lateral spreading was determined using the relation of the yield acceleration versus the displacement developed [22].

To better analyze the Santa Ana levee, and due to its long extension, the levee was divided into three categories, as follows: SAR1 (Santa Ana River levee, section 1), SAR2 and SAR3 all federally authorized and subsequently constructed by the U.S. Army Corps of Engineers, Los Angeles District (USACE). The SAR1 is located on the right/west bank of the Santa Ana River in the cities of Santa Ana, Fountain Valley, and Huntington Beach (Figure 3(a)). The construction of the SAR1 was completed in September 1995 and is now entirely operated and maintained by Orange County Flood Control District (OCFCD) that is administered by Orange County Public Works (OCPW) staff, as for the SAR2 and SAR3 systems. The SAR1 Levee System consists of an earthen embankment with a trapezoidal channel lined with reinforced concrete and grouted riprap. Also, a rectangular channel lined with reinforced-concrete floodwalls and retaining wall, concrete masonry unit (CMU) retaining walls, 28 side drainage structure pipes, 18 discharge pipes, two side-drain junction structure pipes, four pump stations, numerous utility crossings, 20 bridge crossings, and 14 access ramps. The SAR1 Levee System extends from immediately upstream of Interstate 5 (I-5) to slightly downstream of the Pacific Coast Highway, a distance of approximately 18.8 km [23].

The SAR2 Levee System, (Figure 3(b)) is located on the left/east bank of the Santa Ana River in the cities of Costa Mesa and Newport Beach. The construction was completed in September 1992 and is composed of three levee segments: (1) the Santa Ana River 2a Levee Segment (i.e., the SAR2a Levee Segment); (2) the Santa Ana River 2b Levee Segment (i.e., the SAR2b Levee Segment); and (3) the Greenville-Banning Levee Segment (i.e., the GB Levee Segment). The SAR2 has an earthen embankment, concrete or riprap lined riverward side slopes, concrete lined or natural invert, seven side-drainage structures, two tide-gate assemblies, three side-drain junction structures, numerous utility crossings, one bridge crossing, and one access ramp.

The SAR2a Levee Segment forms the left/east bank of the Santa Ana River and extends from immediately downstream of the confluence of the Santa Ana River with the Greenville-Banning Channel to immediately downstream of the Pacific Coast Highway, converging at a distance of 1.9 km. The SAR2b Levee Segment forms the left/east bank of the Santa Ana River and extends from immediately downstream of Victoria Street/Hamilton Avenue to immediately upstream of the confluence of the Santa Ana River with the Greenville-Banning Channel, a distance of 0.4 km.

The SAR2b Levee Segment also forms the right/west bank of the Greenville-Banning Channel and extends from immediately downstream of Victoria Street/Hamilton to upstream of the confluence of the Santa Ana River with Greenville-Banning Channel, a distance of 0.5 km. The GB Levee Segment forms the left/east bank of the

Greenville-Banning Channel, and extends from immediately downstream of Victoria Street/Hamilton Avenue to immediately upstream of the confluence of the Santa Ana River with the Greenville-Banning Channel [23]. The SAR3 Levee System (Figure 3(c)) is located on the left/east bank of the Santa Ana River and on the left/east and right/west banks of the Greenville-Banning Channel (GB Channel) in the cities of Santa Ana and Costa Mesa. The construction of the SAR3 Levee System was completed in September 1995 and is composed of two levee segments: (1) the Santa Ana River 3 Levee Segment (i.e., the SAR3 Levee Segment), and (2) the Greenville-Banning Levee Segment (i.e., the GB Levee Segment). The SAR3 Levee System has an earthen embankment; a riverward slope armored with either grouted riprap, riprap, or reinforced concrete; an invert with either no lining, reinforced concrete lining, or derrick-stone lining; side-drainage structures; side-drain junction structures; utility crossings; bridge crossings; and access ramps.

The portion of the SAR3 Levee Segment along the Santa Ana River extends from the confluence of the Santa Ana River with Santiago Creek to Victoria Street, a distance of 14.7 km. The lower reach of the SAR3 Levee Segment consists of the left/east bank of the Santa Ana River and the right/west bank of the GB Channel. The

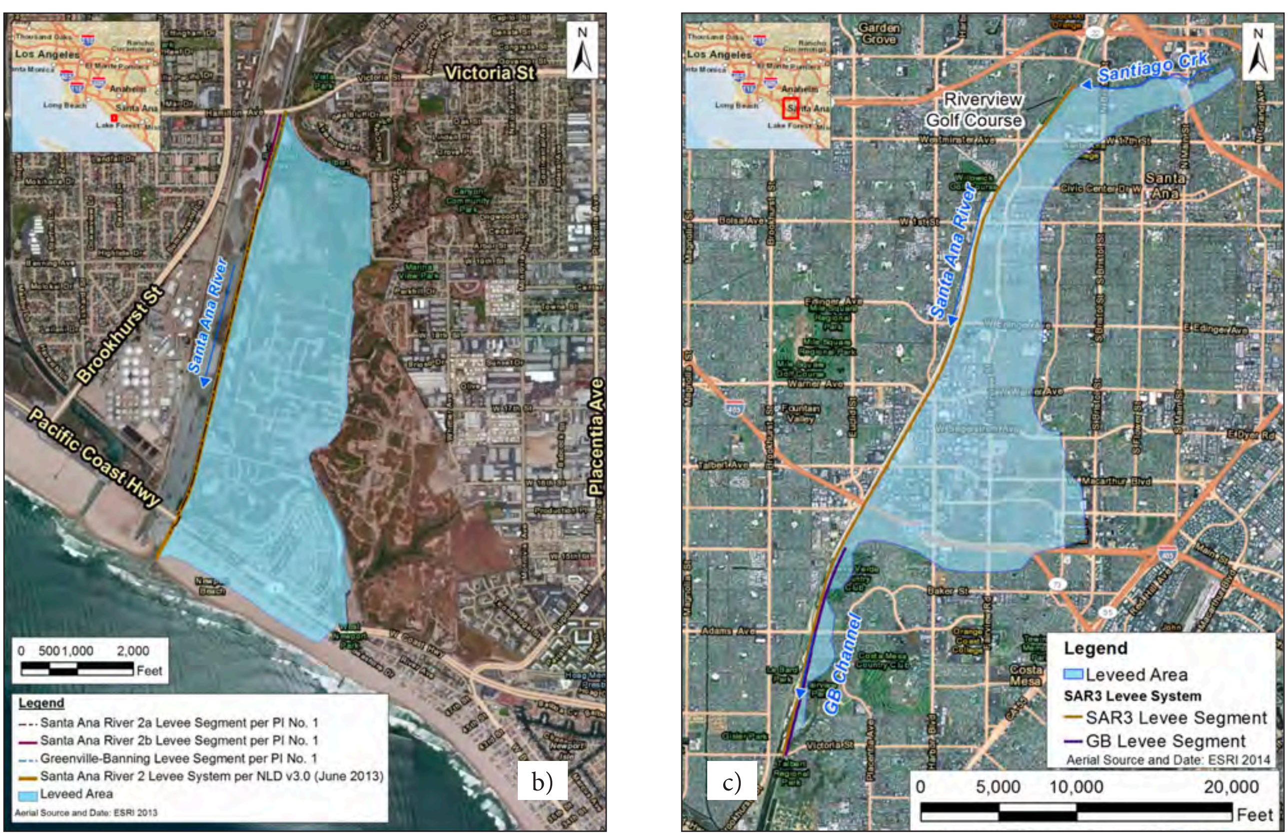

Figure 3. Major sections of the levee systems in Southern California, (a): SAR 1 Levee system; (b): SAR 2 Leveed area; (c): SAR 3 Leveed area.

portion of the SAR3 Levee Segment, which coincides with the GB Channel, extends from where the GB Channel begins to parallel the Santa Ana River to Victoria Street, a distance of 4.6 km. The GB Levee Segment forms the left/east bank of the GB Channel and extends from where the leveed condition begins along the left/east bank of the GB Channel to Victoria Street, a distance of 4.3 km. Previous to the construction of the Santa Ana River Project, GB Channel also ran parallel to the Santa Ana River, but discharged directly into the Pacific Ocean. As part of the Santa Ana River Project, the GB Channel was redesigned to discharge into the Santa Ana River just downstream from the Hamilton-Victoria Avenue. The GB Channel runs parallel to the Santa Ana River instead of entering into the Santa Ana River further upstream to maintain the interior drainage along the GB Channel, which has a lower invert elevation compared to the Santa Ana River along most of the reach [23].

The SAR1 Levee System is in fairly close proximity to several active and potentially active faults (Figure 4). Current State of California legislation defines an active fault as a fault that shows evidence of surface displacement during the Holocene (about the last 11,000 years). A potentially active fault is defined by the state as exhibiting evidence of surface displacement within the Quaternary (about the last 1.6 million years). These definitions are used as a basis for delineating Earthquake Fault Zones as mandated by the Alquist-Priolo Act Geologic Hazards Zones Act of 1972 and subsequent revisions (1975, 1985, 1990, 1992 and 1994) [24]. The intent of the act is to assure that urban development and certain habitable structures and sensitive improvements are not constructed across traces of active faults.

The Newport-Inglewood fault zone, which extends from possibly Baja California (Rose Canyon segment extending from the San Diego to offshore Orange County) to at least Santa Monica in Los Angeles County is the predominant structural/tectonic feature to cross the Santa Ana River. The zone is approximately 6.4 km wide near the mouth of the river (Santa Ana Gap). It is characterized by generally northwest-trending parallel faults and folds. Within the Gap (downstream of the I-405), at least six splays or segments of the fault have been mapped (Figure 5).

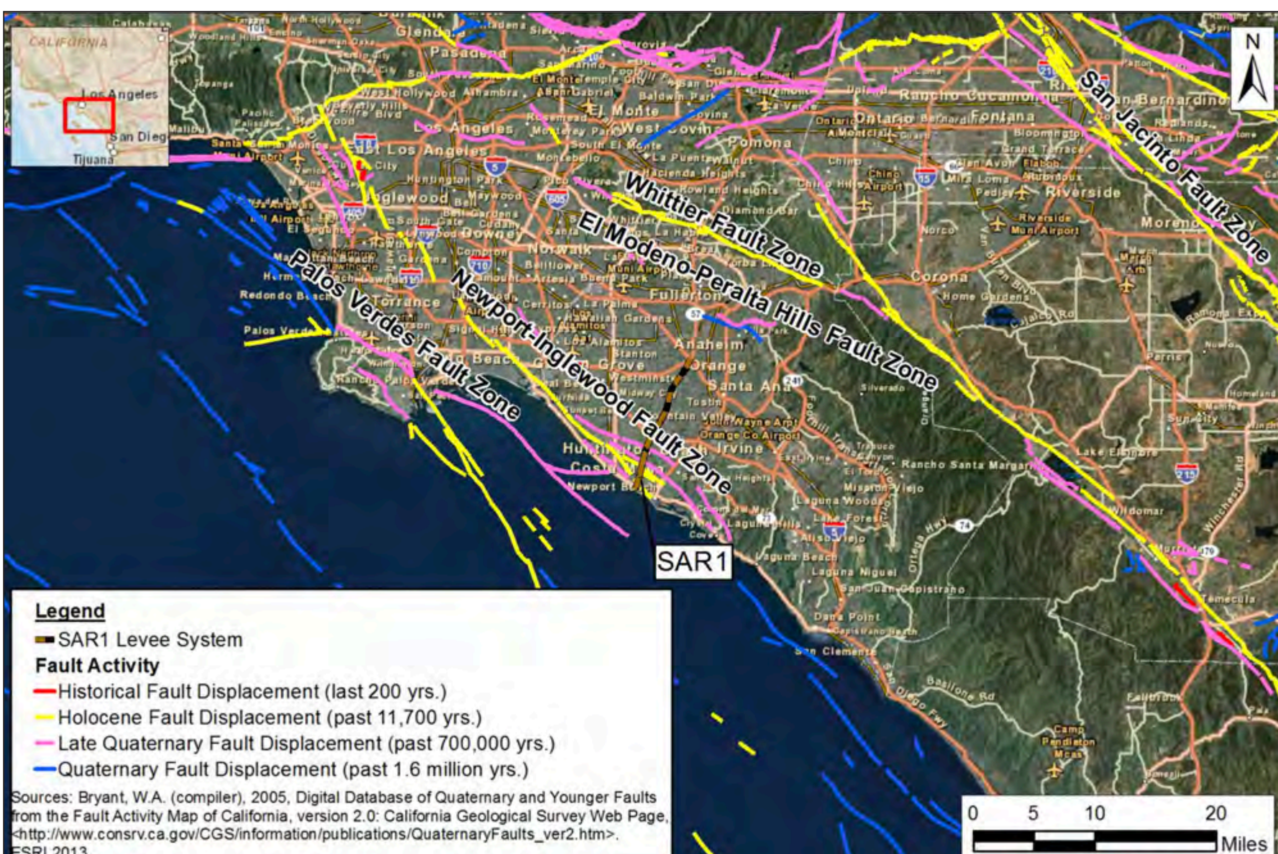

Figure 4. Regional fault map.

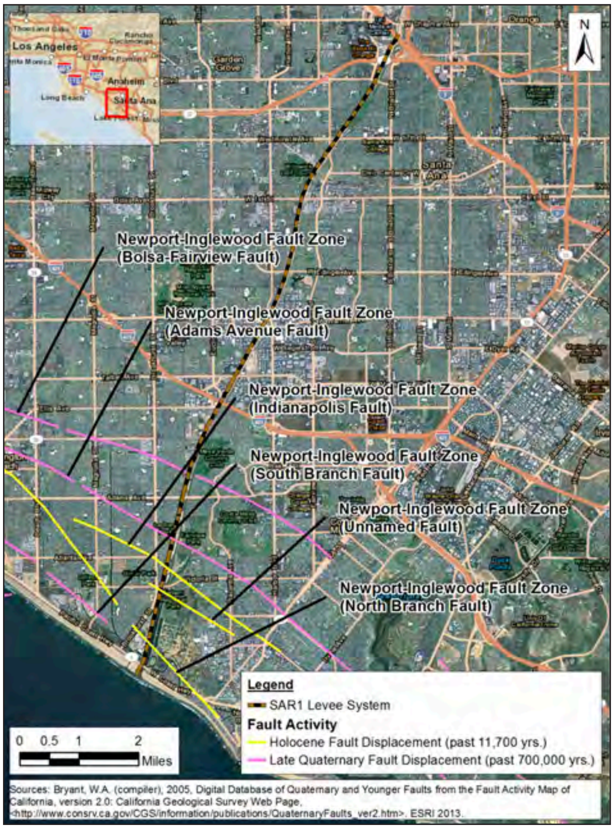

Figure 5. Local fault map.

The SAR Levee System is located within the seismically active Southern California region and is subjected to seismic forces along local and more distant regional faults. Some of the most significant seismically active faults near the levee alignment include the Newport Inglewood fault, the Palos Verdes fault, and the San Joaquin fault; although earthquakes on the Whittier, Elsinore, Sierra Madre, San Andreas, as well as other major fault systems within southern California, could also cause significant ground shaking along the levee alignment. In order to assess the historic ground shaking in the area of the SAR Levee System, monitoring data from earthquake-recording stations near to the project site were reviewed at the Center for Engineering Strong Motion Data website. Table 1 presents summarized data for the peak ground acceleration (PGA) noted nearby some of the levee stations during historical earthquake events [23].

3 MATERIALS AND METHODS

This portion aims to explain the methodology used to build the levee models and the criteria used to evaluate the system when subjected to seismic forces. Three main sections of the Santa Ana River Levee were chosen to be represented in the 2D model for further analysis using Slide Modeler software from the Rocscience package. The first section covers the downstream portion of the levee beginning on the Greenville-Banning channel area from station 20+00 and extends approximately 4.5 km towards upstream, where it meets the station 180+00 (Figure 6(a)). This section is inserted into the Newport-Inglewood-Rose Canyon fault zone where seismic activities are constant. The second section is the middle-stream portion. It represents the central part of the levee from stations 586+00 to 796+00 crossing the limits of Fountain Valley, Santa Ana and Orange cities (Figure 6(b)). There are no faults crossing the region of the chosen section; however, its proximity to the active El Modeno fault 1.6 km to the north, explains the occasional seismic activities in the region. The third section is located in the upstream portion from stations 796+00 to 1215+00 (Figure 6(c)). It mediates the cities of Placentia, Yorba Linda and Olive inserted on the Peralta Hills structure and near to other geologic formations with a high probability of ground shaking and intense seismic activities.

Subsurface investigations and laboratory testing were also used to evaluate the soil conditions. Exploratory borings were generally spaced at intervals of approximately 300 m or less. Boring depths varied from 8 m to

Table 1. Data of the recent earthquakes in Southern California.

Earthquake	Date	Magnitude	Station (CGS- CSMIP)*	PGA (g)	Minimum Distance from Station to Levee (km)
Chino Hill	July 29, 2008	5.4	13884	0.13	1.9
Irvine	Sept. 15, 2011	3.5	13891	0.08	1.5
Inglewood	May 17, 2009	4.7	13887	0.10	1.5
Northridge	Jan. 17, 1994	6.7	5465	0.16	1.0
Whittier Narrows	Oct. 1, 1987	5.9	13197	0.05	4.3
Landers	June 28, 1992	7.3	13160	0.07	4.8

*CGS-CSMIP California Geological Survey – California Strong Motion Instrument Program

a)

b)

c)

Figure 6. Different sections of the Santa Ana River Levee system;
(a) Section 1, Downstream;
(b) Section 2, Middle-stream;
(c) Section 3, Upstream.

over 21 m. The soils encountered during the investigation generally included varying percentages of sand, silt and clay. Given the fairly broad range of material types, the USACE LAD conducted an extensive laboratory program that included dry density, moisture content, maximum density, Atterberg limits, gradation, and shear-strength testing with its values summarized and presented in Table 2. Based on this testing, parameters were established for the various material types encountered along the levee's alignment. The strength tests were performed on samples remolded to both 80 and 90 percent of the maximum density as per the ASTM D1557 test method in order to evaluate loose foundation conditions and dense foundation/compacted fill conditions, respectively. The values were estimated for both the total-stress (R) and the effective-stress (S) conditions [23].

3.1 Geometry

The Santa Ana Levee geometry is in accordance with the EM 1110-2-1913, United States Army Corps of Engineer

Table 2. Summary of soil parameters.

Design Parameter	$\gamma_{d(max)}$ (kN/m^3)	w_{Opt} (%)	R Strengths				S Strengths				γ - (80%) (kN/m^3)			γ - (90%) (kN/m^3)		
			80% Compaction		90% Compaction		80% Compaction		90% Compaction							
			φ (deg)	c (kPa)	φ (deg)	c (kPa)	φ' (deg)	c' (kPa)	φ' (deg)	c' (kPa)	γ_d	γ_{wet}	$\gamma_{sat.}$	γ_d	γ_{wet}	$\gamma_{sat.}$
Clay	19	11	15	28.7	23	28.7	24	9.6	30	9.6	15.6	17.1	19.5	17.4	19.3	20.7
Silt	18.4	12	20	9.6	25	19.2	26	3.8	32	4.8	14.8	16.4	19.2	16.5	18.4	20.3
Silty Gravelly Sand	20.4	8	28	0	35	0	32	0	37	0	16.3	17.5	12.8	18.4	19.9	21.4
Sand	18.5	13	27	0	33	0	31	0	36	0	14.8	16.7	19.2	16.7	18.9	12.9
Silty Sand	18.7	12	24	9.6	30	14.4	28	0	34	0	14.9	16.8	19.3	16.8	19.0	20.4
Sand/Silty Sand	19.3	11	26	0	32	0	30	0	35	0	15.5	17.1	19.4	17.4	19.2	20.6
Clayey Sand	20.4	8	22	14.4	27	19.2	26	4.8	32	4.8	16.4	17.6	20.1	18.4	19.9	21.4

Table 3. Geometric parameters used in the numerical models.

Section	Slope	Width (m)	Height (m)
Downstream	2H:1V	7.6	4.9
Middle stream	2H:1V	10.7	6.7
Upstream	2H:1V	4.6	5.5

Design and Constructions of Levees manual, which indicates a minimum crown width of 3 m and also states that the levee should have side slopes flatter than or equal to 2H:1V. The actual levee geometry meets the manual requirements, having an approximately 6 m average crown width and the majority of the slopes measured along its extension of 2H:1V; however, slopes measuring 3H:1V and 1.5H:1V were also found. The actual levee height varies from 1 to 8 m. An average measurement of height was taken for each of the three sections as well as measurements of the slope and crown width further considered to build the numerical model. Table 3 presents the geometric parameters used to build the models for each section.

The external boundaries for the models were built using the 2D (x-y) cartesian coordinate system. The model was extended vertically to six times the embankment height, from the top of the levee crown to the bottom boundary line, and horizontally three times the value of the channel width (riverward direction) and three times the embankment width (landward direction). This format was used in order to fit all the potential failure surfaces in the boundaries, which will be discussed further in the results and discussion.

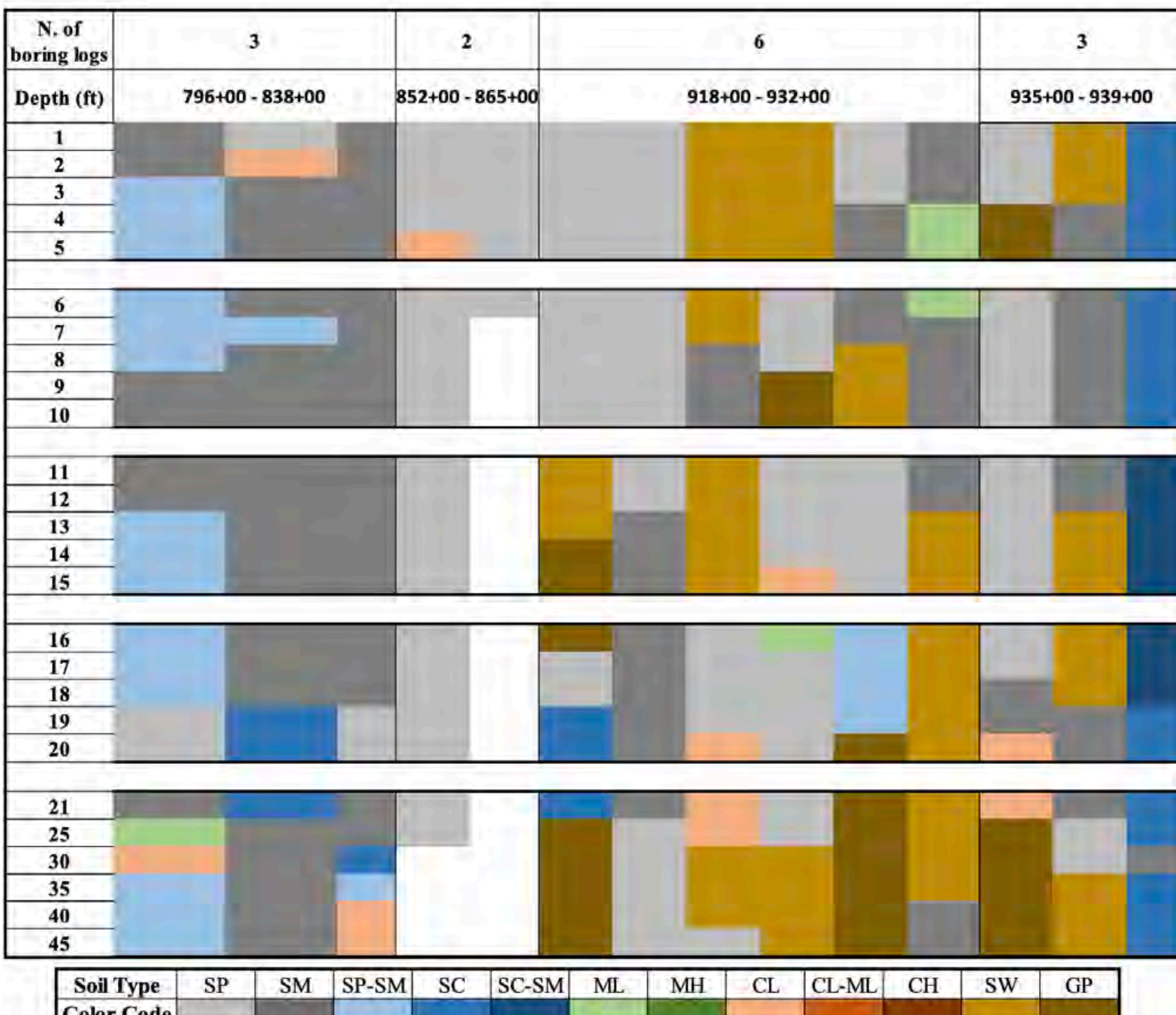

Figure 7. Analyses of the representative soil type and depths per station segments.

3.2 Levee Embankment Material Assignment

The type of soil encountered on the earthen embankment and the soil parameters (Table 2) were obtained through a sampling campaign conducted by the US Army Corps of Engineers and a contractor consulting company during the 1960s and 1970s. The majority of the test holes were set up alongside the channel and the rear side of the levee performed by a 15 cm (6 inch) rotary or a 40 cm (16 inch) bucket drilling machine. The soil used to build the embankment was originally from the channel excavation. Prior to the construction of the levees, these materials were tested, and later compacted and used to lift the layer during the levee's construction.

A statistical and quantitative method was developed in order to assign the embankment material in this study in such a way that each section chosen for modeling (downstream, middle stream and upstream) has its pre-defined initial and final stations. These stations set the limits of the sections. From the boring logs available, the depth and the corresponding types of soils were then statistically found. Thus, the station and the boring logs were identified and the values of the depth and soil type for each log were put together in a color-coded system for further quantitative analyses and the definition of the

Table 4. Number of soil-type occurrences per depth per station.

Depth (ft)	SP	SM	SM-SM	SC	SC-SM	ML	MH	CL	CL-MH	CH	SW	GP	Highest Occurrences	Representative Soil Type
1	9	6	0	3	1	0	0	0	0	0	11	2	11	
2	8	6	0	3	1	0	0	1	0	0	11	2	11	
3	8	6	1	3	1	0	0	0	0	0	11	2	11	SW
4	6	11	3	1	0	1	0	0	0	0	9	1	11	
5	5	11	3	1	0	1	0	1	0	0	9	1	11	
TOTAL	36	40	7	11	3	2	0	2	0	0	**51**	8		
6	8	11	3	1	0	1	0	0	0	0	8	0	11	
7	8	9	7	1	0	0	0	0	0	0	6	0	9	
8	8	10	6	2	0	0	0	0	0	0	5	0	10	SM
9	7	10	5	2	0	0	0	0	0	0	6	1	10	
10	10	9	5	1	0	0	0	1	0	0	4	1	10	
TOTAL	41	**49**	26	7	0	1	0	1	0	0	29	2		
11	11	8	5	0	1	0	0	1	0	0	5	0	11	
12	11	8	5	0	1	0	0	1	0	0	5	0	11	
13	8	6	2	0	1	0	0	0	0	0	13	1	13	SW
14	8	6	2	0	1	0	0	0	0	0	12	2	12	
15	6	6	2	0	1	1	0	1	0	0	12	2	12	
TOTAL	44	34	16	0	5	1	0	3	0	0	**47**	5		
16	8	5	2	1	1	2	0	0	0	0	9	2	9	
17	10	5	2	0	1	1	0	0	0	0	9	2	10	
18	10	6	2	0	1	1	0	0	0	0	9	1	10	SP
19	13	5	1	3	0	1	0	0	0	0	6	1	13	
20	12	4	0	3	0	1	0	2	0	0	5	3	12	
TOTAL	**53**	25	7	7	3	6	0	2	0	0	38	9		
21	10	6	0	3	0	1	0	2	0	0	5	3	10	
25	9	8	2	2	0	1	0	1	0	0	3	4	9	
30	3	8	1	2	0	1	0	1	1	0	5	5	8	
35	1	7	4	2	0	1	0	0	0	0	6	4	7	SM
40	1	9	2	2	0	1	0	1	0	0	4	5	9	
45	4	7	2	2	0	1	0	1	0	0	3	5	7	
TOTAL	28	**45**	11	13	0	6	0	6	1	0	26	26		

most suitable type of soil to represent the depths on each station, which were later incorporated into the model.

For instance, the third section (upstream) starts at station 796+00 and ends at station 1215+00. The first set of boring logs corresponds from station 796+00 to station 838+00. Three boring logs were analyzed in three columns with the associated depth and soil type represented by the color code. The second set of boring logs corresponds from station 852+00 to station 865+00 and two boring logs were available and analyzed in the same way. These analyses were performed on every segment until the last station (1215+00), which considered the available boring logs within the section limits. As an example, the final color-coded analyses results of a portion of the third section from station 796 to 939 are presented in Figure 7 (page 39).

This procedure was applied for every boring log and station available, involving each of the three sections. In order to determine the most appropriate representative material to be assigned in the model, the number of occurrences for each depth is summed and the total largest number is assumed to represent the soil type in the model (Table 4).

3.3 Numerical Model

The numerical models were created based on USACE drawings, the actual levee geometry and the measurements taken from in-person site visits as well as Google Earth images, using the 2D limit equilibrium analysis method and Rocscience software Slide2. With the assigned soil type and materials, seismic loads were then applied to the model. Figure 8 below shows an example of a levee's cross-section, the actual structure image and the model representing the upstream section.

In this project, three case scenarios considering different approaches are discussed: (1) Minimum factor of safety for critical slip surface, static load, (2) Application of pseudo-static seismic loads in the horizontal direction, assuming a seismic coefficient load of 0.15 (k_h), and its effect on the minimum safety factor, and (3) Critical seismic coefficient determination (k_c) that results in a destabilized slope with factor of safety equal to 1.0.

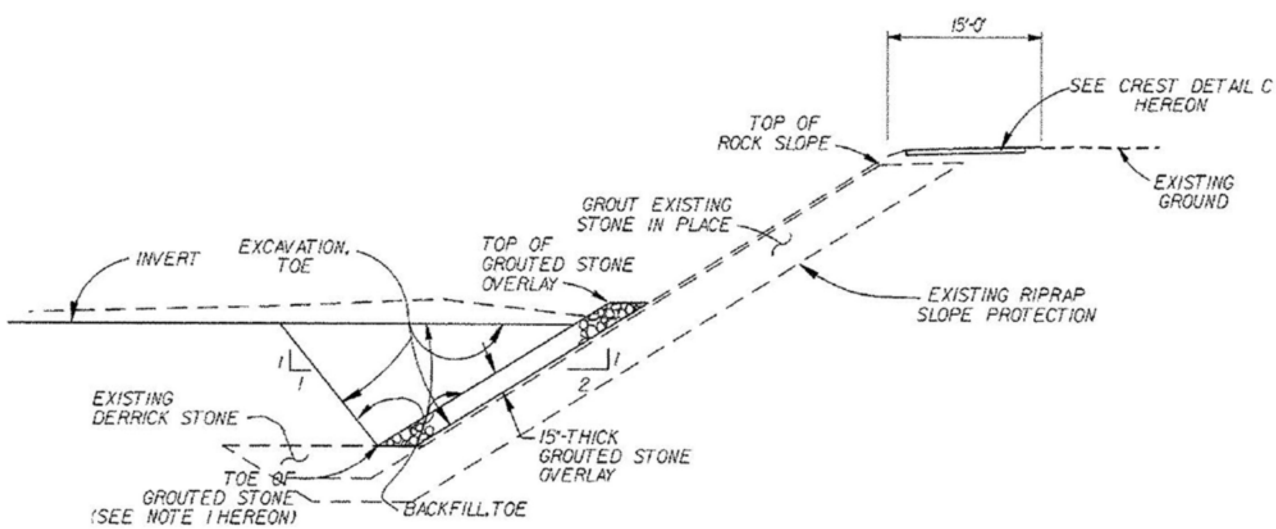

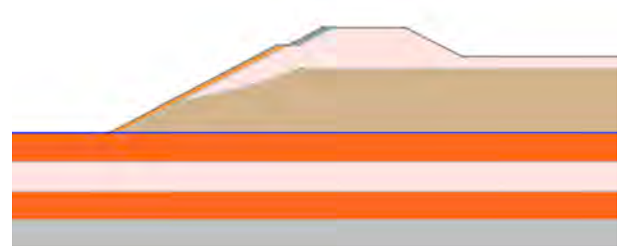

Figure 8. Upstream representation.

This work does not discuss methods to determine the seismic coefficient (k_h). Instead, it chooses 0.15 as a maximum value recommended for the design in the studied area by Melo and Sharma (2004) [25] and USACE (2014) [23]. It should be mentioned that the selection of an appropriate seismic coefficient is one of the most important and difficult aspects of a pseudo-static stability analysis. In theory, the seismic coefficient values should depend on some measure of the amplitude of the inertial force induced in the slope by the dynamic forces generated during an earthquake. Because soil slopes are not rigid and the peak acceleration generated during an earthquake lasts for only a very short period of time, seismic coefficients used in practice generally correspond to acceleration values well below the predicted peak accelerations. However, the choice of coefficients used in the slope-stability analysis is very subjective and lacks a clear rational [25]. There have also been other studies that identified the shear strength and seismic coefficient of levees by analyzing surficial slides during the 2004 Mid-Niigata Prefecture Earthquake, and researchers also chose 0.15 as a maximum value, recommended by the US Army Corps of Engineers for large earthquakes [26]. The selection of an appropriate seismic coefficient is critical in a pseudo-static stability analysis, mainly because in this method, the seismic loading is modeled as a statically applied inertial force, the magnitude of which is a product of the seismic coefficient, k, and the weight of the potential sliding mass [27].

4 RESULTS AND DISCUSSION

This study performed a qualitative and quantitative analysis approach to the Santa Ana River levee structure from a seismic activity perspective. The project has the intention to analyze the behavior of the levee, in terms of the factor of safety, when submitted to relevant magnitude seismic conditions.

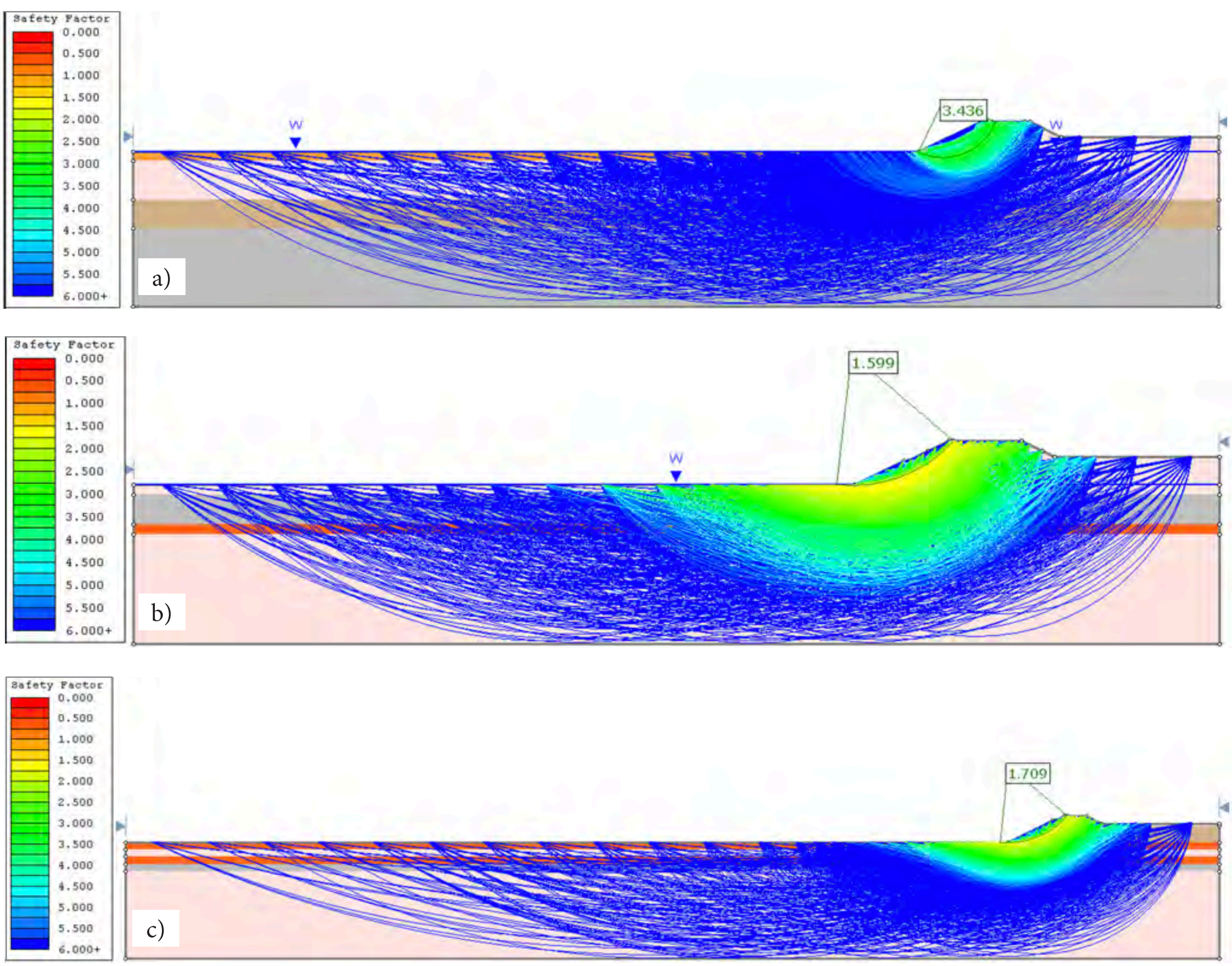

Figure 9. Different sections of the Santa Ana River (SAR) levee under static load (a) Downstream, (b) Middle stream, (c) Upstream.

4.1 Scenario 1 – Static Loading

This interpretation defines the critical slip surface and its safety factor. The downstream earthen levee model (Figure 9(a)) was considered to have a height and width of 4.8 m and 7.6 m respectively. The slope has an inclination of 2H:1V and a 1 m thickness of riprap revetment. After running the software interpretation, the factor safety found was 3.4. The middle stream earthen levee model Figure 9(b) has a total height of 6.7 m and a width of 10.7 m. The overall slope has an inclination of 2H:1V and it is divided in the middle by a 0.6 m wide berm. The slope has a 0.6 m thick reinforced-concrete revetment. After running the software interpretation, the factor safety found was 1.6. The upstream earthen levee model (Figure 9(c)) has a total height of 5.5 m and a width of 4.6 m, on average. The overall slope has an inclination of 2H:1V and it is also divided by a 0.6 m wide berm located 0.9 m below the levee crest.

Based on USACE cross-sections, a slope with 0.6 m of reinforced-concrete revetment (above the berm) and 0.6 m of riprap revetment below the berm was considered in the model. After running the software interpretation, the factor of safety was found to be 1.7.

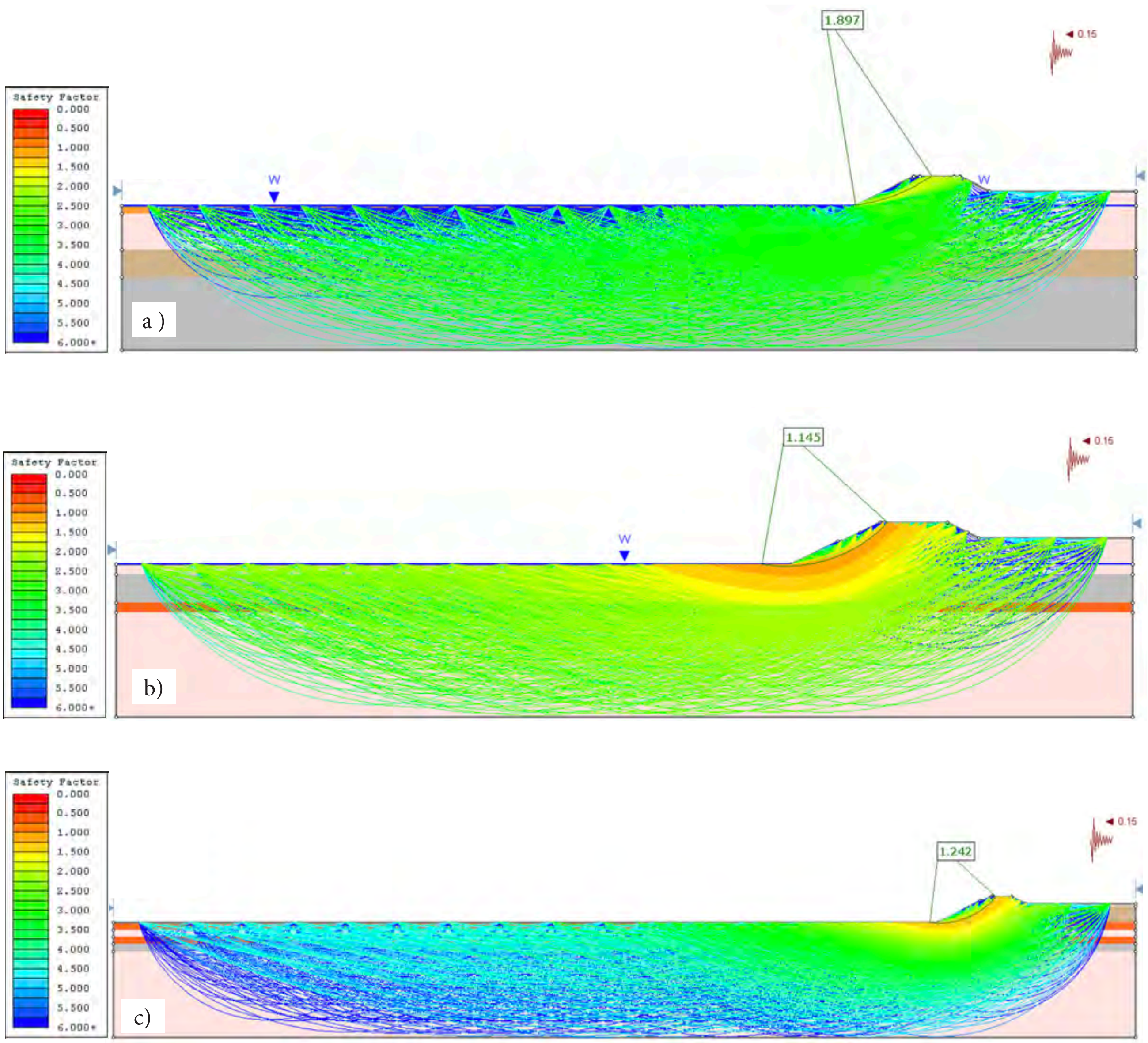

Figure 10. Different sections of the Santa Ana River (SAR) levee under Pseudo-static loading; (a) Downstream, (b) Middle stream, (c) Upstream.

4.2 Scenario 2 – Pseudo-Static Loading

This scenario shows the effect of pseudo-static earthquake loading in the limit equilibrium analysis. The orientation chosen in the software was the slip direction in lieu of trend/plunge and vector options. The slip-direction option automatically applies the horizontal seismic coefficient (k_h) in the direction of sliding (right to left), through the geometric centroid of each column. Seismic coefficients are dimensionless coefficients that represent the (maximum) earthquake acceleration as a fraction of the acceleration due to gravity. Usually, the factor of safety for ordinary static conditions must be at least 1.5, and the factor of safety from a pseudo-static analysis with a prescribed horizontal acceleration factor must be at least 1.1 [28].

Figure 10(a) shows the lines with different colors corresponding to the factor of safety, which for this case has a critical value of 1.9. The same procedure is applied for the middle-stream section, presenting a factor of safety of 1.15 (Figure 10(b)), and the upstream section Figure 10(c) with a factor of safety of 1.2.

4.3 Scenario 3 – Critical Seismic Coefficient Analysis

The safety factor was evaluated in the previous scenario for a horizontal seismic load coefficient (k_h) of 0.15. For this scenario, a set of reverse analyses was performed for each section of the levees to determine the critical seismic coefficient (k_c) that results in a destabilized slope for a factor of safety equals to 1.0. Figure 11 shows the outcome for each section.

A summary of all of the above-mentioned factors of safety along with the percentage of drops are presented in Table 5.

Table 5. FS of different sections of the SAR levee under static and pseudo-static loads.

	FS for static load	FS for static load	Drop percentage	Seismic coefficient k_h
Downstream	3.436	1.897	45 %	0.406
Middle stream	1.599	1.145	28 %	0.215
Upstream	1.709	1.242	27 %	0.262

4.4 Limitations

The most recent sampling campaign in the actual levee crest would be essential to determine accurate details about the soil type and its properties in various section of the levee. This study considered a statistical approach to determine the soil type for sections located relatively far away from each other. Although similar soils were used for this levee at various sections, the development of a more precise study of the Santa Ana levee/embankment soil type would lead to a more accurate model.
A verification of the model used in this study could be performed in order to verify its congruency with the actual levee. That would demand more planning and field visits, arrangements with the USACE inspectors or Orange County Public Work (OCPW) personnel on the areas that are restricted. A more site-specific determined seismic coefficient (k_h) would also lead to a more accurate result for each of the three sections.

5 CONCLUSIONS

This project evaluated the seismic behavior of the major Southern California levee systems. In particular, different sections of the Santa Ana River levee system were investigated. A set of selected sections of the structure were modeled by taking into consideration the effects of seismic loads for different conditions. Factors of safety for each scenario were then calculated for the levee-slope failures. The conclusions below can be drawn from this study:

1. The downstream section has the highest factor of safety and this might be justified due to its proximity to several active fault systems and the large number of previously recorded seismic activities.
2. The downstream section presents a higher percentage drop in the factor of safety (45 %) when experiencing seismic loads, it would still be within a safe range, assuming a minimum FS of 1.0 for static loads and 1.5 for pseudo-static loads.
3. The middle-stream section resulted in the lowest value for the factor of safety, both under static load (FS = 1.6) and pseudo-static loads (FS = 1.1). The values are very close to the acceptable limits.
4. The middle-stream section would require more attention and consideration for regular inspections and a further opportunity for a re-evaluation in terms of design.
5. The upstream FS values are also close to the limit values. The development of a future inspection plan would be strongly recommended for this section.

Data Availability

Some or all the data, models, or code that support the findings of this study are available from the corresponding author upon reasonable request.

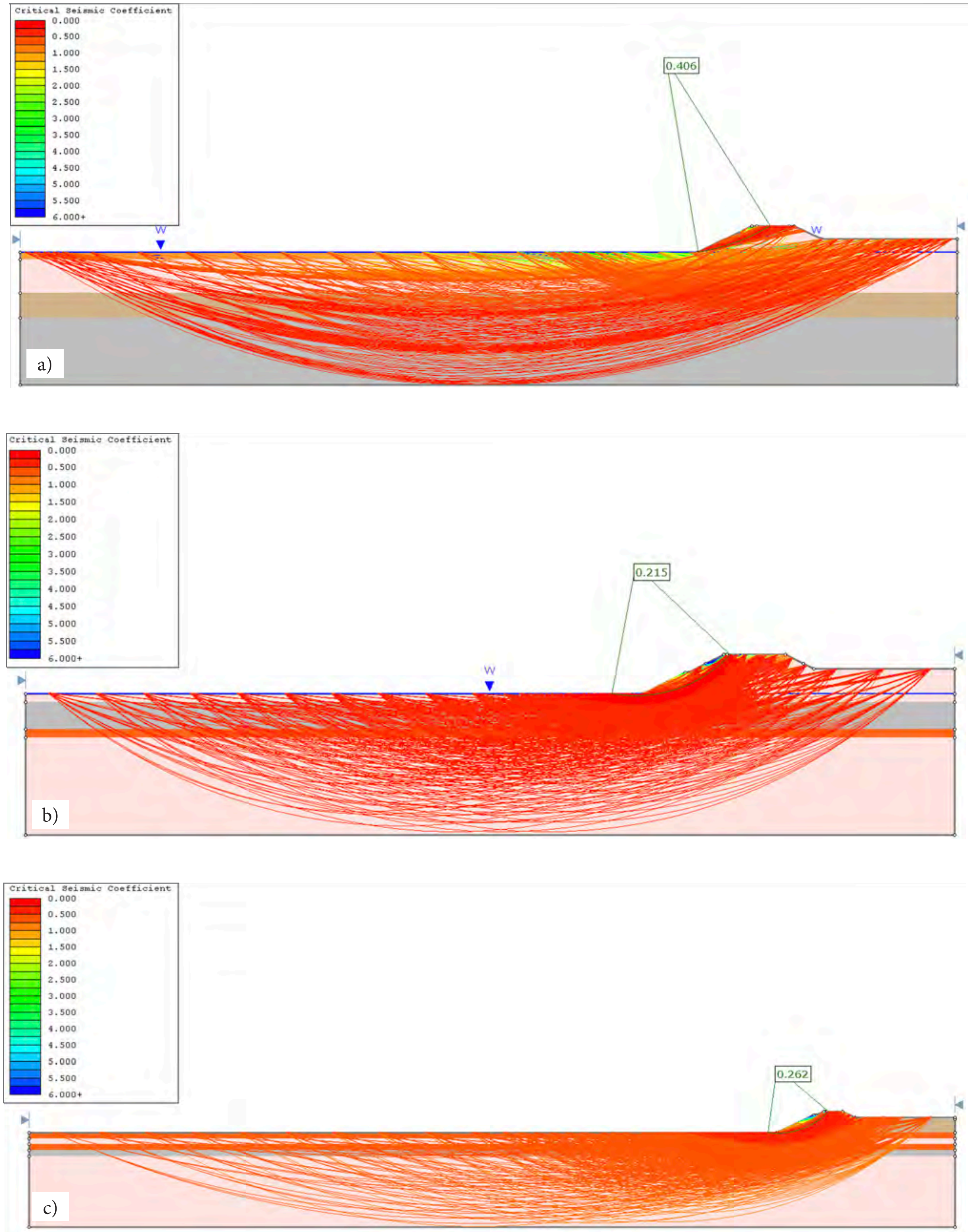

Figure 11. Different sections of the Santa Ana River (SAR) levee under Critical seismic coefficient: (a) Downstream, (b) Middle-stream, (c) Upstream.

REFERENCES

[1] Kamalzare, M., 2013, "Investigation of Levee Failure because of Overtopping and Validation of Erosion Evolution and Quantity," PhD dissertation, Department of Civil and Environ- mental Engineering, Rensselaer Polytechnic Institute, Troy, NY.
[2] Kamalzare, M., Chen, Z., Stuetzle, C., Cutler, B., Franklin, W. R., and Zimmie, T. F., 2011, "Computer Simulation of Over- topping of Levees," 14th Pan-American Conference on Soil Mechanics and Geotechnical Engineering (64th Canadian Geotechnical Conference), The Canadian Geotechnical Society, Toronto, Ontario, Canada.
[3] Kamalzare, M., Stuetzle, C., Chen, Z., Zimmie, T. F., Cutler, B., and Franklin, W. R., 2012a, "Validation of Erosion Modeling: Physical and Numerical," Geo-Congress, Oakland, CA, Mar 25–29, pp. 710–719.
[4] Kamalzare, M., Zimmie, T. F., Stuetzle, C., Cutler, B., and Franklin, W. R., 2012b, "Computer Simulation of Levee's Erosion and Overtopping," XII International Symposium on Environmental Geotechnology, Energy and Global Sustain- able Development, International Society for Environmental Geotechnology, Los Angeles, CA, June 27–29, pp. 264–273.
[5] Kamalzare, M., Han, T. S., McMullan, M., Stuetzle, C., Zimmie, T., Cutler, B., and Franklin, W. R., 2013a, "Computer Simulation of Levee Erosion and Overtopping," Proceedings of the Geo-Congress 2013: Stability and Performance of Slopes and Embankments III, San Diego, CA, Mar 3–7, pp. 1851–1860.
[6] Kamalzare, M., Zimmie, T. F., Han, T. S., McMullan, M., Cutler, B., and Franklin, W. R., 2013b, "Computer Simulation of Levee's Erosion and Overtopping," Proceedings of the 18th International Conference on Soil Mechanics and Geotechnical Engineering (ICSMGE), Paris, France, Sept 2–6.
[7] Marquez, H., and Kamalzare, M., 2019. "Geotechnical risk analyses and evaluation of design criteria of embankment dam systems", 7th International Symposium on Deformation Characteristics of Geomaterials, Strathclyde's Technology & Innovation Centre, Glasgow, UK.
[8] Howes, C., 2018. "Santa Ana River Project-Flood Control Improvements." SABPPrint Solutions, https://sabp.com/2018/07/16/santa-ana-river-project-flood-control-improvements/.
[9] Orange County Public Work, 2009. Orange County, California - Santa Ana River Project (SARP). Retrieved Jan. 31, 2019, from http://www.ocpublicworks.com/gov/pw/flood/sarp/.
[10] Duncan, J., and Houston, W., 1983." Estimating Failure Probabilities for California Levees." Journal of Geotechnical Engineering, vol. 109 (2) ASCE, pp. 260–268.
[11] Rapti, I., Lopez-Caballero, F., Modaressi, A., Foucault, A., and Voldoire, F., 2018, "Liquefaction Analysis and Damage Evaluation of Embankment-Type Structures." Acta Geotechnica, vol. 13, (5), pp. 1041-1059. doi: http://dx.doi.org.ezproxy.cyclib.nocccd.edu/10.1007/s11440- 018-0631-z.
[12] Shen, R., Huang, A., Li, B. and Guo, J., 2019, "Construction of a drought monitoring model using deep learning based on multi-source remote sensing data." International Journal of Applied Earth Observation and Geoinformation, vol. 79 (1), pp. 48-57. doi:10.1016/j.jag.2019.03.006
[13] Ozer, I., Rikkert, S., Leijen, V., Jonkman, F., and Hanssen, S., 2019, "Sub-seasonal Levee Deformation Observed Using Satellite Radar Interferometry to Enhance Flood Protection." Scientific Reports, report 9, article no. 2646. Doi: https://doi.org/10.1038/s41598-019-39474- x
[14] Huaizhi, S., Zhaoqing, F., Gao, A., Zhiping, W. 2017, "Particle Flow Code Method-Based Meso-Scale Identification for Seepage Failure of Soil Levee." Transport in Porous Media, vol. 119, no. 2, pp. 311-336.
[15] Balistrocchia, M., Moretti, G., Orlandini, S., Ranzi, R., 2019, "Copula-Based Modeling of Earthen Levee Breach Due to Overtopping." Advances in Water Resources, vol. 134. doi: https://doi.org/10.1016/j.a dvwatres.2019.103433.
[16] Bomers, A., Lopez, A., Warmink, J., Hulscher, S., 2018, "Modelling Effects of an Asphalt Road at a Dike Crest on Dike Cover Erosion Onset during Wave Overtopping." Natural Hazards, vol. 93, no. 1, pp. 1-30. doi: http://dx.doi.org.ezproxy.cyclib.nocccd.edu/10.1007/s11 069 - 018-3287-y.
[17] Franczyk, A., Slipek, M., and Dwornik, M., 2018, "Application Of Morris Method Of Sensitivity Analysis to Flood Embankment Stability Modelling". 18th International Multidisciplinary Scientific Geo-Conference, vol. 18, pp. 81-88, Sofia, Bulgaria.
[18] Ferrari, A., Dazzi, S., Vacondio, R., and Mignosa, P., 2020, "Enhancing the Resilience to Flooding Induced by Levee Breaches in Lowland Areas: A Methodology Based on Numerical Modelling." Natural Hazards and Earth System Sciences, vol. 20, no. 1, pp. 59-72. doi: http://dx.doi.org.ezproxy.cyclib.nocccd.edu/10.5194/nhess-20-59-2020.
[19] Chang, I., Lee, M., and Cho, G., 2019, "Global CO_2 Emission-Related Geotechnical Engineering Hazards and the Mission for Sustainable Geotechnical Engineering." Energies, vol. 12 (13), pp.

2567. doi: http://dx.doi.org.ezproxy.cyclib.nocccd.edu/10.3390/en12132567.
[20] Ward, P, Blauhut, V., Bloemendaal, N., Daniell, J., de Ruiter, M., Duncan, M., Emberson, R., Jenkins, S., Kirschbaum, D., Kunz, M., Mohr, S., Muis, S., Riddell, G., Schafer, A., Stanley, T., Veldkamp, T., and Winsemius, H., 2020, "Review Article: Natural Hazard Risk Assessments at the Global Scale." Natural Hazards and Earth System Sciences, vol. 20, (4), pp. 1069-1096.
[21] United State Geological Survey, 2016, "Latest Earthquakes", Retrieved Jan. 31, 2019, from https://earthquake.usgs.gov/earthquakes/map.
[22] Miller, E., and Roycroft, G., 2004, "Seismic Performance and Deformation of Levees: Four Case Studies." Journal of Geotechnical and Geoenvironmental Engineering, vol. 130 (4). Doi: https://doi.org/10.1061/(ASCE)1090-0241(2004)130:4(344).
[23] US Army Corps of Engineers (USACE), 2014, "Santa Ana River 1 Levee System Final Periodic Inspection Report", (1).
[24] Hazards Vulnerability Research Institute. (2007). Hazards and Vulnerability Research Institute, University of South Carolina. Retrieved January 31, 2019, from https://artsandsciences.sc.edu/geog/hvri/hvri-resources.
[25] Melo, C., and Sharma, S., 2004, "Seismic Coefficient for Pseudostatic Slope Analysis.", 13th World Conference on Earthquake Engineering, paper number 369, Vancouver, B.C., Canada.
[26] Bandara, S., Ohtsuka, S. and Fukumoto, Y., 2018. "Identification of Shear Strength and Seismic Coefficient by Back Analyzing Surficial Slides in the 2004 Mid-Niigata Prefecture Earthquake" Landslides, vol. 15 (11), pp. 2255-2266. doi: http://dx.doi.org.ezproxy.cycli b.nocccd.edu/10.1007/s10346-018-1029-6.
[27] Yang, X., Zhai, E., Wang, Y., and Hu, Z., 2018, "A Comparative Study of Pseudo-Static Slope Stability Analysis Using Different Design Codes." Water Science and Engineering, vol. 11, (4), pp. 310-317.
[28] Christian, J. T., & Urzua, A., 2017, "Anomalies in Pseudostatic Seismic Stability Analysis." Journal of Geotechnical and Geoenvironmental Engineering, vol. 143 (5). https://doi.org/10.1061/(ASCE)GT.1943-5606.0001666

THE EFFECT OF WEATHERING ON THE APPROPRIATENESS OF GRANITE FOR CLAY STABILIZATION

PREDVIDEN VPLIV PREPEREVANJA NA PRIMERNOST GRANITA ZA STABILIZACIJO GLINE

Syed Husnain Ali Shah *(corresponding author)*
Hazara University,
Department of Earth and Environmental Sciences
Mansehra, Pakistan
E-mail: shas.husnain@gmail.com, syedhusnain@hu.edu.pk

Mohammad Arif
Peshawar University,
Department of Geology
Peshawar, Pakistan

Mohammad Amjad Sabir
COMSATS University Islamabad,
Department of Earth Sciences
Abbottabad, Pakistan

Javed Iqbal Tanoli
COMSATS University Islamabad,
Department of Earth Sciences
Abbottabad, Pakistan

Asma Saleem
Hazara University,
Department of Earth and Environmental Sciences
Mansehra, Pakistan

Huzafa Tahir Lodhi
RWTH Aachen University,
Division of Earth Sciences and Geography
Aachen, Germany

DOI https://doi.org/10.18690/actageotechslov.19.1.48-55.2022

Keywords

soil stabilization, granite, weathering, settlement, bearing capacity

Ključne besede

stabilizacija tal, granit, preperevanje, posedek, nosilnost

Abstract

This study analyzes the impact of weathering on the effectiveness of granite as a stabilization agent for clay soils. A sample of clay soil was obtained from Mansehra District (Hazara, Pakistan) and its composition was determined. The sample consists of quartz, feldspare, kaolinite and illite, and is categorized as a CH soil following the Unified Classification System. Samples of fresh (non-weathered) and variously altered, i.e., slightly weathered, moderately weathered and highly weathered Mansehra granite were collected. Two different amounts (12.5 % and 25 %) of these granite varieties were mixed with the clay soil sample and geotechnical properties (plasticity index, activity, cohesion, angle of internal friction, maximum dry density, optimum moisture content, unconfined compressive strength and allowable bearing capacity) of the resulting mixtures were determined following the corresponding standard ASTM procedures. The results reveal that the addition of all the granite types, except the highly weathered variety, leads to an improvement in the parameters

Izvleček

Predstavljena študija obravnava možen vpliv preperevanja na učinkovitost granita kot stabilizatorja za glinene zemljine. Iz okrožja Mansehra (Hazara, Pakistan) smo pridobili vzorec glinene zemljine in določili njeno sestavo. Vzorec je sestavljen iz kremena, ortoklaza, kaolinita in ilita in je po enotnem klasifikacijskem sistemu kategoriziran kot CH zemljina. Pripravljeni so bili vzorci svežega (nepreperelega) in različno spremenjenega, torej rahlo preperelega, mešanice rahlo in zmerno preperelega, zmerno preperelega in močno preperelega granita Mansehra. Dve različni količini (12,5 % in 25 %) omenjenih variant granita sta bili pomešani z vzorcem glinene zemljine in določene geotehnične lastnosti (indeks plastičnosti, aktivnost, kohezija, kot notranjega trenja, največja suha gostota, optimalna vlažnost, enoosna tlačna trdnost in nosilnost) nastalih zmesi po ustreznih standardnih ASTM postopkih. Rezultati kažejo, da dodajanje vseh vrst granita, razen zelo preperele variante, vodi do izboljšanja omenjenih parametrov *of the soil. However, the magnitude of the positive impact produced, strongly depends on the degree of weathering of the added granite, i.e., the improvement in the soil properties decreases with the increasing degree of weathering of the added granite. This is because the weathering of granite principally involves the conversion of feldspars into clay minerals. As the weathering progresses, the abundance of clay minerals increases, while that of feldspars decreases. As a result, the water-absorption capacity of the granite increases and its specific gravity decreases. Hence, the higher the degree of granite weathering, the greater the abundance of clay minerals, the lower the specific gravity and the higher the water-absorption capacity, and thus the smaller the potential for the added granite to improve the properties of the soil.*

zemljine. Vendar pa je veličina pozitivnega vpliva močno odvisna od stopnje preperevanja dodanega granita, tj. lastnosti zemljine se zmanjšujejo z naraščajočo stopnjo preperevanja dodanega granita. To je zato, ker preperevanje granita v glavnem vključuje pretvorbo ortoklaza v minerale gline. Ko preperevanje napreduje, se številčnost glinenih mineralov poveča, medtem ko se za ortoklaz zmanjša. Posledično se poveča sposobnost vpijanja vode granita in zmanjša njegova specifična gravitacija. Zato je pri višji stopnji preperelosti granita, večja številčnost glinenih mineralov, nižja specifična gravitacija in večja vpojnost vode ter s tem manjši potencial dodanega granita za izboljšanje lastnosti zemljine.

1 INTRODUCTION

Only a few soil types are suitable in their natural or raw form for use in the construction of infrastructures, whereas most others (the so-called problematic soils) are not appropriate for this purpose [1]. The problematic soils typically contain natural clayey materials, which are considered detrimental to a construction because of their expansive nature [2]. The use of such soils is considered risky in the construction industry since they are susceptible to differential settlement and a volume change resulting from their greater compressibility and/or swelling [2]. In order to overcome this problem and reduce the risk of settlement while building infrastructures, clayey soils are subjected to the process of stabilization, i.e., blending and mixing with artificially made materials to bring an improvement in the soil's geotechnical properties so that it can acquire greater stability [3].

To reduce the soil's deformability, attempts to bring an improvement in the natural soil's properties with artificially prepared materials have been made for the past several years. Generally, the effects of lime, cement, mud, oil shale, fly ash and industrial solid waste on problematic raw soil have been examined experimentally and the results reveal that their addition improves the soil's properties at momentous levels. [4-9]. In addition to these additives, granite powder is widely used these days for soil stabilization owing to its good petrographic and rational engineering properties. Results from recent studies conducted by Sivrikaya et al. [1] and Ogbonnaya [10] show that the addition of granite reduces the plasticity index, the optimum moisture content and cohesion, and increases the strength parameters of the soil. An increasingly important issue regarding granite, and for that matter also other rocks, is its vulnerability to chemical weathering, which loosens its structure and causes a reduction in the strength parameters [11], which may in turn affect its aptness for soil stabilization. The studies conducted by Brand, 1990 [12]; GSE-GWPR, 1990 [13]; Cascini et al., 1992 [14], and Borrelli, 2004 [15] show that as the weathering degree of granite increases, its strength is reduced because there are more clay contents. Hence, it is imperative to properly study the impact of weathering, if any, on a given rock before it is used as an admixture for soil stabilization. This study focuses on assessing the degree of weathering of granite and the impact on its soil-stabilization potential.

2 MATERIALS AND METHODS

The soil sample for this study was picked from Mansehra District, KPK Pakistan (Figure 1). The sample was extracted from a 1-m-deep and 1.2-m-wide test pit. Based on the results from the grain size and hydrometer analyses (ASTM C136 [16] and ASTM D7928 [17] 90 % of the soil material is finer than 0.075 microns (Figure 2) and consists of 55 % silt and 35 % clay-size particles. The other geotechnical properties (Table 1) group the original soil with CH type (Figure 3). XRD analysis was performed to determine the mineralogical composition of the soil (Table 1). Based on the degree of weathering, non-weathered (NW), slightly weathered (SW), moderately weathered (MW) and highly weathered (HW) samples of granite were collected from different parts of the study area (Figure 1) for use as an admixture to assess their potential as a soil-stabilizing agent. The degree of weathering of the collected granite samples was determined by applying the relevant published criteria [12-15]. The NW Mansehra granite is made

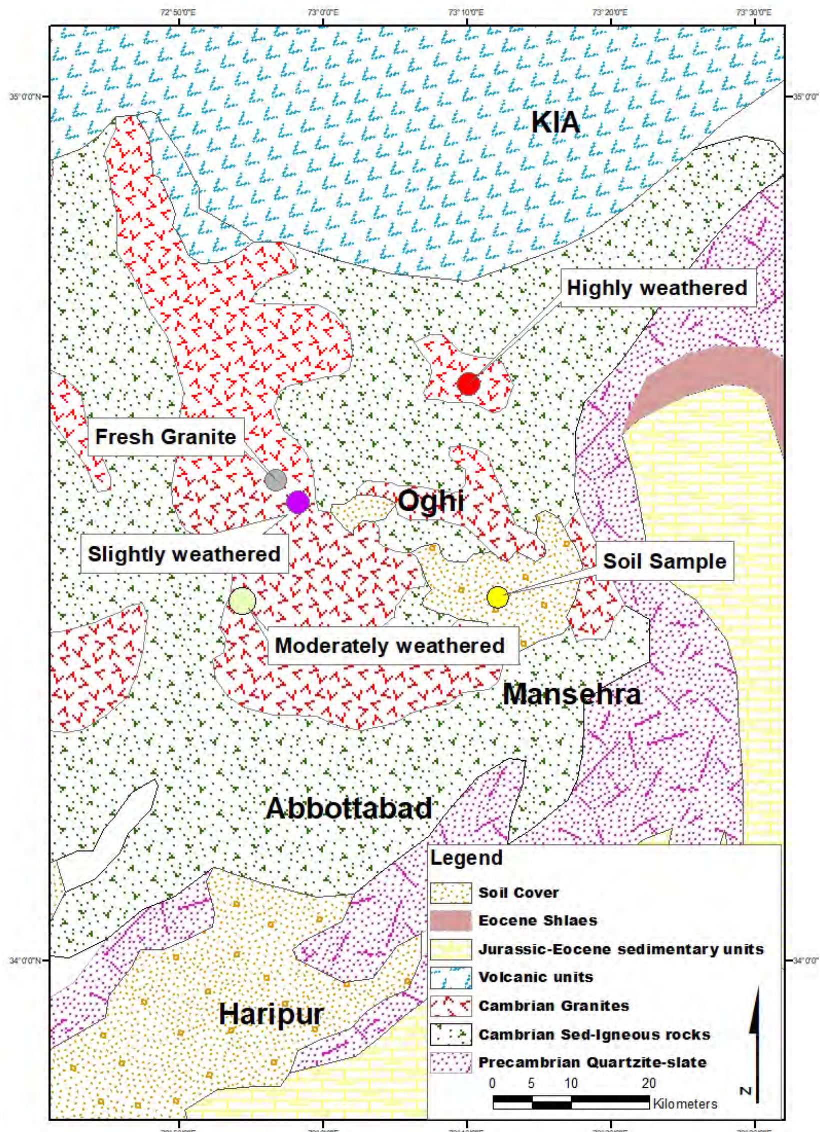

Figure 1. Geological map (Shams, 1967) showing the location of the rocks and soil samples used for the soil stabilization. [26].

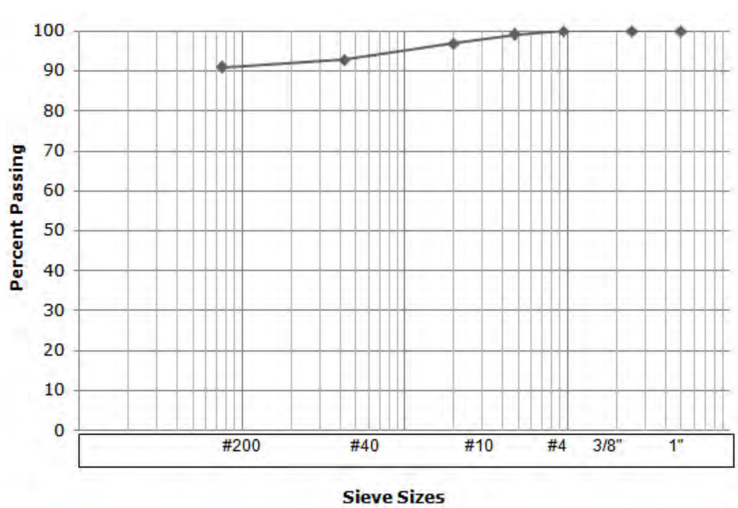

Figure 2. Grain size distribution of the investigated soil sample.

Table 1. Geotechnical properties and mineralogical composition of the untreated soil sample.

Specific Gravity	2.65
Maximum Dry Density (kN/m^3)	16.56
Optimum Moisture content (%)	19
Liquid Limit (%)	45
Plastic Limit (%)	17
Plasticity Index (%)	28
Activity	0.8
Cohesion(kPa)	11.6
UCS (kPa)	35.1
Quartz (%)	51
Feldspar (%)	10
Kaolinite (%)	31
Illite (%)	8
Angle of internal friction	8
Soil type	CH

up of quartz (30 %), alkali feldspar (30 %), plagioclase feldspar (20 %) and mica (15 %), and has a very low water-absorption capacity (0.381 %) [18]. The values of the specific gravity and the water absorption of all the collected sample types were determined in accordance with the ASTM D6473 [19] method (Table 2). Each of the granite samples was crushed and ground, and the resulting powder passed through a 40# sieve opening. Eight sample mixtures were prepared by adding 12.5 % and 25 % of each of the four categories of granite powder to the original (untreated) soil sample, and an additional sample was prepared in which a mixture of slightly and moderately weathered granite powder is added to the soil. The original soil and all the nine mixtures were subjected to testing to determine their physical properties and strength following the corresponding ASTM standards (Table 3) [20-23]. The properties and parameters determined include plasticity index (PI), activity, maximum dry density (MDD), optimum moisture content (OMC), cohesion, angle of

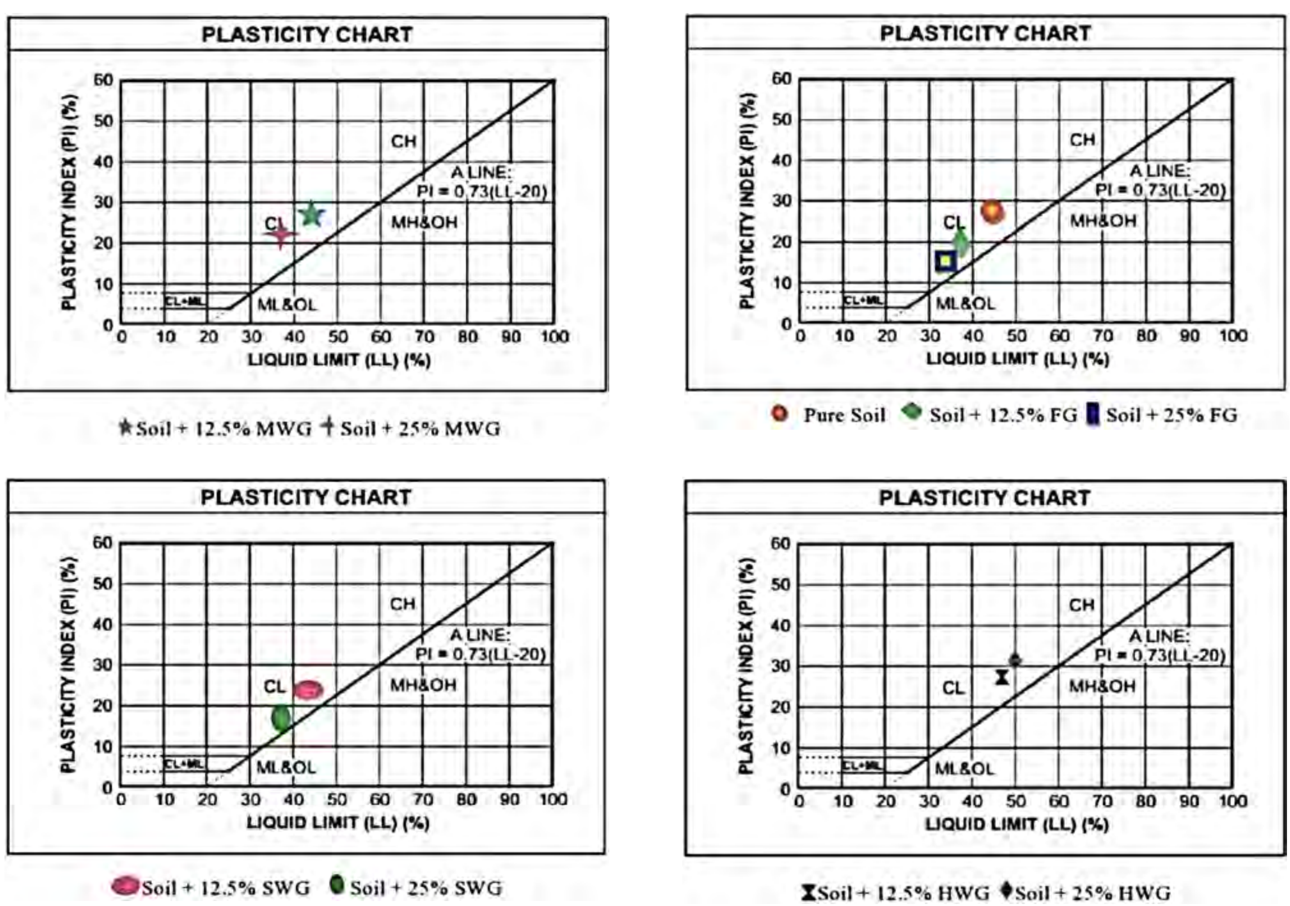

Figure 3. Unified classification of the untreated and variously treated soil samples.

Table 2. Specific gravity and water-absorption capacity of the different granites.

Samples	Type of Granite Admixture	Specific Gravity	Water absorption (%)
1	Fresh Granite	2.75	0.81
2	Slightly weathered	2.73	2.09
3	Moderately weathered	2.70	7.59
4	Highly weathered	2.63	16.28

Table 3. Tests conducted and the corresponding ASTM standard used and property determined.

Test Type	ASTM Standard	Determined Properties
Atterberg limits	D4318 [20]	Plasticity Index
Proctor compaction test	D698 [21]	MDD and OMC
Direct shear box test	D3080 [22]	Angle of Internal friction and Cohesion
Unconfined compressive strength test	D2166 [23]	Unconfined Compressive strength

internal friction, bearing capacity (BC) for various shallow foundations and unconfined compressive strength (UCS). The BC for various shallow foundations was calculated using the Terzaghi equations for strip footing, square footing and circular footing (Equation 1-3) [24], while the activity was determined with Equation 4 [25].

For strip footings:

$$Q_u = c\,N_c + \gamma\,D\,N_q + 0.5\,\gamma\,B\,N_\gamma \qquad (1)$$

For square footings:

$$Q_u = 1.3\,c\,N_c + \gamma\,D\,N_q + 0.4\,\gamma\,B\,N_\gamma \qquad (2)$$

For circular footings:

$$Q_u = 1.3\,c\,N_c + \gamma\,D\,N_q + 0.3\,\gamma\,B\,N_\gamma \qquad (3)$$

$$\text{Activity} = \text{plasticity index/clay content} \qquad (4)$$

where Q_u refers to the ultimate bearing capacity, C is the cohesion, γ is the dry density of the soil (the MDD value was used in this equation), D is the depth of the footing (the depth of test pit was used in this equation, from where the soil sample is extracted), B is the width of the footing (the width of the test pit was used in this equation, from where the soil sample is extracted), N_c, N_q, N_γ are the bearing-capacity factors and determined using Terzaghi's published chart (Figure 4).

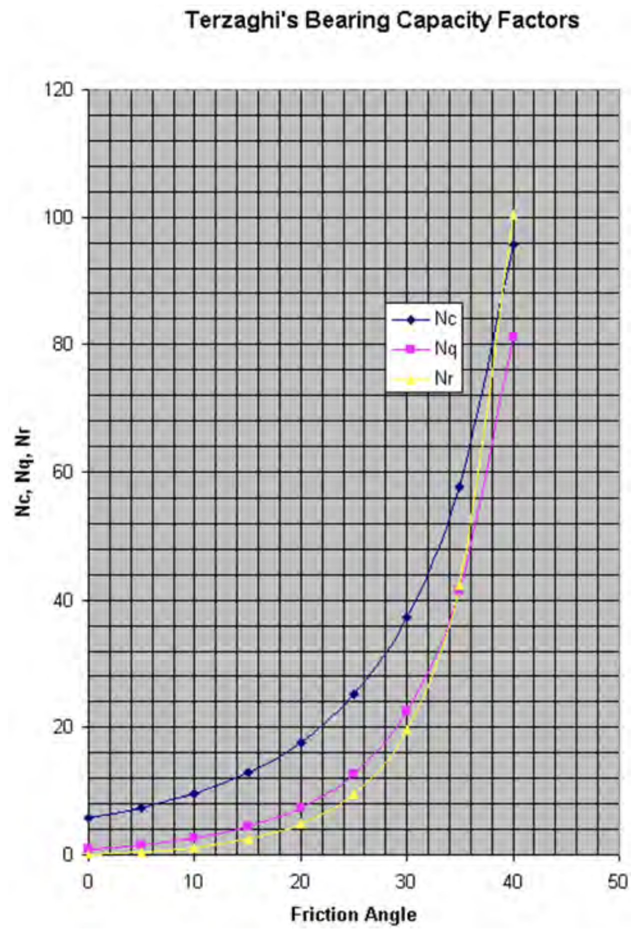

Figure 4. Determination of bearing capacity factors using the Terzaghi chart.

For an allowable bearing capacity, Q_u is divided by the factor of safety (FOS). The FOS used for this study is "3".

The values of the activity were determined, because these values are used as an index for identifying the swelling potential of clay soils. The higher the activity values, the greater the swelling potential.

3 RESULTS AND DISCUSSION

The Unified Classification System, which is based on the values of the liquid limit and the plasticity index, was used to characterize the investigated samples (Figure 3). The untreated soil sample belongs to the CH class (fat clays). The addition of NW, SW, MW and the mixture of SW+MW granites improves the soil by upgrading it to CL class; however, the addition of HW granite degrades rather than upgrades the soil. The studied soil sample has high values of PI, activity, cohesion and OMC

(Table 1). These values are directly proportional to the water-holding capacity of the soil, which is determined by its mineralogical composition, specifically the clay mineral content [27-29]. Unlike the NW granite, the original soil sample contains significant amounts of clay minerals, including kaolinite and illite (Tables 1). The addition of NW, SW, MW and the mixture of SW+MW granite powder led to a reduction in the values of PI, LL, activity, cohesion and OMC (Figure 5 and Figure 6). The main reason for this improvement is the abundance of non-clay minerals in granites (quartz, feldspars and mica) compared to raw soil. The addition of powder with non-active and less-absorptive minerals results in diluting the effect from more absorptive active clay minerals in the raw soil. The minerals contained in the added granite powder are predominantly stronger and hence their addition to the soil is likely to amplify the strength parameters including UCS, MDD, angle of internal friction and BC of various foundations of the latter(Figure 5 and Figure 6). Besides, the higher specific gravities of the added granites than the raw soil (Tables 1, 2) might be responsible for this significant positive change. The results demonstrate that as the degree of granite weathering increases, the effects of its powder addition on the soil properties diminish. That is why the effect of NW granite powder is the highest, while that of MW granite is the least and the HW type has even produced a negative impact by increasing PI, LL, OMC, activity (Figure 5), and reducing the strength parameters (Figure 6). This might be a consequence of the conversion of feldspars and mica into clay minerals due to the leaching of Na^+ and K^+ ions during the process of weathering. Wang et al. [30] produced a sketched section of a granite-weathering profile and demonstrated how weathering leads to the transformation of feldspars and micas into kaolinite and illite. The decrease in specific gravity and the rise in water-absorption capacity with an increasing degree of weathering validates the conversion of feldspar into kaolinite and illite in granites used in the current study. The presence of abundant quartz and alkali feldspar and the total absence of clay minerals are responsible for the observed high specific gravity of the fresh variety of granite. The increasing degree of weathering promotes the formation of kaolinite and illite at the expense of the granite feldspars and micas. As the clay minerals are lighter and have a higher water-absorption capacity than feldspars and micas, the progression in weathering results in a gradual decrease of the specific gravity and an increase in the water-absorption capacity from NW through SW and MW to HW varieties of the studied granite (Table 2). Consequently, the HWG has the least specific gravity and the greatest water-absorption capacity, and hence it is not suitable for soil stabilization, while the NWG is the most suitable for stabilization owing to it having the largest specific gravity and least water-absorption capacity. The effect of slightly and moderately weathered granites and their mixtures on the soil's properties can be improved more by adding lime. This is because the mixing of lime with materials having clay contents can cause the migration of calcium ions (Ca_2^+) from the lime to the clay particle surfaces and displace other ions and water [31]. This process makes the material friable and granular by reducing its moisture, PI and increasing the strength [31-34].

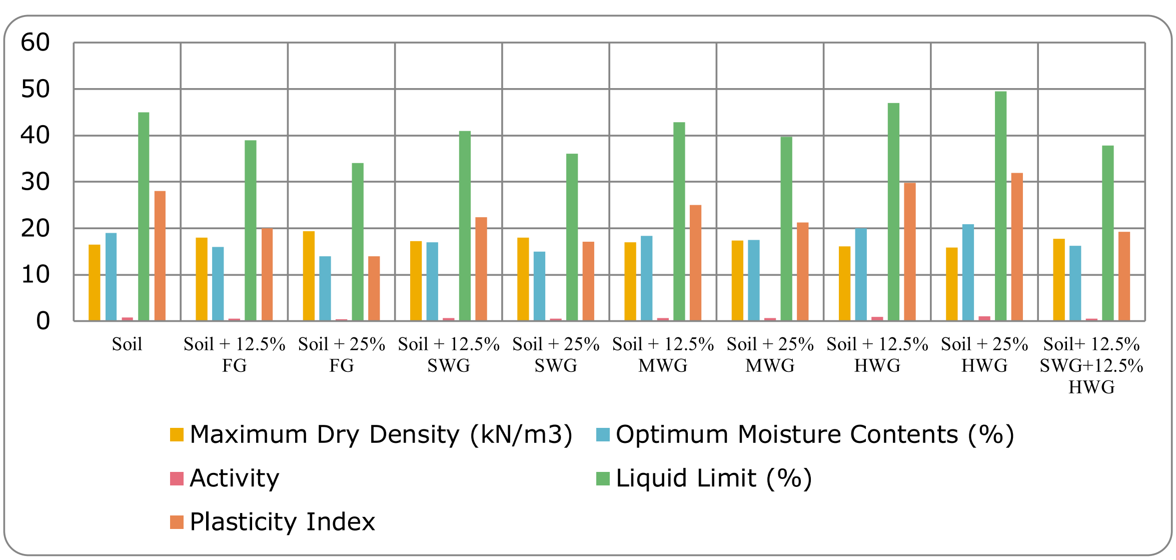

Figure 5. Variation in MDD, OMC, PI, LL and activity of soil containing different proportions of the four types of granite powders (FG= fresh granite, SWG=slightly weathered granite, MWG= moderately weathered granite, HWG=highly weathered granite).

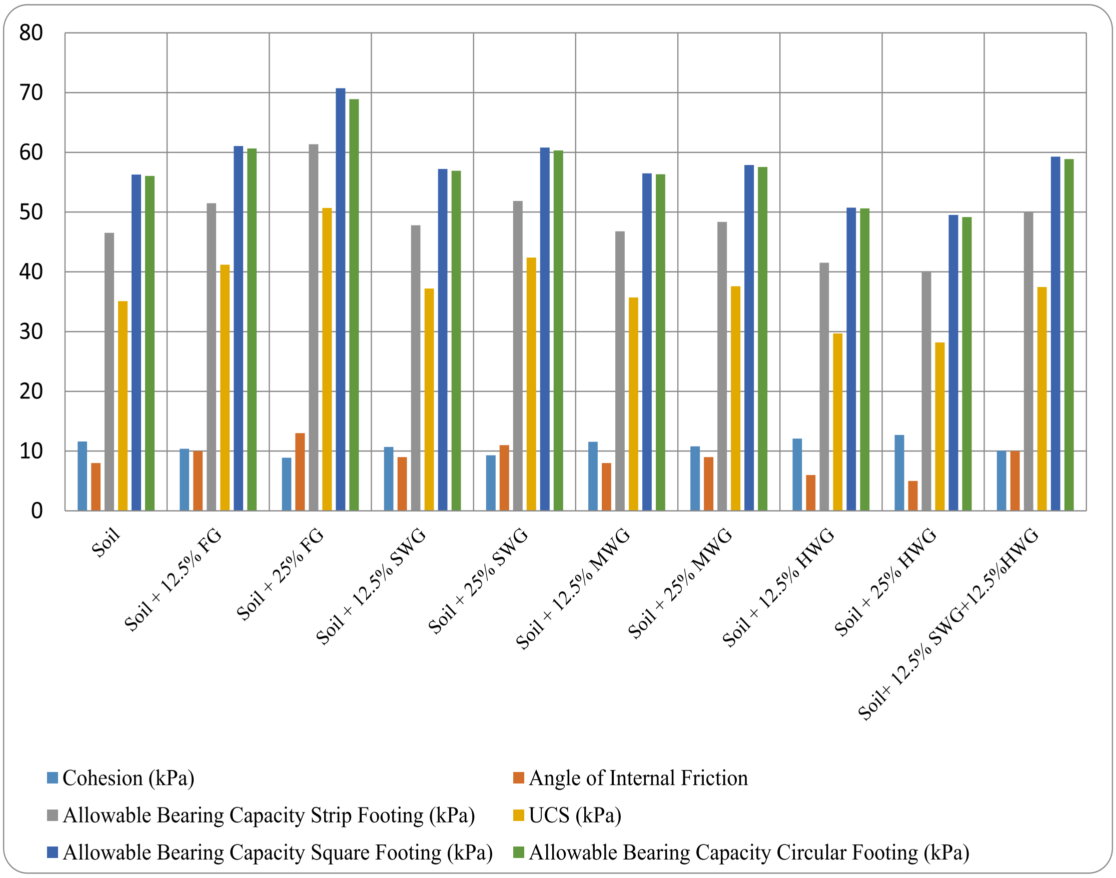

Figure 6. Variation in cohesion, angle of internal friction, UCS and allowable BC for shallow foundations of soil mixed with different amounts of four types of granite powders (FG= fresh granite, SWG=slightly weathered granite, MWG= moderately weathered granite, HWG=highly weathered granite).

4 CONCLUSIONS

The following conclusions can be drawn from the present study:

1. The addition of fresh (non-weathered granite), slightly weathered granite, a mixture of slightly and moderately weathered granite, and moderately weathered granite as an admixture produces a variable but positive effect on the geotechnical properties of problematic soils.
2. The fresh granite (non-weathered granite) admixture produces the most positive impact on the soil's properties, followed by slightly weathered granite, a mixture of slightly and moderately weathered granite, and moderately weathered granite.
3. The addition of highly weathered granite adversely affects the soil's properties by increasing its plasticity index, activity, liquid limit and optimum moisture content and reducing the maximum dry density, the angle of internal friction, the unconfined compressive strength and the bearing capacity for various shallow foundations.

REFERENCES

[1] Sivrikaya O, Koray R, Karaca, Zeki K (2014) Recycling waste from natural stone processing plants to stabilise clayey soil. Environmental Earth Sciences: 71. 4397-4407. 10.1007/s12665-013-2833-x.
[2] Malcolm S (2000) Expansive Soils and the Geomembrane Remedy. Advances in Unsaturated Geotechnics: 456-466. 10.1061/40510(287)31.
[3] Olufowobi J, Ogundoju A, Michael B, Aderinlewo O (2014) Clay soil stabilisation using powdered glass. Journal of Engineering Science and Technology: 9, 541-558.
[4] Turner JP (1994) Soil stabilization using oil-shale solid waste. Journal of Geotechnical Engineering: 120, 4, 646-660.
[5] Attom MF, Al-Sharif MM (1998) Soil stabilization with burned olive waste. Applied Clay Science: 13, 219-230.
[6] Bahar R, Benazzoug M, Kenai S (2004) Performance of compacted cement-stabilized soil. Cement Concrete Composite: 26, 811-820.
[7] Huat BBK, Maail S, Mohammad TA (2005) Effect

of chemical admixtures on the engineering properties of tropical Peat soil. American Journal of Applied Science: 2, 7, 1113-1120.
[8] Eroglu H, Acar HH, Osman U, Sami I (2006) Soil stabilization of forest roads sub-base using lime mud waste from the chemical recovery process in alkaline mill. Journal of Applied Science: 6, 5, 1199-1203.
[9] Reyes A & Pando M (2007) Evaluation of CFBC fly ash for improvement of soft clays. World of Coal Ash (WOCA), Covington, Kentucky, USA: 7-10.
[10] Ogbonnaya I, Illoabachie DE (2011) The potential effect of granite dust on the geotechnical properties of Abakalili clays. Continental J. Earth Sciences: 6, 1, 23–30
[11] Goel RK., Mitra S (2015) Importance of weathering in rock engineering. Conference: Int Golden Jubilee Conf Engineering Geology in New Millennium EGNM.
[12] Brand EW (1990) Written discussion: evolution of a classification scheme for weathered rock. Proc. 2nd Intern. Conf. on Geomechanics in Tropical Soils. Singapore: 515–518.
[13] GSE-GWPR (1990) Tropical residual soils. Quarterly Journal of Engineering Geology: 23, 1–101.
[14] Cascini L, Critelli S, Di Nocera S, Gullà G, Matano F (1992) Grado di alterazione e franositànegli gneiss del Massicciosilano:l'area di S.Pietro in Guarano (CS). Geologia Applicata e Idrogeologia: 27, 49–76.
[15] Borrelli L, Greco R, Gullà G (2007) Weathering grade of rock masses as a predisposing factor to slope instabilities: Reconnaissance and control procedures. Geomorphology: 87, 158-175. 10.1016/j.geomorph.2006.03.031.
[16] ASTM C136 / C136M (2019) Standard Test Method for Sieve Analysis of Fine and Coarse Aggregates. ASTM International, West Conshohocken, PA.
[17] ASTM D7928 (2017) Standard Test Method for Particle-Size Distribution (Gradation) of Fine-Grained Soils Using the Sedimentation (Hydrometer) Analysis. ASTM International, West Conshohocken, PA.
[18] Arif M, Mulk A, Mehmood TM, Shah HM (1999) Petrography and mechanical properties of mansehra granite, Hazara, Pakistan. Geol. Bull. Univ. Peshawar: 32, 41-49.
[19] ASTM D6473 (2015) Standard Test Method for Specific Gravity and Absorption of Rock For Erosion Control. ASTM International, West Conshohocken, PA.
[20] ASTM D4318 (2000) Standard test methods for liquid limit, plastic limit and plasticity index of soils. ASTM International, West Conshohocken, PA, USA.
[21] ASTM D698 (2000) Standard test method for laboratory compaction characteristics of soil using standard effort. West Conshohocken, PA, USA: ASTM International.
[22] ASTM D3080 / D3080M (2011) Standard Test Method for Direct Shear Test of Soils under Consolidated Drained Conditions. ASTM International, West Conshohocken, PA.
[23] ASTM D2166 (2006) Standard Test Method for Unconfined Compressive Strength of Cohesive Soil. ASTM International, West Conshohocken, PA.
[24] Terzaghi K. Theoretical Soil Mechanics. Wiley, New York, USA.
[25] Skempton AW (1948) A possible relationship between true cohesion and the mineralogy of clays. Proc. 2nd Int. Conf. S.M: 7, 45.
[26] Shams FA (1967) Granites of the Mansehra-Amb state area and the associated metamorphic rocks. Unpubl Ph. D thesis, Univ. Punjab, Lahore.
[27] Gardner WR (1971) Laboratory measurement of available soil water. Soil Sci. Soc. Am. Froc: 35, 852.
[28] Moorman FR & Van Wambeke A (1978) The soils of the low land rainy tropical climates. Their inherent limitations for food production and related climatic restraints. Proc. II Congr. Soil Sci. Soc: 2,165-197.
[29] Hillel D (1980) Fundamentals of soil physics. Academic Press, New York.
[30] Wang Z, Ma J, Li J, Wei G, Zeng T, Li, L, Zhang L, Deng W, Xie, L, Liu Z (2018) Fe (hydro) oxide controls Mo isotope fractionation during the weathering of granite. Geochimica et Cosmo chimica Acta: 226.
[31] Firoozi AA, Olgun CG, Firoozi AA & Baghini MS (2017) Fundamentals of soil stabilization. Int. J. GeoEng: 8–26. DOI: 10.1186/s40703-017-0064-9
[32] Shah SHA, Arif M, Sabir MA, Iqbal J (2020) In-situ stabilization of clays with lime, dolerite and quartzite powders. Acta Geodynamica et Geomaterialia: 17, 3(199), 341–352. DOI: 10.13168/AGG.2020.0025.
[33] Shah SHA, Arif M, Sabir MA, Rehman Q (2020) Impact of Igneous rocks admixtures on geotechnical properties of Lime stabilized clays. Civil and Environmental Engineering: 16, 2, 329-339.
[34]. Shah SHA, Arif M, Rehman Q, Manzoor F (2021). Utilization of dolerite waste powder for improving geotechnical parameters of compacted clay soil Open Geosciences, 13(1), 1523–1535.

STRENGTH AND FREEZE-THAWING PROPERTIES OF WHEAT-STRAW-ADDED CLAY

TRDNOST IN LASTNOSTI ZAMRZOVANJA IN ODMRZOVANJA GLINE Z DODANO PŠENIČNO SLAMO

Bahattin Ozdemir
Investment Monitoring and Coordination Department
25040 Erzurum, Turkey
E-mail: bozdemir1015@gmail.com

Zeynep Nese Kurt Albayrak *(corresponding author)*
Ataturk University,
Department of Civil Engineering
25240 Erzurum, Turkey
E-mail: znkurt@atauni.edu.tr

DOI https://doi.org/10.18690/actageotechslov.19.1.56-62.2022

Keywords

clay, freezing-thawing, geotechnical, soil stabilization, unconfined compressive strength, wheat straw

Ključne besede

glina, zamrzovanje-odmrzovanje, geotehnika, stabilizacija tal, enoosna tlačna trdnost, pšenična slama

Abstract

Different methods are used to improve the geotechnical properties of clay soils. One of these methods is the improvement of the properties of soil such as swelling, settlement, permeability and strength by adding various additives to clay soil. The additives included in the clay for the improvement can be waste materials such as silica fume, fly ash or red mud, as well as cement, lime or chemicals. In addition, natural or synthetic fibers are also used to improve the engineering characteristics of clays. In this study, the consistency, compaction, unconfined compression and freezing-thawing properties of wheat-straw-added-clay samples obtained by adding wheat straw to a clay in different percentages (0.5 %, 1 %, 1.5 %) and with different lengths (2 mm, 5 mm) were investigated. The tests showed that the unconfined compressive strength of the clay increased with an increase in the percentage of straw. Unconfined compression tests performed after the samples were subjected to four cycles of freezing-thawing tests revealed that the straw had a positive effect on the unconfined compression strength of the clay after freezing-thawing. The overall evaluation of the test results revealed that wheat-straw fiber can be used as an additive for the stabilization of high-plasticity clays.

Izvleček

Za izboljšanje geotehničnih lastnosti glinenih tal se uporabljajo različne metode. Ena od teh metod za izboljšanje lastnosti tal, kot so nabrekanje, posedanje, prepustnost in trdnost je z dodajanjem različnih dodatkov v glineno zemljino. Dodatki za izboljšanje gline, so lahko odpadni materiali, kot so silicijev dioksid, pepel ali rdeče blato, pa tudi cement, apno ali kemični dodatki. Poleg tega se za izboljšanje inženirskih lastnosti gline uporabljajo tudi naravna ali sintetična vlakna. V tej študiji so bile raziskane lastnosti konsistence, zbijanja, enoosne tlačne trdnosti ter zamrzovanja in odmrzovanja vzorcev gline z dodano pšenično slamo, v različnih odstotnih deležih (0,5 %, 1 %, 1,5 %) in različnih dolžinah (2 mm, 5 mm). Opravljeni preizkusi enoosne tlačne trdnosti gline so pokazali, da se le ta povečuje z večanjem vsebnosti slame. Enoosni tlačni preskusi, opravljeni po tem, ko so bili vzorci podvrženi 4 ciklom preskusa zamrzovanja-odmrzovanja, so pokazali, da je slama pozitivno vplivala na enoosno tlačno trdnost gline po zamrzovanju-odmrzovanju. Celotna ocena rezultatov preizkusa je pokazala, da se vlakna iz pšenične slame lahko uporabljajo kot dodatek pri stabilizaciji gline z visoko plastičnostjo.

1 INTRODUCTION

People have been using soils as foundation materials or building materials since ancient times. Clayey soils with a grain size of less than 2 microns are formed by the chemical decomposition of rocks [1]. Clays are used in geotechnical engineering, in the foundation of solid-waste storage areas, in landfill applications and dams to form an impermeable layer in a clay-core formation. Clays are soils that exhibit plasticity when wet, that swell when water is absorbed into their structures and exhibit shrinkage characteristics when they lose water. These behaviors of clays create deformation problems in the soil [2]. Additionally, the soils, especially in cold climatic regions, can be exposed to freezing-thawing cycles and the engineering properties of soils can be affected by this freezing-thawing [3,4]. Various methods of soil improvement have been developed to reduce or to prevent the effects of swelling, settlement, shrinkage, etc. deformations that can occur in clays or to remove the negative properties of clay soils and improve their engineering properties [5]. One of these soil-improvement methods is adding additives to clay soils. Some of these additives can be listed as cement, lime, fly ash, glass powder, marble powder, silica fume and natural/synthetic fibers [6-10].

Natural fibers are low-cost, low-density and high-characteristic fibers [11]. Some natural fibers are coir fiber, sisal, palm, jute, flax, bamboo, cane, barely straw and cotton straw [12,13]. Sera et al. [14] stated that the ductility and strength of brittle materials can be improved with natural fiber additives and natural fiber-clay mixtures can be used in grain-storage silos for isolation and strength. Zaimoğlu et al. [15] added randomly distributed waste chicken quill as a natural fiber into high-plasticity clay soil and found that the freezing-thawing behavior of the clay soil was improved. Sharma et al. [16] investigated the stabilization of two local natural fibers and clay soil to improve the compressive-strength properties of adobe, which is widely used in rural houses, and they found that natural fibers increase the compressive strength of clay soil. Estabragh et al. [17] added palm-tree fiber to a low-plasticity clay and stated that the fiber additive significantly improved the engineering behavior of the soil. Anggraini et al. [18] found that the unconfined compressive strength of coconut-fiber-added clays is higher than that of clay. Prabakar and Sridhar [19] revealed that sisal fiber increases the shear strength of clay. Ma et al. [20] reinforced a clay soil with flax fiber and stated that the shear strength of the clay was improved.

The aim of this study was to investigate the improvement of the geotechnical properties of clay soils with the addition of wheat straw as a natural fiber. In this study the effect of natural straw of different lengths (2 mm and 5 mm) and percentages (0.5 %, 1 % and 1.5 %) on the unconfined compressive strength and freezing-thawing of a high-plasticity clay was investigated.

2 MATERIALS AND METHODS

2.1 Clay

In this study clay from Turkey-Erzurum (C) was used. The clay taken to the laboratory was dried in the oven at 105° C for 24 hours. The dried clay samples were removed from the oven, grinded in a Los Angeles abrasion device and sieved in a No.40 sieve (Figure 1). Some geotechnical properties of the clay sample are shown in Table 1 and the results of the X-ray fluorescence (XRF) analysis are shown in Table 2. The mineral content of the clay was determined as quartz, plagioclase, clay mineral and calcite.

Table 1. Some geotechnical properties of the clay.

Geotechnical Properties	Clay
< 0.002 mm, %	42
Specific gravity	2.64
Liquid limit, %	60.8
Plastic limit, %	26.5
Plasticity index, %	34.3
Soil classification*, (USCS)	CH
Optimum moisture content, %	25.5
Maximum dry unit weight, kN/m^3	15

*Unified soil-classification system

Table 2. XRF analysis of the clay.

Geotechnical Properties	Clay
SiO_2	59.3
Al_2O_3	16.5
A.Za	8.50
Fe_2O_3	8.0
MgO	2.1
K_2O	1.6
CaO	1.5
Na_2O	1.4
TiO_2	0.6
P_2O_5	0.2
MnO	< 0.1

2.2 Wheat-straw fiber

In this study straw (S) derived from wheat being produced in the eastern Anatolia region of Turkey was used. Approximately the same thickness stems of wheat straw taken to the laboratory were selected, cut into 2-mm and 5-mm dimensions, and used in the experiments (Figure 1). The straw was dried in sunlight and stored in a jar to completely remove the water that can be found in it.

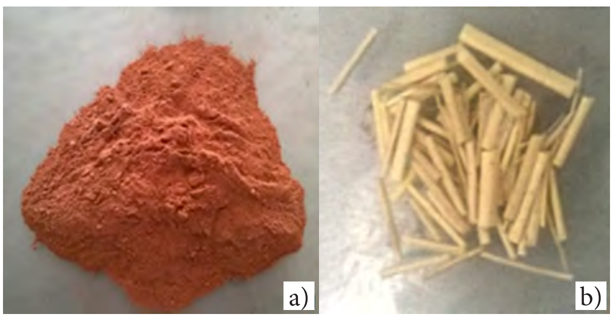

Figure 1. a) Clay sample b) Cut straw.

2.3 Sample Preparation

The clay sample, which was dried and grinded after being taken to the laboratory, was sieved in a No. 40 sieve. Straw fibers with lengths of 2 mm and 5 mm in weight ratios 0.5 %, 1 % and 1.5 % were added to the sieved clay sample. Clay and straw fibers were mixed homogeneously. Test samples and straw-additive percentages and lengths are given in Table 3.

Table 3. Samples.

Length	Straw fiber, %	
	2 mm	5 mm
C	-	-
S1	0.5	-
S2	1	-
S3	1.5	-
S4	-	0.5
S5	-	1
S6	-	1.5

2.4 Tests

Consistency-limit tests were carried out on samples with straw additives. The liquid limit is determined with the falling-cone method according to BS 1377, Part 2 (1990) and the plastic limit is determined according to ASTM D 4318. The optimum moisture content and maximum dry unit volume weights of the clay were determined by the standard proctor test according to ASTM D 698. Samples from the straw-added clays for unconfined compression and freezing-thawing tests are cylindrical samples with a diameter of 3.8 cm and a height of 7.6 cm. These samples are prepared by compacting with standard compaction energy using the optimum moisture content for the clay. An unconfined compression test was carried out according to ASTM D 2166. Likewise, the samples were subjected to a freezing-thawing test. For the freezing-thawing tests, the number of cycles is four [21], the temperatures are –20° C for freezing and +25° C for thawing [21,22], and the waiting time for each interval is 6 hours. The samples were wrapped in aluminum foil to avoid any loss of water. After freezing-thawing, unconfined compressive strengths were determined for the samples once the freezing-thawing cycles were completed.

3 RESULTS AND DISCUSSION

3.1 Consistency-Limit Test Results

The consistency-limit test results on the straw-added-clay samples are given in Table 4. The change in the liquid limit of the samples with the increase in the percentage of straw is presented in Figure 2.

Table 4. Consistency-limit test results.

Sample	Liquid limit, %	Plastic limit, %	Plasticity index, %
C	60.8	26.5	34.3
S1	66.8	35.0	31.8
S2	66.4	43.0	23.4
S3	68.5	40.5	28
S4	66.5	41.0	25.5
S5	64.0	40.5	23.5
S6	65.5	34.0	31.5

The liquid limit of the clay increased with the addition of straw (Figure 2). It was observed that the addition of 0.5 %, 1 % and 1.5 % straw in 2-mm lengths increased the liquid limit of the clay by 10 %, 9 % and 13 %, respectively. The addition of 0.5 %, 1 % and 1.5 % straw in 5-mm lengths, increased the liquid limit of the clay by 9 %, 5 % and 8 %, respectively. Figure 3 shows the soil classes of the 2-mm straw-added-clay samples and Figure 4 shows the soil classes of the 5-mm straw-added-clay samples. According to the unified soil-classification system

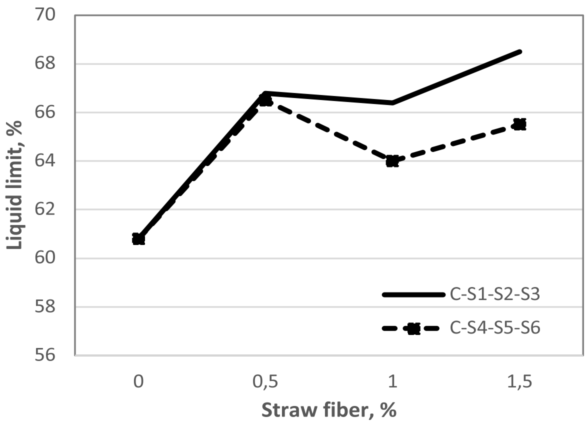

Figure 2. Change in liquid limits of straw-added-clay samples.

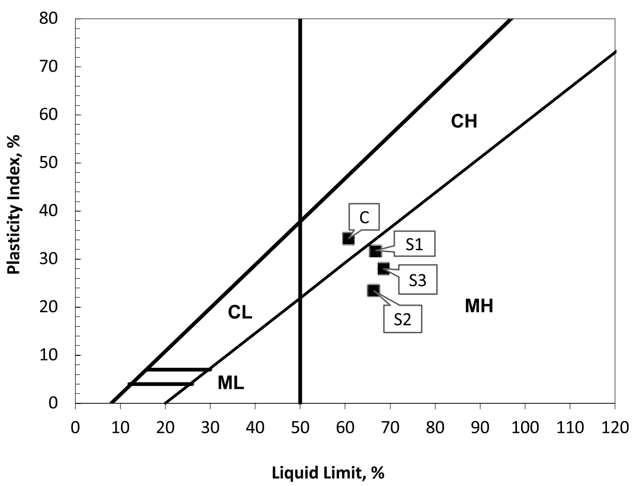

Figure 3. Casagrande plasticity chart of 2-mm straw-added-clay samples.

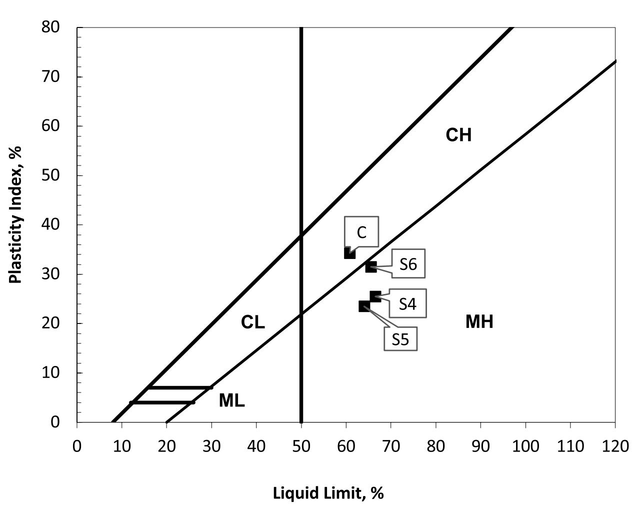

Figure 4. Casagrande plasticity chart of 5-mm straw-added-clay samples.

(USCS), the soil class of clay that was originally determined as high-plasticity clay (CH) showed a behavior of high-plasticity silt (MH) a soil class with 2-mm and 5-mm lengths of straw-additive effect and at different rates.

3.2 Unconfined Compressive-Strength Test Results

In Table 5 the unconfined compressive-strength values of the straw-added-clay samples are given. Figure 5 shows the change in the unconfined compressive-strength values of the straw-added-clay samples with an increase in the percentage of straw additive.

Table 5. Unconfined compressive-strength values of straw-added-clay samples.

Sample	Unconfined compressive strength, kPa
C	157
S1	248
S2	258
S3	327
S4	231
S5	233
S6	329

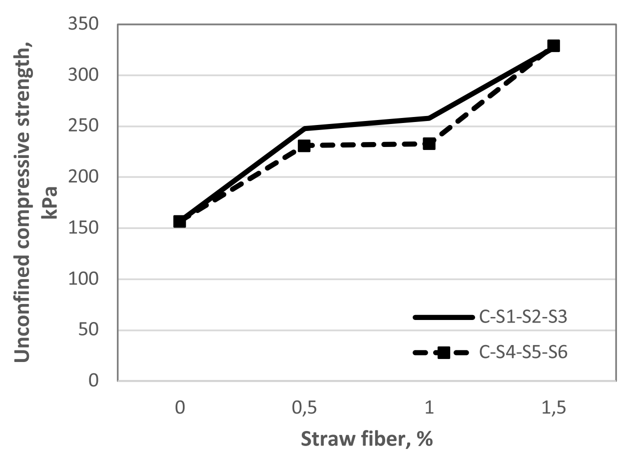

Figure 5. Change in unconfined compressive-strength values with increasing straw percentage.

The unconfined compressive strength of the samples increased with the increase in the percentage of straw, compared to clay. The unconfined compression strength of samples with 0.5 %, 1 % and 1.5 % straw additives of 2-mm length increased by 58 %, 64 % and 108 %, respectively, compared to the unconfined compressive strength of the clay. Unconfined compression strengths of the 0.5 %, 1 % and 1.5 % straw-added samples of 5-mm

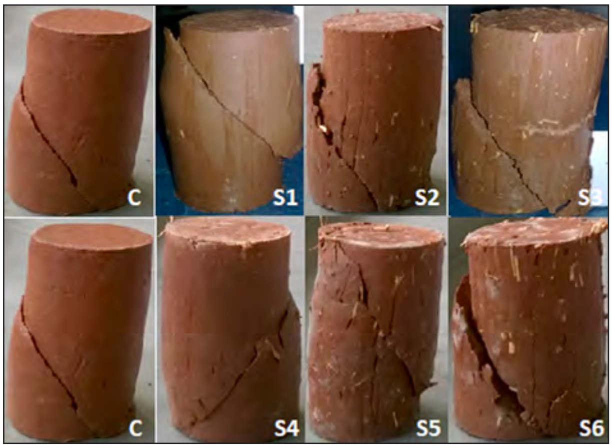

Figure 6. Fracture forms of samples after unconfined compression tests.

length increased by 47 %, 48 % and 110 %, respectively, compared to the unconfined compression strength of the clay. Figure 6 shows the fracture forms of the clay and straw-added-clay samples occurred after the unconfined compression tests.

Qu and Sun [23] added wheat-straw fiber to clay and examined the strength behavior and stated that the soil strength increased due to the frictional forces occurring between the fibers and the soil particles. Güllü and Khudir [24] stated that the jute fiber increased the unconfined compression strength of the clay and said that this could be because the jute fiber increased the tension in the soil. The amount of adhesion force and fiber shear strength between the fiber and the soil is linked to the contact surface area and the roughness of the fiber surface [25]. Given that the surface area of the high-plasticity clay is large, adhesion will be higher and therefore the unconfined compression strength can be increased accordingly.

3.3 Freezing-Thawing Test Results

In Table 6 the unconfined compression-strength values of straw-added-clay samples after four cycles of freezing-thawing are shown. When Table 6 is examined, it is seen that the highest unconfined compression-strength value after freezing-thawing was obtained from the sample (S6) with 2-mm length of 1.5 % straw additive. Figure 7 shows the change in unconfined compression strengths with an increase in the percentage of straw after four cycles of freezing-thawing of straw-added-clay samples.

According to Figure 7 the unconfined compression strengths determined after subjecting the straw-added-clay samples to four cycles of freezing-thawing increase with the increase in the percentage of straw. When the unconfined compression strength straw ratio of 2 mm and 5 mm straw-added clay after freezing-thawing was 1.5 %, it increased by 146 % and 140 %, respectively, compared to clay. Figure 8 shows the fracture forms that

Table 6. Unconfined compressive-strength values of straw-additive samples after four cycles of freezing-thawing.

Sample	Unconfined compressive strength after freezing-thawing, kPa
C	85
S1	124
S2	148
S3	209
S4	138
S5	161
S6	204

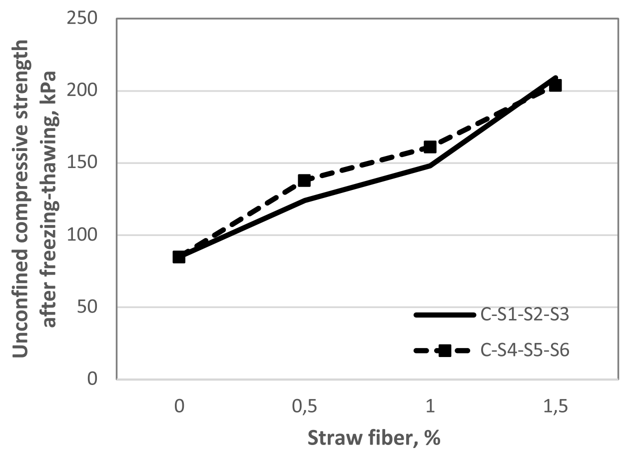

Figure 7. Change in unconfined compressive strengths of straw-added-clay samples after freezing-thawing.

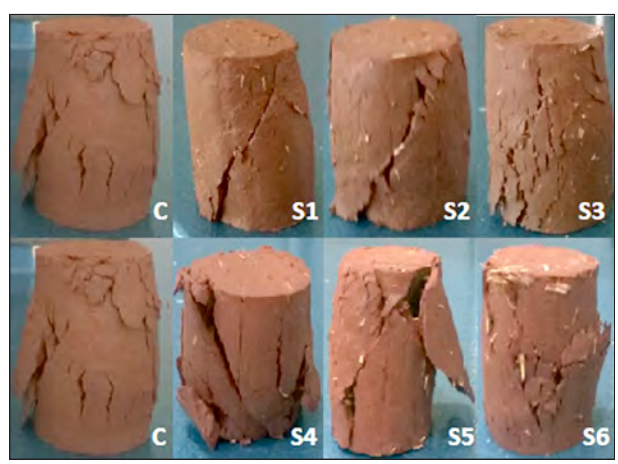

Figure 8. Fracture forms of samples that were exposed to freezing-thawing cycles.

occur after unconfined compression tests performed after four cycles of freezing-thawing in straw-added-clay samples.

The change in the unconfined compression strengths of the samples and the unconfined compression strengths after freezing-thawing are shown together in Figure 9. According to Figure 9, the loss of unconfined compressive strength in the samples after freezing-thawing was determined to be 46 % in clay. The decrease of the unconfined compression strength of the clay after freezing-thawing shows that the soil needs improvement in terms of freezing-thawing. The strength loss after freezing-thawing is 50 %, 43 % and 36 %, respectively, for 0.5 %, 1 % and 1.5 % additive ratios of straw additives with 2-mm length. For samples with 5-mm straw additives, the strength loss was determined as 40 %, 31 % and 38 % for the 0.5 %, 1% and 1.5 % additive ratios, respectively. It can be said that samples with straw additives are less affected by freezing-thawing cycles than the clay.

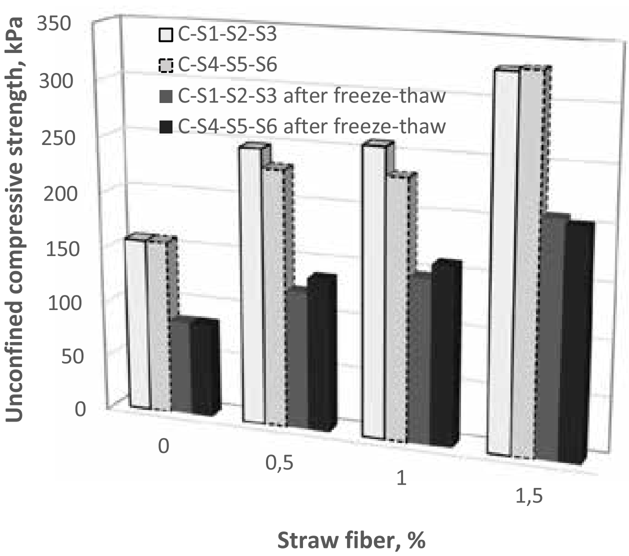

Figure 9. Unconfined compressive strength of samples and change in unconfined compressive strengths after freezing-thawing.

4 CONCLUSIONS

In this study the consistency, unconfined compression and freezing-thawing properties of straw-added-clay samples obtained by adding wheat straw in different percentages (0.5 %, 1 %, 1.5 %) and different lengths (2 mm, 5 mm) were investigated.

It was observed that the liquid-limit values of the straw-added-clay samples increased with the increase in the percentage of straw and the consistency properties of the samples changed. As a result of the consistency limits tests, the soil class of clay that was determined as CH according to USCS, changed to MH with the addition of straw.

As a result of unconfined compression tests on straw-additive samples, it was determined that unconfined compressive strengths increased with the increase in the percentage of straw in all of the straw-additive samples with a lengths of 2 mm and 5 mm. The unconfined compressive strength of the 2-mm-long straw-added clay increased by 108 % when compared to the clay when the straw ratio is 1.5 %. The unconfined compressive strength of clay with 5-mm straw additives increased by 110 % compared to clay when the straw ratio was 1.5 %.

Samples with straw additives were subjected to four cycles of freezing-thawing cycles. The unconfined compressive strengths of the straw-additive samples determined after freezing-thawing are higher than the unconfined compressive strength of the clay after freezing-thawing. The unconfined compressive strength of the straw-additive samples after freezing-thawing increased with the increase in straw percentage. The unconfined compressive strength of the 2-mm and 5-mm straw-added clay after freezing thawing increased by 146 % and 140 %, respectively, when the straw ratio was 1.5 % compared to clay.

Unconfined compression strength decreased after freezing-thawing with an increase in the straw length. Freezing-thawing reduced the unconfined compression strength of all the samples. Experimental studies have shown that the straw additive has a positive effect on the unconfined compressive strength after clay freezing. Straw-additive samples were less affected by freezing-thawing cycles than clay. It is thought that the use of straw additive will be appropriate as a soil-improvement method, especially in cold climatic regions, in order to minimize the soil being affected by freezing-thawing.

Fundings

This study did not receive financial support from public or private institutions and organizations.

REFERENCES

[1] Holtz, R.D. and Kovacs, W.D. 1981. An Introduction to Geotechnical Engineering. Prentice Hall Inc., New Jersey, USA.
[2] Mitchell, J.K., Soga, K. 2005. Fundamentals of Soil

Behavior. John Wiley&Sons, Inc., New Jersey.
[3] Zaimoglu, A. 2010. Freezing–thawing behavior of fine-grained soils reinforced with polypropylene fibers. Cold Regions Science and Technology 60(1), 63-65.
[4] Rezaei Fard, A., Moradi, G., Karimi Ghalehjough, B., Abbasnejad, A. 2020. Freezing-thawing resistance evaluation of sandy soil, improved by polyvinyl acetate and ethylene glycol monobutyl ether mixture. Geomechanics and Engineering 23(2), 179-187.
[5] Bell, F.G. 1993. Engineering Treatment of Soils. Chapman&Hall, London.
[6] Okagbue, C.O., Onyeobi, T.U.S. 1999. Potential of marble dust to stabilise red tropical soils for road construction. Engineering Geology 53(3-4), 371-380.
[7] Çokça, E. 2001. Use of class C fly ashes for the stabilization of an expansive soil. Journal of Geotechnical and Geoenvironmental Engineering 127(7), 568-573.
[8] Ayeldeen, M., Kitazume, M. 2017. Using fiber and liquid polymer to improve the behaviour of cement-stabilized soft clay. Geotextiles and Geomembranes 45(6), 592-602.
[9] Boz, A., Sezer, A. 2018. Influence of fiber type and content on freeze-thaw resistance of fiber reinforced lime stabilized clay. Cold Regions Science and Technology 151, 359-366.
[10] Oluwatuyi, O.E., Ojuri, O.O., Khoshghalb, A. 2020. Cement-lime stabilization of crude oil contaminated kaolin clay. Journal of Rock Mechanics and Geotechnical Engineering 12(1), 160-167.
[11] Saheb, D.N., Jog, J.P. 1999. Natural fiber polymer composites: A review. Advances in Polymer Technology 18(4), 351-363.
[12] Hejazi, S.M., Sheikhzadeh, M., Abtahi, S.M., Zadhoush, A. 2012. A simple review of soil reinforcement by using natural and synthetic fibers. Construction and Building Materials 30, 100-116.
[13] Yu, X., Liu, C., Lu, F. 2020. Field Test Study on Treatment of Dredged Soil with Cotton Straw. Soil Mechanics and Foundation Engineering 57, 343–350.
[14] Sera, E.E., Robles-Austriaco, L., Pama, R.P. 1990. Natural fibers as reinforcement. Journal of Ferrocement 20(2), 109-124.
[15] Zaimoğlu, A.Ş., Akbulut, R.K., Arasan, S. 2016. Effect of freeze-thaw cycles on strength behavior of compacted chicken quill clay composite in undrained loading. Journal of Natural Fibers 13(3), 299-308.
[16] Sharma, V., Vinayak, H.K., Marhava, B.K. 2015. Enhancing compressive strength of soil using natural fibers. Construction and Building Materials 93, 243-249.
[17] Estabragh, A.R., Bordbar, A.T., Javadi, A.A. 2013. A study on the mechanical behavior of a fiber-clay composite with natural fiber. Geotechnical and Geological Engineering 31, 501–510.
[18] Anggraini, V., Huat, B.B.K., Asadi, A., Nahazanan, H. 2015. Effect of coir fibers on the tensile and flexural strength of soft marine clay. Journal of Natural Fibers 12(2), 185-200.
[19] Prabakar, J., Sridhar, R.S. 2002. Effect of random inclusion of sisal fibre on strength behaviour of soil. Construction and Building Materials 16, 123–131.
[20] Ma, Q., Yang, Y., Xiao, H., Xing, W. 2018. Studying shear performance of flax fiber-reinforced clay by triaxial test. Hindawi Advances in Civil Engineering 2018, Article ID 1290572.
[21] Zaimoğlu, A.Ş., Akbulut, R.K. 2019. Effect of aspect ratio on the freezing thawing of a CH clay. Selçuk Üniversitesi Mühendislik Bilim ve Teknik Dergisi 7, 66-74.
[22] Ghazavi, M., Roustaie, M. 2010. The influenze of freeze thaw cycles on the unconfined compressive strength of fiber reinforced clay. Cold Regions Science and Technology 61, 125-131.
[23] Qu, J., Sun, Z. 2016. Strength behavior of Shanghai clayey soil reinforced with wheat straw fibers. Geotechnical and Geological Engineering 34, 515–527.
[24] Güllü, H., Khudir, A. 2014. Effect of freeze–thaw cycles on unconfined compressive strength of fine-grained soil treated with jute fiber, steel fiber and lime. Cold Regions Science and Technology 106-107, 55-65.
[25] Chaduvula, U., Viswanadham, B.V.S., Kodikara, J. 2017. A study on desiccation cracking behavior of polyester fiber-reinforced expansive clay. Applied Clay Science 142, 163-172.

EFFECTS OF UNCERTAINTY IN THE HYDRAULIC PROPERTIES FOR THE SEEPAGE ANALYSES OF RAINWATER INFILTRATION

UČINKI NEZANESLJIVOSTI HIDRAVLIČNIH LASTNOSTI NA ANALIZE PRONICANJA INFILTRACIJE DEŽEVNICE

Lin Zhou
Southeast University,
The Capital Construction Department
Nanjing, 210096 China

Yidong Zhao *(corresponding author)*
Technical University of Munich
Arccisstr. 21 80335 Munich Germany
E-mail: yidong.zhao@tum.de

DOI https://doi.org/10.18690/actageotechslov.19.1.63-76.2022

Keywords

soil-water characteristic curve, uncertainty, hydraulic properties, rainwater infiltration, hydraulic conductivity function

Ključne besede

karakteristična krivulja zemljina-voda, nezanesljivost, hidravlične lastnosti, infiltracija deževnice, funkcija hidravlične prepustnosti

Abstract

Rainwater infiltration is the crucial factor in any evaluation of rainfall-induced slope stability. The amount of rainwater infiltration is dependent on factors such as the rainfall intensity, the rainfall duration, the slope geometry, the hydraulic properties of the soil, and the initial pore-water pressure distribution. In this paper the effects of the variability in hydraulic properties of unsaturated soil on the rainwater's infiltration are investigated and discussed. Different hydraulic conductivity functions (HCFs) by considering the uncertainty in saturated volumetric water content (θ_s) and the soil-water characteristic curve (SWCC) are proposed. The seepage analyses for five cases (incorporating the uncertainty in θ_s, SWCC, and hydraulic conductivity, k_s) are conducted in this study. The results indicated that the effect of the variability in hydraulic properties of the unsaturated soil on the infiltration is much dependent on the initial suction in the slope soil. If the initial suction level is low (relatively wet conditions), then the variability in the hydraulic properties has an insignificant effect on the infiltration. On the contrary, if the initial suction level is high (relatively dry conditions), then the variability in the hydraulic properties has a significant effect on the infiltration.

Izvleček

Znano je, da je infiltracija deževnice ključni dejavnik za oceno stabilnosti pobočij, ki jih povzročajo padavine. Količina infiltracije deževnice je odvisna od dejavnikov, kot so intenzivnost padavin, trajanje padavin, geometrija pobočja, hidravlične lastnosti zemljin in začetna porazdelitev pornega vodnega tlaka. V prispevku so raziskani in obravnavani vplivi variabilnosti hidravličnih lastnosti nenasičenih zemljin na infiltracijo deževnice. Predlagane so različne funkcije hidravlične prepustnosti (HCF) z upoštevanjem nezanesljivosti pri nasičeni volumetrični vsebnosti vode (θ_s) in karakteristični krivulji zemljina-voda (SWCC). V tej študiji so bile izvedene analize pronicanja za pet primerov (vključujejo nezanesljivost (θ_s), SWCC in hidravlične prepustnosti, k_s). Rezultati analiz so pokazali, da je vpliv variabilnosti hidravličnih lastnosti nenasičenih zemljin na infiltracijo močno odvisen od začetne sukcije v pobočju. Če je začetni nivo sukcije nizek (sorazmerno mokro stanje), potem variabilnost hidravličnih lastnosti nima pomembnega vpliva na infiltracijo. Nasprotno, če je začetni nivo sukcije visok (relativno suho stanje), potem variabilnost hidravličnih lastnosti pomembno vpliva na infiltracijo.

1 INTRODUCTION

The seepage analysis plays an important role in a geotechnical analysis, especially for an analysis involving unsaturated soil. Umana et al. [1] and Ouzaid et al. [2] indicated that seepage analyses are important for both oil production and excavation works. The shear strength, which is the key parameter in the slope-stability analysis of unsaturated soil can be higher than that of saturated soil due to presence of matric suction in the soil (Vanapalli et al [3]., Goh, et al. [4], Zhai et al. [5] and Zhai et al. [6]. It should be noted that the shear strength of unsaturated soil can decrease dram atically when the soil's suction decreases during the infiltration. Therefore, a quantification of the rainwater infiltration is crucial for an evaluation of the rainfall-induced slope stability. The works from Ng and Shi [7], Toll [8], Chen et al. [9], Zhang et al. [10], Rahardjo et al. [11], Rahardjo et al. [12], Rahimi et al. [13] and Shoaib et al. [14] indicated that the rainwater infiltration is dependent on many factors, such as rainfall intensity, rainfall duration, slope geometry, hydraulic properties of the soil, etc. Zhai et al. [15, 16] also reported that the water flow in the soil may also be affected by the pore-size distribution function (PSDF). In addition, Satyanaga et al. [17] and Satyanaga and Rahardjo [18] showed that the variability in the soil-water characteristic curve (SWCC) could also behave in unimodal and bimodal shapes. In this study the effects of a variation in the hydraulic properties of the soil on the rainwater infiltration are investigated. In addition, only unimodal SWCC, which is applicable for most soils, is adopted in the analyses.

Richards's [19] governing differential equation, as illustrated in Equation (1), was commonly adopted for the seepage analysis.

$$\frac{\partial\left(k_x \frac{\partial H}{\partial x}\right)}{\partial x} + \frac{\partial\left(k_y \frac{\partial H}{\partial y}\right)}{\partial y} + Q = \frac{\partial \theta}{\partial t} \qquad (1)$$

where: H = total head, k_x = the hydraulic conductivity in the x-direction, k_y = the hydraulic conductivity in the y-direction, Q = the applied boundary flux, θ = the volumetric water content, and t = time.

As illustrated in Equation (1), the solution of Equation (1) is governed by the parameters of k_x , k_y , H, Q, θ and t. The parameters k_x , k_y and θ define the hydraulic properties of soil, while H and Q define the initial suction and the seepage boundary conditions, respectively. The values of k_x , k_y and θ, are dependent on the soil types and soil suction. The relationship between θ and the soil suction is commonly defined as the soil-water characteristic curve (SWCC), while the relationship between k_x (or k_y) and the soil suction is commonly defined as the permeability function. Equation (1) indicated that the water flow in unsaturated soil was mainly governed by the water-retention capacity (can be expressed as SWCC) and hydraulic conductivity of unsaturated soil (can be expressed as the hydraulic conductivity function, HCF).

Zhai and Rahardjo [20] proposed the first-order error method for the quantification of the uncertainty in SWCC and concluded that the high variability of SWCC occurred in the transition zone. (i.e., the suction zone between the air-entry value and the residual suction as defined by Vanapalli et al. [3]). Fredlund and Fredlund [21] suggested the hydraulic conductivity function of the unsaturated soil can be estimated from Zhai and Rahardjo's [22] equation using a Microsoft Excel spreadsheet.

It is observed that the variability in the hydraulic properties of unsaturated soils has been widely reported (Zapata [23], Dye et al. [24], Rahardjo et al. [25], Zhai et al. [26]). However, the effect of the variability in the hydraulic properties of unsaturated soil on the rainwater infiltration has not been extensively studied. In this paper, the uncertainty in volumetric water content and SWCC fitting parameters are estimated first. Subsequently, the HCFs of unsaturated soils, by incorporating uncertainty in θ_s and SWCC, are computed. Consequently, the parametric studies of the seepage analyses by considering the uncertainty in the hydraulic properties of unsaturated soils are carried out. The effect of the uncertainty in the hydraulic properties on the infiltration into the slope soil is investigated and discussed.

2 THEORY

As Arya and Paris's model [27] is commonly used for an estimation of the SWCC from the grain size distribution data (GSD) and the capillary model is commonly used for an explanation of the water flow in soil, both models are introduced and discussed in this section. The relationship between the saturated coefficient of permeability, k_s , and the saturated volumetric water content, θ_s , was also discussed. It is observed that a similar equation to the Kozeny-Carman equation (Kozeny [28] and Carman [29]) can be obtained by using both Arya and Paris's model [27] and the capillary model. Subsequently, the effect of the variability in the SWCC and the hydraulic conductivity is explained.

2.1 Comparison of Arya and Paris's model and the capillary model

Arya and Paris [27] proposed a physico-empirical model to estimate the SWCC from the GSD. In Arya and Paris's model [27], the soil element was divided into several fractions, with the porosity being the same. In each fraction, the solid portion represents the soil particle, while the void portion represents the porosity of the soil. On the other hand, the capillary model considers the pores in the soil as a series of cylindrical tubes with different sizes and statistical distributions. (Childs and Collis-George [30], Tuller et al. [31]). The water content in the soil can be simplified as the water amount exists in these tubes (with different sizes). Fredlund and Rahardjo [32] pointed out the limitations and apparent anomalies when the capillary model was used to interpret certain unsaturated soil phenomena.

It is noted that both Arya and Paris's model [27] and the capillary model treated pores in the soil as a series of cylindrical tubes. Arya and Paris's model [27] was proposed to explain the relationship between the grain size distribution (GSD) data and the pore-size distribution function (PSDF). Arya and Paris's method [27] can be regarded as a simplified procedure to assume the ratio of the solid and void tube is isotropic throughout a soil element. In the capillary model, only the tubes (regardless of the solid soil) are adopted to study the water flow through these tubes (or porous space in soil). As a result, the combination of Arya and Paris's model [27] and the capillary model provides a more comprehensive explanation of the PSDF and the water flow in soil.

2.2 Relationship between the hydraulic conductivity, k_S, and the saturated volumetric water content, θ_S

According to Arya and Paris's model [27], in each fraction, the ratio between the void volume and the soil volume remains constant and is equal to the porosity, n, as illustrated in Figure 1.

Consider that the fraction i has a thickness of h, the void volume in fraction i can be calculated from the volume of a tube with a radius of r_i and expressed as follows:

$$V_{void,i} = \pi r_i^2 h \qquad (2)$$

where r_i= radius of the pore in fraction i, $V_{void,i}$ = void volume in fraction i, h = thickness of fraction i. $V_{void,i} = nV_{total,i}$, $V_{total,i}$ = total volume of fraction i.

Then Equation (2) can be rearranged as follows:

$$\pi r_i^2 h = nV_{total,i} \qquad (3)$$

The area of the tube r_i represents the soil area that faces the water. As all the soil is submerged in the water under the fully saturated condition, the area of the tube r_i represents the area of the soil in fraction i and can be expressed as follows:

$$A_{soili} = 2\pi r_i h \qquad (4)$$

where $A_{soil,i}$ = soil area in fraction i. $A_{soil,i} = (1\text{-}n)\, A_{total,i}$, where $A_{total,i}$ = total area of fraction i.

Equation (4) can be rearranged as follows:

$$2\pi r_i h = (1-n)A_{total\,i} \qquad (5)$$

Assuming that the water flows through the tube following Hagen-Poiseuille's law, as illustrated in Equation (6).

$$q = \frac{\pi r^4}{8\eta}\frac{dh}{dl} \qquad (6)$$

where r = radius of the tube, η = dynamic fluid viscosity and dh/dl = pressure gradient.

Rearrange Equation (6) as Equation (7) as follows:

$$q = \frac{\pi r^4}{8\eta}\frac{dh}{dl} = \frac{\pi r^2}{8\eta}\left\{\frac{(2\pi r^2)}{(2\pi r)}\right\}^2\frac{dh}{dl} \qquad (7)$$

Substituting Equations (3) and (5) into Equation (7), Equation (8) can be obtained as follows:

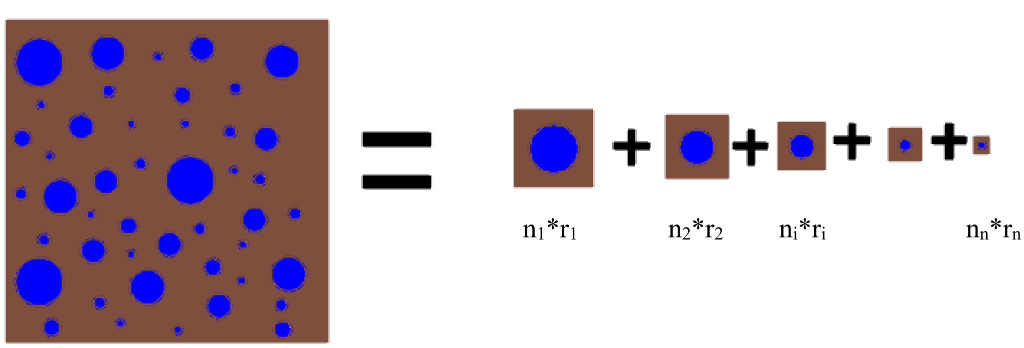

Figure 1. Illustration of the fractions of the soil element.

$$q_i = \frac{\pi r_i^2}{2\eta}\left(\frac{n v_{total}}{(1-n)A_{total}}\right)^2 \frac{dh}{dl} = \frac{\pi r_i^2}{2\eta}\left(\frac{n}{1-n}\right)^2\left(\frac{V}{A}\right)^2\frac{dh}{dl} \quad (8)$$

By summing all the fractions, the unit flux flow can be obtained as follows:

$$\begin{aligned} q &= \sum_{i=1}^{N} q_i = \sum_{i=1}^{N} \frac{\pi r_i^2}{2\eta}\left(\frac{n}{1-n}\right)^2\left(\frac{V}{A}\right)^2\frac{dh}{dl} \\ &= \frac{n}{2\eta}\left(\frac{n}{1-n}\right)^2\left(\frac{V}{A}\right)^2\frac{dh}{dl} = \frac{n^3}{(1-n)^2}\frac{1}{2\eta}\left(\frac{V}{A}\right)^2\frac{dh}{dl} \end{aligned} \quad (9)$$

where n = porosity,

Consider V/A= constant and Equation (9) has similar form to the Kozeny-Carman equation. Equation (9) indicates that the variation in the saturated coefficient of permeability, k_s, can be estimated from the variation in the porosity n. As the porosity is equal to the saturated volumetric water content, θ_s, the variation in k_s can be estimated from the variation in θ_s as follows:

$$\frac{k_{s2}}{k_{s1}} = \frac{\theta_{s2}^3}{(1-\theta_{s2})^2}\frac{(1-\theta_{s1})^2}{\theta_{s1}^3} \quad (10)$$

Equation (10) was used to correlate the saturated coefficient of permeability, k_s, and the saturated volumetric water content, θ_s, in this study.

2.3 Relationship between the porosity and the pore-size distribution function.

As illustrated in Figure 1, one soil element can be divided into serials of fractions such as n_1 numbers of fractions with a pore size equal to r_1, n_2 numbers of fractions with a pore size equal to r_2, a n_i numbers of fraction with a pore size equal to r_i --- and n_n numbers of fractions with a pore size equal to r_n. If the total pore area in the element is defined as A_{pore}, then the pore-size density corresponding to a pore with the radius r_i can be calculated from Equation (11) as follows:

$$f(r_i) = \frac{n_i \pi r_i^2}{A_{pore}} \quad (11)$$

where $f(r_i)$ = pore-size density corresponding to a pore with radius of r_i.

In fact, A_{pore} in the soil element is equal to θ_s if the area of the whole element is considered as 1. If θ_s is changed (either it increases or decreases), $f(r_i)$ can remain constant if $n_i \pi r_i^2$ changes with the same ratio as the changes in θ_s. In this case, the pore-size distribution function, $f(r)$, has no direct link to the saturated volumetric water content, θ_s. The saturated volumetric water content, θ_s, defines the ratio between the total pore volume and the soil-element volume, while $f(r_i)$ defines the ratio between the pore volume in fraction i to the total pore volume. As a result, there is possibility that a soil with a different saturated volumetric water content, θ_s, can have the same SWCC in the form of the degree of saturation. In other words, the soil with different saturated volumetric water content, θ_s, might not necessarily have different SWCCs, and vice versa.

3 NUMERICAL MODEL FOR THE INFILTRATION ANALYSES

Zhai et al. [26] presented the variability of the hydraulic conductivities for residual soil in Singapore. The work of Zhai et al. [26] provided a good reference for the uncertainty in the hydraulic properties for residual soil. Therefore, the residual soil from Singapore was adopted for the infiltration analyses in this study. A numerical model for seepage analyses was created using the commercial software Seep/w, as illustrated in Figure 2, to investigate the effect of the uncertainty of the hydraulic properties of the soil on the rainwater infiltration into the slope soil. A typical slope with H_s = 10m, a slope angle α = 45º, an initial depth of ground water table, H_w = 2m was adopted for the seepage analysis. In order to minimize the effects of the boundaries on the analyzed result, the distances between the boundaries and the slope were illustrated in Figure 2. In addition, the hydraulic conditions of the boundaries were defined in Figure 2. Rainfall with an intensity of 22 mm/hour for 24 hours was applied to the slope surface as a flux boundary, q. Ponding was not allowed to occur at the slope surface. In other words, the excess rainfall at the slope surface was removed as run-off. To make the analysis results comparable, $k_s = 6\text{x}10^{-6}$ m/s, which is within the range of k_s for residual soil in Singapore as presented by Zhai et al. [26], was assigned to the soil. The permeability function was estimated from SWCC using a statistical method with Zhai and Rahardjo's [22] equation.

Assuming θ_s follows a t-distribution and the standard deviation equal to 10 % of θ_s. The confidence limits of θ_s can be estimated as [0.8355θ_s, 1.1645θ_s] by adopting a 95 % confidence level. As a result, the variation in the saturated coefficient of permeability, ks, can be estimated from the uncertainty in θ_s using Equation (10). On the other hand, the variability in SWCC can only be determined if the uncertainty in the pore-size distribution function is known. Therefore, this study was started by estimating the uncertainty in the pore-size distribution function. Three different pore-size distribution functions, as illustrated in Figure 3, were adopted to introduce the variability in SWCC. In this case, a soil with a selected θ_s/k_s and SWCC was used for the seepage

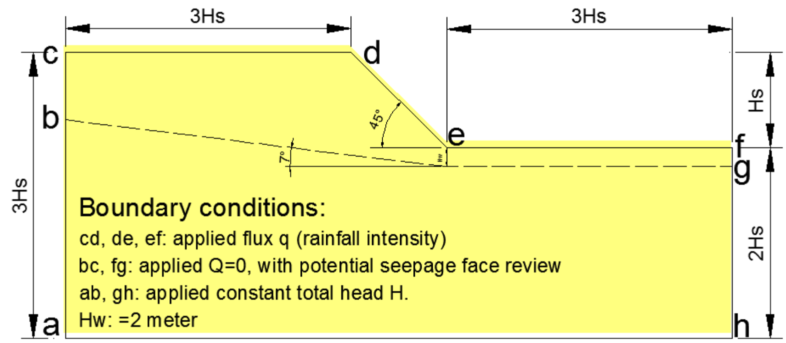

Figure 2. Slope geometry and boundary condition of residual soil.

analysis and named as Case A. To investigate the effect of variability in θ_s/k_s on the rainwater infiltration, the soil used in Case A was modified by considering a certain uncertainty in θ_s/k_s and named Case B+ and Case B-,

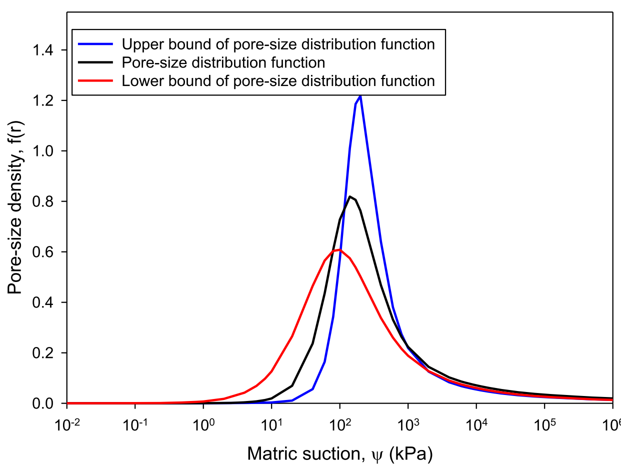

Figure 3. Illustration of variation of pore-size distribution function.

where "+" denotes the upper bound and "-" denotes the lower bound. On the other hand, to investigate the effect of variability in θ_s/k_s and SWCC on the rainwater infiltration, the soil used in Case B was further modified by considering the uncertainty in SWCC and named Case C+ and Case C-, where "+" denotes the upper bound and "-" denotes the lower bound. The fitting parameters in the Fredlund and Xing's equation [33] and the SWCC variables, which were determined using Zhai and Rahardjo's method [34], for the soils according to five scenarios were illustrated in Table 1. As illustrated in Table 1, Case A represents the condition where all the data are obtained from experimental measurements. Case B represents the condition that considers the uncertainty in the void ratio with reference to Case A. Case C represents the condition that considers the uncertainty in the void ratio and SWCC with reference to Case A.

The SWCCs and the permeability functions of the soils used in the five cases were illustrated in Figure 4.

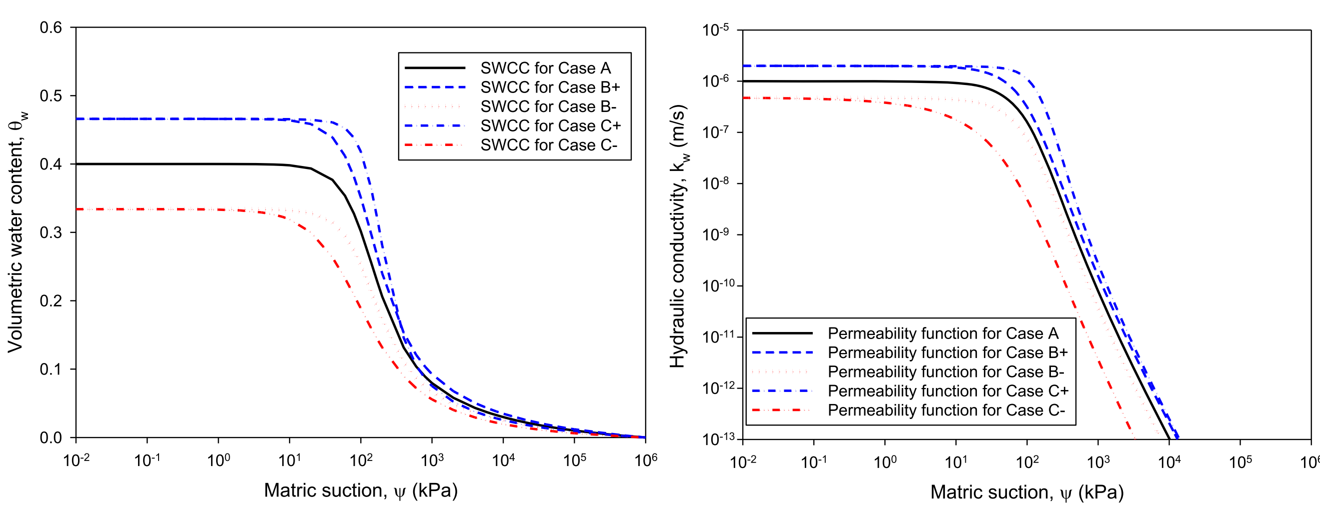

(a) SWCCs of the soils (b) Permeability functions of the soils

Figure 4. Illustration of SWCCs and permeability function of soils used in five cases.

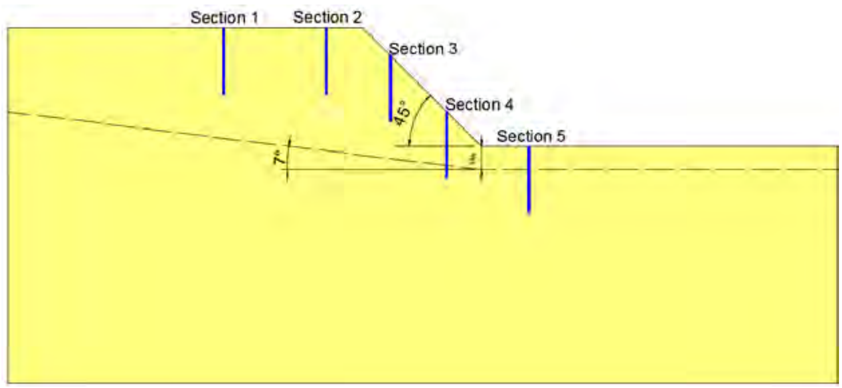

Figure 5. Illustration of sections for comparison of computed PWP.

Table 1. Illustration of hydraulic properties of soil for five cases.

Scenarios	θ_s	k_s	Parameters of SWCC				
			a_f	n_f	m_f	AEV	ψ_r
Case A	0.400	1.00E-06	100	2	1	51.24	461.25
Case B+	0.466	2.00E-06	100	2	1	51.24	461.25
Case B-	0.334	4.73E-07	100	2	1	51.24	461.25
Case C+	0.466	2.00E-06	150	3	1	94.88	473.70
Case C-	0.334	4.73E-07	60	1.3	1.3	19.34	461.3

where: a_f, n_f and m_f are the fitting parameters in the Fredlund and Xing's equation [34] and AEV and ψ_r are the air-entry value and the residual suction, respectively.

Pore-water pressure (PWP) profiles computed from seepage analyses using Seep/W were drawn based on five sections, as shown in Figure 5.

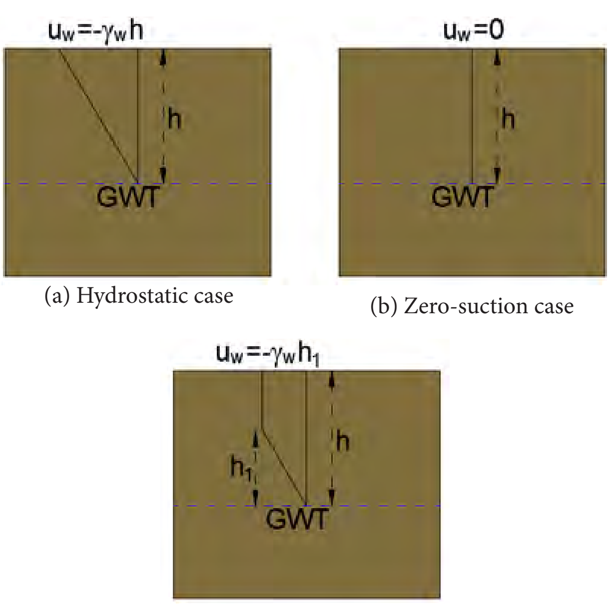

(a) Hydrostatic case

(b) Zero-suction case

(c) Limited maximum suction case

Figure 6. Illustration of three scenarios of suction distribution in the soil above the ground-water table (GWT).

The rainwater infiltration into the slope is also dependent on the initial suction in the soil. In this case, three scenarios, i.e., hydrostatic, zero-suction, and maximum suction of 5 meters of water head (as illustrated in Figure 6), were selected as the initial condition for the seepage analyses. In conventional saturated soil mechanics, (b) zero-suction is always considered, while in unsaturated soil mechanics both (a) hydrostatic and (c) limited maximum suction are considered for the seepage analysis.

4 RESULTS OF NUMERICAL ANALYSES

The computed pore-water pressures for five sections with initial pore-water pressure following the hydrostatic condition (scenario (a) in Figure 6) at different time steps were illustrated in Figure7.

As illustrated in Figure 7, the differences in the pore-water pressure profiles from different cases are larger on sections near the crest of the slope, as compared with those near the toe of the slope. As a result, the effect of the uncertainty in the hydraulic conductivity of unsaturated soil is more significant at a location near the slope crest than the slope toe. The differences in pore-water pressure (which represents rainwater infiltration) between case C and case A are greater than that between case B and case A, which means that considering the uncertainty in the void ratio and SWCC leads to a more significant effect on the infiltration than that considering the uncertainty in void ratio only. In addition, the differences in the PWP profile after 24 hours of rainfall are smaller than that obtained after 12 hours of rainfall, which indicates the difference in the PWP decrease with the increase in rainfall duration. It was also noted that after 24 hours of rainfall the pore-water pressure profiles from case B+ overlap with case C+, which indicates that the pore-water pressure profile under long-term rainfall conditions is mainly controlled by the saturated hydraulic conductivity, k_s.

The pore-water pressure profiles within five sections in Figure 5 with initial pore-water pressure following zero-suction condition (scenario (b) in Figure 6) at different time steps were illustrated in Figure 8. As the results after 6 hours rainfall are same as that after 12 hours and 24 hours of rainfall, respectively, only

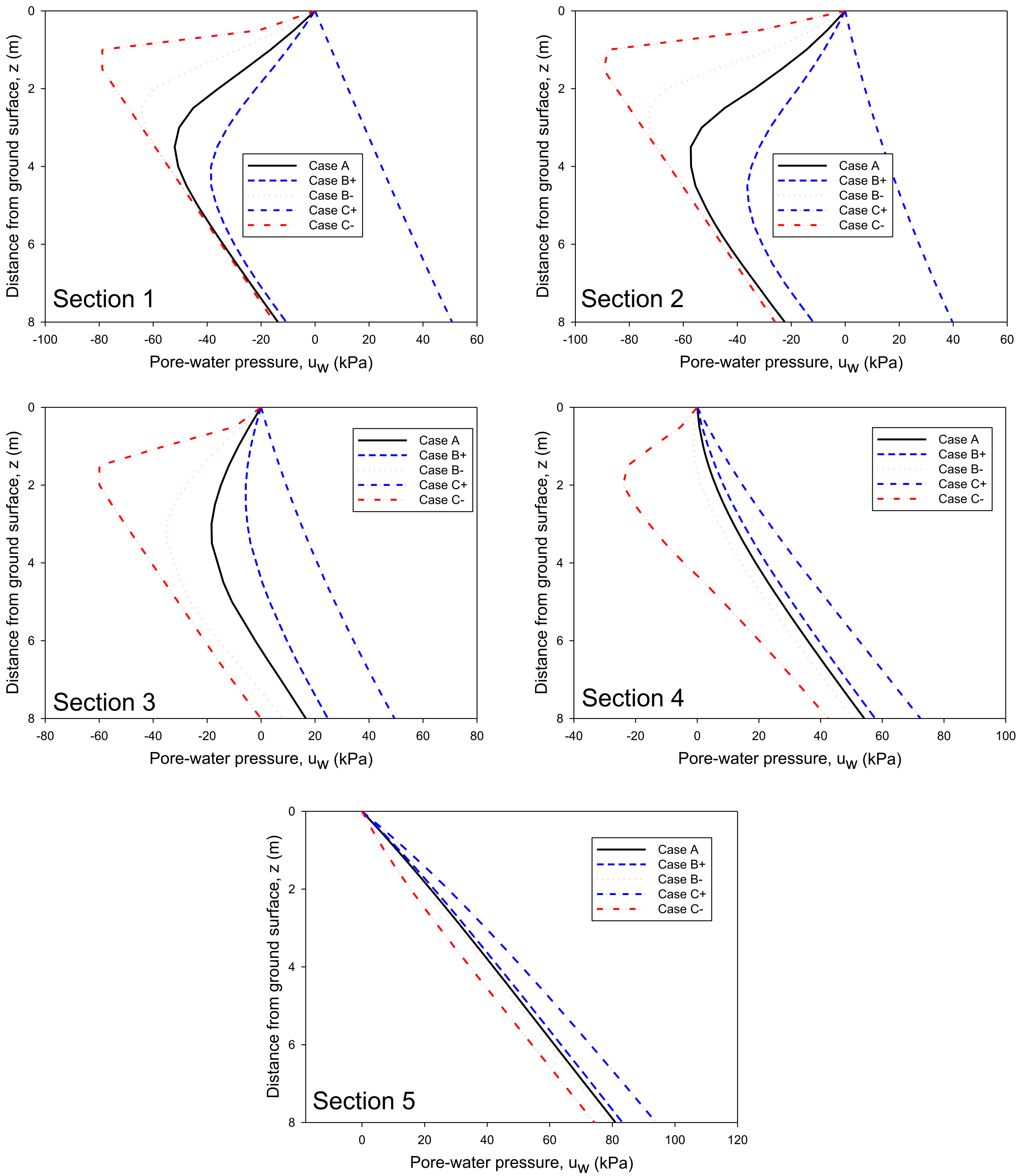

(a) Pore-water pressure profiles within five sections in Figure 5 after 12 hours of rainfall.

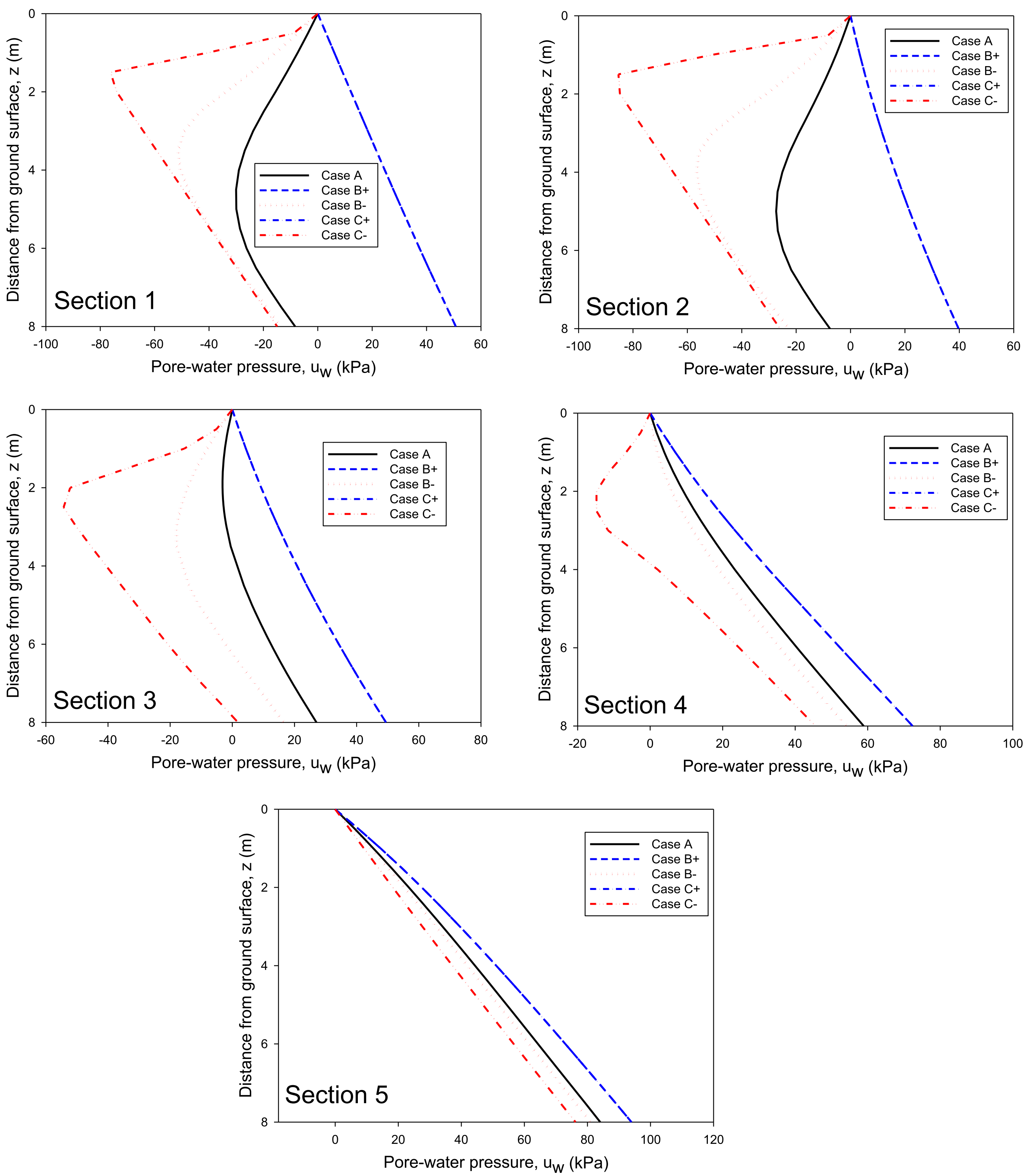

(b) Pore-water pressure profiles within five sections in Figure 5 after 24 hours of rainfall.

Figure 7. Pore-water pressure profiles within five sections in Figure 5 at different time steps.

the results after 24 hours of rainfall were illustrated in Figure 8.

The results shown in Figure 8 indicate that the computed pore-water pressure profiles from five cases overlap with each other. In other words, the rainwater infiltration rate is mainly governed by k_s if the initial soil condition is fully saturated.

The pore-water pressures profiles within five sections in Figure 5 with the initial condition having a maximum suction of 5 meters of water head (scenario (c) in Figure 6) at different time steps are illustrated in Figure 9.

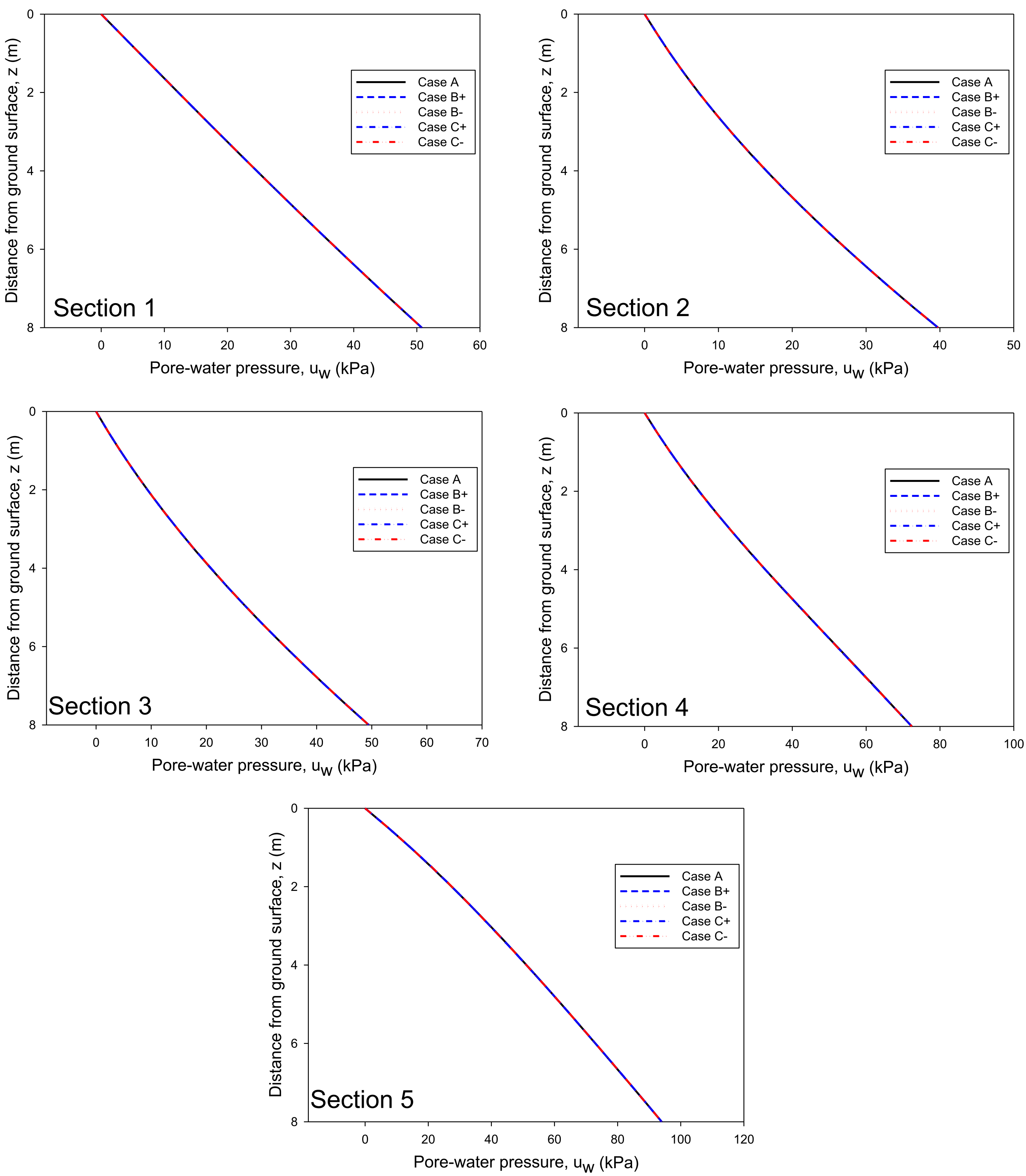

Figure 8. Pore-water pressure profiles for five sections after 24 hours of rainfall.

The results as illustrated in Figure 9 are similar to those in Figure 7. The results in Figure 9 indicated that the differences in the pore-water pressure profiles from the five cases in this scenario were smaller than that in the scenario of the hydrostatic condition.

Based on the results from Figures 7 to 9, it seems to be concluded that the effect of the initial suctions in the soil can be ignored if the rainfall period is long enough. To verify this point, these pore-water pressure profiles from three scenarios were re-drawn in the same figure

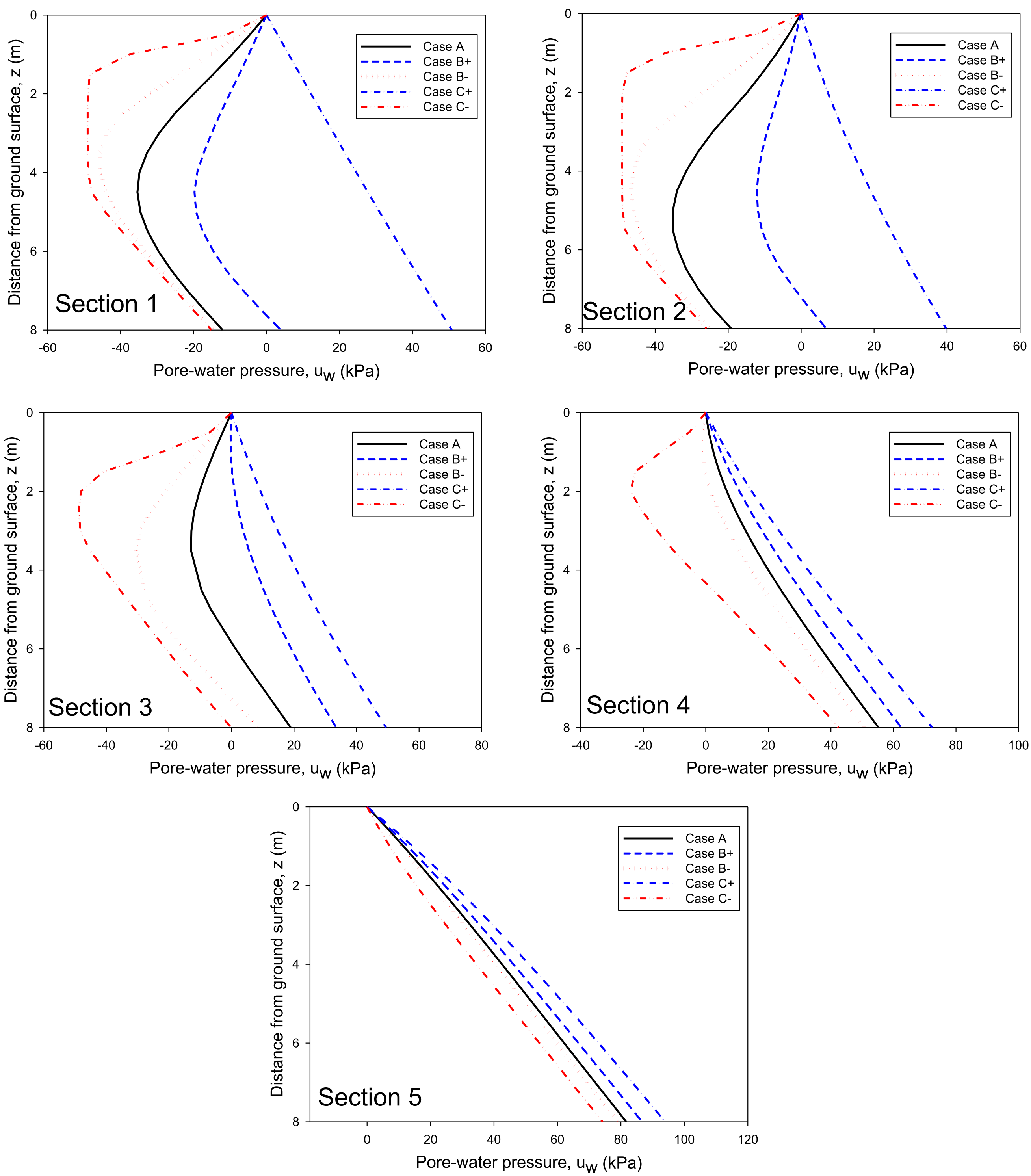

(a) Pore-water pressure profiles within five sections in Fig.5 after 12 hours of rainfall.

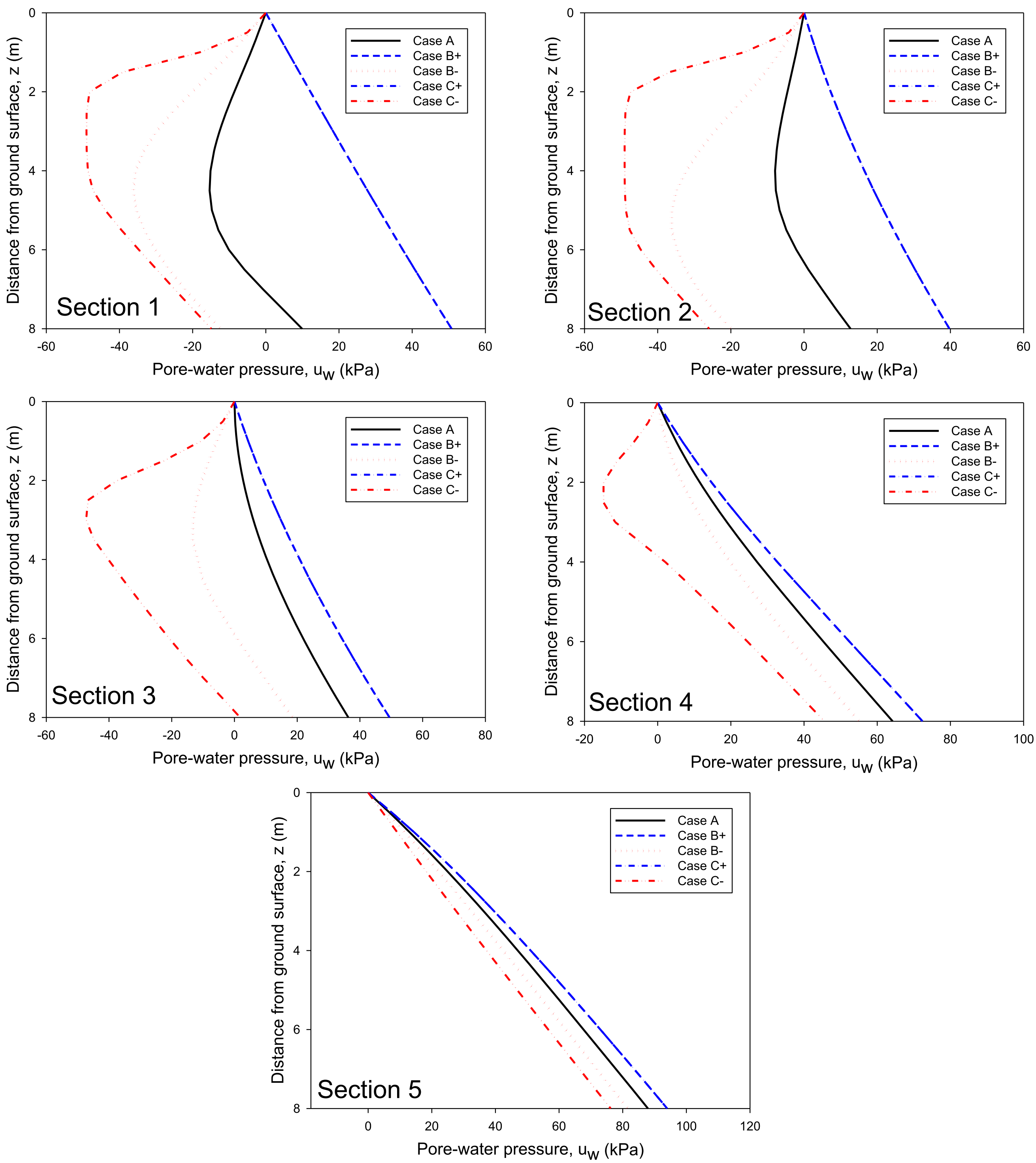

(b) Pore-water pressure profiles within five sections in Figure 5 after 24 hours of rainfall.

Figure 9. Pore-water pressure profiles for five sections at different time steps.

as illustrated in Figure 10. An additional line, named the hydrostatic line, which is computed from $\gamma_w z$, where γ_w is unit weight of water (9.81 kN/m^3), z is the vertical distance from the ground surface, is drawn in Figure 10.

Figure 10 indicated that the computed pore-water pressure profiles within five sections in Figure 5 after 24 hours of rainfall overlap with each other from three different scenarios. In other words, for the long-term rainfall condition, the rainwater's infiltration is mainly governed by the saturated hydraulic conductivity, k_s.

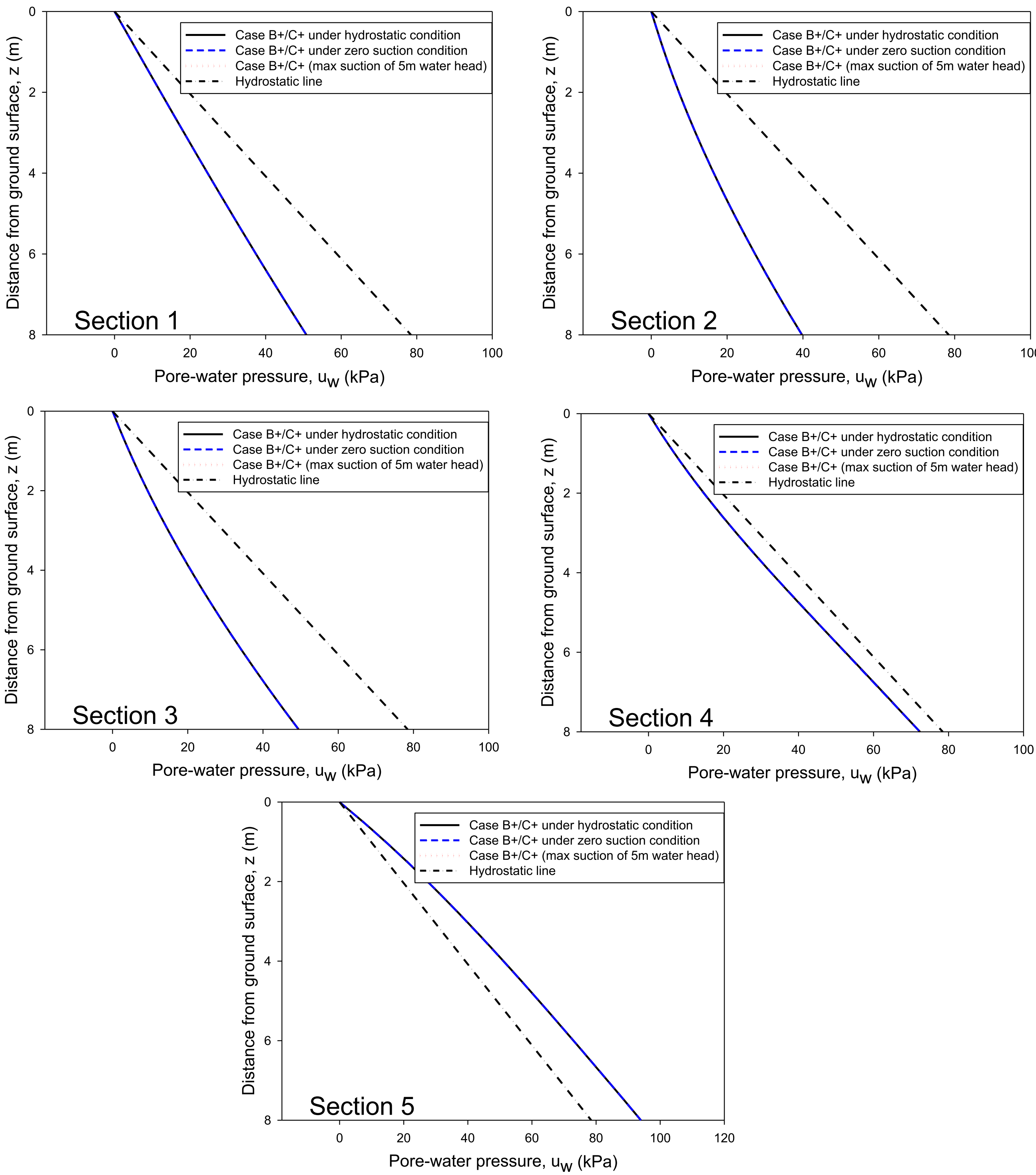

Figure 10. Comparison of pore-water pressure profiles within five sections under different scenarios.

5 CONCLUSIONS

An equation for describing the relationship between the saturated volumetric water content, θ_s, and the saturated coefficient of permeability, k_s was developed using both Arya and Paris's model [27] and the capillary model. The HCFs of the unsaturated soils are obtained by incorporating the uncertainty in the void ratio and SWCC. The seepage results indicated that when the initial suction in the slope soil is high (relatively dry condition), the uncertainty in the hydraulic properties of the unsaturated soil has a significant effect on the rainwater infiltration. In contrast, if the initial suction in the slope is low (relatively wet conditions), then the uncertainty in the hydraulic properties of the unsaturated soil has an insignificant effect on the rainwater's infiltration. It is also observed that the uncertainty in the hydraulic properties of the unsaturated soil has a more significant effect on the rainwater infiltration at the location near the slope crest than that near the slope toe. It is noted that the initial suction in the soil near the slope crest is higher than that near the slope toe. If the rainfall's duration is long enough, the seepage results indicated that the rainwater's infiltration is mainly governed by the saturated hydraulic conductivity.

REFERENCES

[1] Umana US, Ebong MS, and Godwin EO. (2020) "Biomass Production from Oil Palm and Its Value Chain" Journal of Human, Earth, and Future, Vol. 1, No. 1.

[2] Ouzaid I, Benmebarek N and Benmebarek S. (2020) "FEM Optimisation of Seepage Control System Used for Base Stability of Excavation" Civil Engineering Journal, Vol. 6, No. 09.

[3] Vanapalli S.K., Fredlund D.G., Pufahl D.E. and Clifton A.W. (1996) "Model for the prediction of shear strength with respect to soil suction". Can. Geotech J. 33 379-392.

[4] Goh, S.G., Rahardjo H. and Leong E.C. (2010). "Shear Strength Equations for Unsaturated Soil Under Drying and Wetting". ASCE Journal of Geotechnical and Geoenvironmental Engineering. 136(4):594 –606.

[5] Zhai Q., Rahardjo H. Satyanaga, A., and Dai G.L. (2019a) "Estimation of unsaturated shear strength from soil-water characteristic curve" Acta Geotechnica 14(6), 1977-1990

[6] Zhai Q., Rahardjo H., Satyanaga, A., Dai G.L. and Du YJ(2020a) "Effect of the uncertainty in soil-water characteristic curve on the estimated shear strength of unsaturated soil" Journal of Zhejiang University-SCIENCE A 21(4):317-330.

[7] Ng, C.W.W., and Shi, Q., (1998) "A numerical investigation of the stability of unsaturated soil slopes subjected to transient seepage." Computers and Geotechnics 22 (1), 1–28.

[8] Toll, D.G. (2001) "Rainfall-induced landslides in Singapore". Proceedings of the Institution of Civil Engineers: Geotechnical Engineering 149 (4), 211–216.

[9] Chen, H., Lee, C.F. and Law, K.T. (2004) "Causative mechanisms of rainfall-induced fill slope failures." Journal of Geotechnical and Geoenvironmental Engineering 130 (6), 593–602.

[10] Zhang, L.L., Zhang, L.M., Tang, W.H., (2005) "Rainfall-induced slope failure considering variability of soil properties." Geotechnique 55 (2), 183–188.

[11] Rahardjo, H., T.H. Ong, R.B. Rezaur and E.C. Leong (2007). "Factors Controlling Instability of Homogeneous Soil Slopes under Rainfall Loading". ASCE Journal of Geotechnical and Geoenvironmental Engineering. December, Vol. 133, No.12, pp. 1532 – 1543.

[12] Rahardjo, H., E.C. Leong and R.B. Rezaur (2008). "Effect of Antecedent Rainfall on Pore-water Pressure Distribution Characteristics in Residual Soil Slopes under Tropical Rainfall". Hydrological Processes, Special Issue on Rainfall Induced Landslides and Debris Flow, Vol. 22, pp. 506-523.

[13] Rahimi, A., H. Rahardjo and E.C. Leong (2010). "Effect of Hydraulic Properties of Soil on Rainfall-Induced Slope Failure". Journal of Engineering Geology, Vol. 114, pp. 135 – 143.

[14] Shoaib M, Wang Y, Yang L and Rehman G (2021) "Stability and Deformation Analysis of Landslide under Coupling Effect of Rainfall and Reservoir Drawdown", Civil Engineering Journal, Vol. 7, No. 07.

[15] Zhai Q., Rahardjo H., Satyanaga, A., Priono, and Dai G. L. (2019b) "Role of pore-size distribution function on the water follow in soil" Journal of Zhejiang University-SCIENCE A, 20(1): 10-20.

[16] Zhai Q, Rahardjo H, Satyanaga A, Dai GL, and Zhuang Y (2020b) "Framework to estimate the soil-water characteristic curve for the soil with different void ratios" Bulletin of Engineering Geology and the Environment, 79: 4399-4409

[17] Satyanaga A., Rahardjo H. and Zhai, Q (2017). "Estimation of unimodal water characteristic curve for gap-graded soil." Soils and Foundations, 57(5), 789-801.

[18] Satyanaga, A. and Rahardjo, H. (2018). "Unsaturated shear strength of soil with bimodal soil-water characteristic curve." Géotechnique, 69(9), 1-18.

[19] Richards L.A. (1931) "Capillary conduction of liquids through porous mediums" Physics volume 1: 318-333.

[20] Zhai Q, and Rahardjo H. (2013) "Quantification of uncertainty in soil-water characteristic curve associated with fitting parameters" Engineering Geology 163 (2013) 144-152.

[21] Fredlund DG and Fredlund MD. (2020) "Application of 'Estimation Procedures' in Unsaturated Soil Mechanics." Geosciences, 10: 364.

[22] Zhai Q, and Rahardjo H. (2015) "Estimation of

permeability function from Soil-Water Characteristic Curve" Engineering Geology 199 (2015) 148-156.

[23] Zapata, C. E. (1999). "Uncertainty in Soil-Water Characteristic Curve and Impacts on Unsaturated Shear Strength Predictions", Ph.D. Dissertation, Arizona State University, Tempe, United States.

[24] Dye H.B., Houston S.L. and Welfert B.D (2011) "Influence of Unsaturated Soil Properties Uncertainty on Moisture Flow Modeling." Geotech Geol Eng 29 (161-169)

[25] Rahardjo, H., A. Satyanaga, E.C. Leong and Y.S. Ng (2012). "Variability of Residual Soil Properties". Journal of Engineering Geology, June, Vol. 141–142, No. 124–140.

[26] Zhai Q., Rahardjo H. and Satyanaga, A. (2016) "Variability in unsaturated hydraulic properties of residual soil in Singapore" Engineering Geology 209: 21-29

[27] Arya, L.M. and Paris, J.F., (1981) "A physico-empirical model to predict the soil moisture characteristics from particle-size distribution and bulk density data." Soil Sci. Soc. Am. J. 45 (6), 1023–1030.

[28] Kozeny J (1927) "Ueber kapillare Leitung des Wassers in Boden." Sitzungsber Akad, Wiss., Wien Math. Naturwiss. Kl. Abt. 2a 13: 271-306 (in German)

[29] Carman, P.C. (1938). "Fundamental principles of industrial filtration - a critical review of present knowledge". Transactions of Institution of Chemical Engineering 16, 168–188.

[30] Chids, E.C., and Collis-George, G.N. (1950)" The permeability of porous materials." Proc. Royal Soc. of London, Series A. London, U.K., 201, 392-405.

[31] Tuller, M., D. Or, and L. M. Dudley (1999) "Adsorption and capillary condensation in porous media: Liquid retention and interfacial configurations in angular pores," Water Resour. Res., 35(7), 1949–1964.

[32] Fredlund, D. G. and Rahardjo H. (1993) "Soil Mechanics for unsaturated soil", Wiley, New York.

[33] Fredlund, D.G. and Xing, A. (1994) "Equations for the soil-water characteristic curve." Canadian Geotechnical Journal, 31(3): 521-532.

[34] Zhai, Q. and H. Rahardjo (2012). "Determination of Soil-Water Characteristic CurveVariables". Computer and Geotechnics, 42:37-43.

CALCULATING THE FUNDAMENTAL NATURAL FREQUENCY OF RETAINING WALLS, INCLUDING SHEAR-DEFORMATION EFFECT

IZRAČUN OSNOVNE NARAVNE FREKVENCE PODPORNIH ZIDOV, VKLJUČNO Z UČINKI STRIŽNE DEFORMACIJE

Kanat Burak Bozdogan *(corresponding author)*
Canakkale Onsekiz Mart University,
Department of Civil Engineering
17000, Canakkale Turkey
E-mail: kbbozdogan@comu.edu.tr

Muhammed Mahmudi
Ege University,
Department of Civil Engineering
35100 Bornova, Izmir, Turkey
E-mail: mu.mahmudi@hotmail.com

DOI https://doi.org/10.18690/actageotechslov.19.1.77-87.2022

Keywords

retaining wall, analytical method, Rayleigh method, natural frequency, shear

Ključne besede

podporni zid, analitična metoda, Rayleighova metoda, lastna frekvenca, strižna deformacija

Abstract

In this study, two analytical approaches were proposed to determine the fundamental natural frequencies of retaining walls. In the first method, the soil effect is taken into consideration with springs, while in the second method, the soil effect is considered as a continuous medium. Föpl Papkovich and Southwell's theorems and the Rayleigh method were used to obtain the presented approaches. It was assumed that the change of the inertial moment and the cross-sectional area can be expressed with an exponential function. In contrast to the analytical methods in the literature, shear deformations in the retaining wall are also taken into account in the presented methods. In the second method presented in the study, Southwell's theorem was originally used for the interaction of the retaining wall with the soil. With the methods presented in the study, the fundamental natural frequency of the retaining wall can be determined practically with the help of created tables. At the end of the definition of the method, to determine the suitability of the approaches, an example from the literature was solved and the results were evaluated together. The example discussed in the study was also modeled with SAP2000. The results show that the methods presented in this study give results closer to the Abaqus results compared to the method in the literature. Considering the shear deformations in the retaining wall in the methods presented in this study is the main reason for this.

Izvleček

V tej študiji sta bila predlagana dva analitična pristopa za določitev osnovnih naravnih frekvenc podpornih zidov. Pri prvi metodi se upošteva učinek tal z vzmetmi, pri drugi metodi pa se učinek tal obravnava kot neprekinjen medij. Za pripravo predstavljenih pristopov so bili uporabljeni Föpl Papkovich in Southwellovi izreki ter Rayleighova metoda. Predpostavili smo, da je spremembo vztrajnostnega momenta in površine preseka mogoče izraziti z eksponentno funkcijo. Za razliko od analitičnih metod v literaturi so v predstavljenih metodah upoštevane tudi strižne deformacije v podpornem zidu. Pri drugi metodi, predstavljeni v študiji, je bil Southwellov izrek prvotno uporabljen za interakcijo podpornega zidu s tlemi. Z metodami, predstavljenimi v študiji, lahko s pomočjo izdelanih tabel praktično določimo osnovno naravno frekvenco podpornega zidu. Na koncu smo za ugotavljanje primernosti predstavljenih metod rešili primer iz literature in ovrednotili dobljene rezultate. Primer, obravnavan v študiji, je bil tudi modeliran s SAP2000. Rezultati kažejo, da metode predstavljene v tej študiji, dajejo rezultate, ki so bližje rezultatom Abaqusa v primerjavi z rezultati metode v literaturi. Glavni razlog za to je, da so se pri metodah predstavljenih v tej študiji v podpornem zidu upoštevale strižne deformacije.

1 INTRODUCTION

The stability and safety of shoring structures under static and dynamic load conditions are some of the important problems in geotechnical engineering. In recent years, slope failures and serious structural damage, and thus significant financial losses have occurred during the San Francisco (1906), San Fernando (1971), Northridge (1994), Kobe (1995), Chichi (1999), and Adapazarı (1999) earthquakes. For example, Figure 1 shows a trapezoidal concrete gravity retaining wall that rotated outward due to the failure of the slope above during the 1999 Chi-Chi earthquake in Taiwan. Therefore, shoring systems play an important role during an earthquake against slope failures and the instability of the backfill soils, especially under permanent load conditions. Retaining walls that are categorized as flexible elements are a common shoring system that is widely used in shallow excavations, road embankments, and railways due to their simple structural forms and convenient constructions. In this case, a soil-structure interactions analysis of the retaining walls under seismic loadings are very important aspects in geotechnical and structural engineering. Besides that, a safe design and estimate of the dynamic-response magnitudes of retaining walls are very important due to its influence on the dynamic displacements under seismic loadings.

In recent years, several researchers like Okabe [2], Seed and Whitman [3], Whitman et al. [4], Duzgun and Bozdag [5], Wang et al. [6], Xu [7], Darvishpour et al. [8], Bakr et al. [9] have worked on the seismic response of gravity-type retaining walls. However, their study methods and findings may be partially or completely invalid for common reinforced concrete walls because of differences in their characters. On the other hand, based on pseudo-static, pseudo-dynamic, and limit equilibrium approaches, several researchers [2, 10, 11, 12, 13, 14, 15, 16, 17, 18] have developed different methods to determine the seismic earth pressure to unit weight of a retaining wall due to earthquake loading. Also, the natural frequency of backfill soils has been calculated and estimated by several researchers by defining the Winkler springs, elastic wave theory, an analytical method [19, 20, 21], linear elastic theory [22, 23], centrifuge model tests [24], shaking-table tests [25], the Rayleigh method [21], transfer-matrix methods [26] and using differential equations or finite-element methods [21, 27, 28, 29]. Hatemi and Bathurst [30] investigated the effect of structural design on the fundamental frequency of reinforced retaining walls. A desire to highlight that the influence of wall facing that is very important in a seismic-response analysis has not been considered in most of these methods. Besides these theoretical methods, many field tests have been carried out to study the natural frequencies of retaining walls, and this is still preferred by researchers.

Figure 1. Retaining wall rotated due to slope failure during the Chi-Chi earthquake (1999) in Taiwan [1].

In this study, two analytical approaches were proposed to determine the fundamental natural frequency of retaining walls. Föpl Papkovich and Southwell's theorems and the Rayleigh method were used to obtain the presented approaches. It was accepted that the change of the inertial moment and the cross-sectional area can be expressed with an exponential function.

2 ANALYTICAL APPROACHES

In this study, unlike studies in the literature, shear displacements on the retaining wall are also taken into account. With the methods presented in the study, the fundamental natural frequency of the retaining wall can be determined practically with the help of a created table. To evaluate and verify the results, the findings of Ghanbari et al. [21] based on the assumption of a beam on elastic foundations theory and finite-element analysis were used. In developing the methods, it is accepted that the retaining wall and the soil show linear elastic behavior.

2.1 First method

The mathematical model of the retaining wall, whose physical model is shown in Figure 2, is written as the free-vibration equation of the Timoshenko beam on the Elastic Winkler foundation as follows.

$$\frac{d^2}{dz^2}\left[EI(z)\frac{d^2y_B}{dz^2}\right]+sy-\rho A\omega^2 y=0 \qquad (1)$$

$$\frac{d}{dz}\left[GA'(z)\frac{dy_S}{dz}\right]-sy+\rho A\omega^2 y=0 \qquad (2)$$

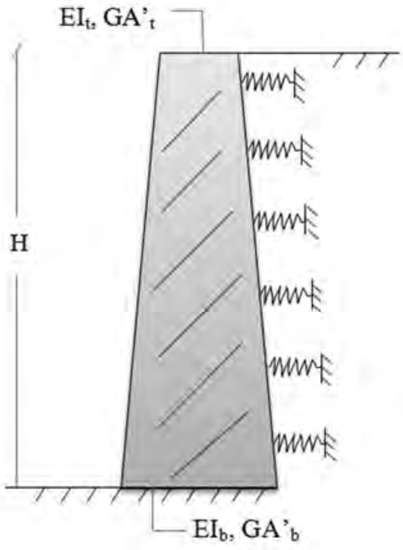

Figure 2. Timoshenko beam with variable cross-section representing the retaining wall.

where E is the modulus of elasticity, G is the shear modulus, $I(z)$ is the moment of inertia function, $A'(z)$ is the equivalent shear area function, $A(z)$ is the area function, ω is the natural frequency, s is the Winkler coefficient per unit length, ρ is the unit volume mass. z shows the axis extending along the height of the retaining wall and y is the total lateral displacement function, y_B is the displacement function consisting of bending, and y_S is the shear displacement. The total displacement can be illustrated using the equation below:

$$y(z) = y_B + y_S \qquad (3)$$

Differential Eqs. (1) and (2) can be written in dimensionless form with Eqs. (5) and (6) with the help of the transformation Eq. (4).

$$\varepsilon = \frac{z}{H} \qquad (4)$$

$$\frac{1}{H^4}\frac{d^2}{d\varepsilon^2}\left[EI(\varepsilon)\frac{d^2 y_B}{d\varepsilon^2}\right] + sy - \rho A\omega^2 y = 0 \qquad (5)$$

$$\frac{1}{H^2}\frac{d}{d\varepsilon}\left[GA'(\varepsilon)\frac{dy_S}{d\varepsilon}\right] - sy + \rho A\omega^2 y = 0 \qquad (6)$$

The cross-sectional areas of the retaining wall at the top level and the base level are as follows:

$$A_0 = v_b * 1 \qquad (7)$$

$$A_t = v_t * 1 \qquad (8)$$

In this study, the change of the cross-sectional area along the retaining-wall height was accepted as an exponential function as follows:

$$A(\varepsilon) = A_0\, e^{-a\varepsilon} \qquad (9)$$

where the value of a is defined as follows:

$$a = -ln\frac{A_t}{A_0} = -ln\frac{v_t}{v_0} \qquad (10)$$

The moment of inertia of the retaining wall at the level of the base and the peak is found using the following relations.

$$I_0 = \frac{{v_b}^3}{12} * 1 \qquad (11)$$

$$I_t = \frac{{v_t}^3}{12} * 1 \qquad (12)$$

The moment-of-inertia function along the retaining-wall height is written as follows:

$$I(\varepsilon) = I_0\, e^{-3a\varepsilon} \qquad (13)$$

where the expression $3a$ is calculated as follows:

$$3a = -ln\frac{I_t}{I_0} = -ln\frac{{v_t}^3}{{v_0}^3} = -3 * -ln\frac{v_t}{v_0} \qquad (14)$$

The Föppl Papkovich theorem can be used to find the angular frequency and the buckling-load factor in systems whose stiffness can be expressed by a series spring model, such as the Timoshenko beam.The fundamental natural frequency of the retaining wall is calculated according to the Föpl Papkovich theory [31, 32] as follows:

$$\omega = \sqrt{\frac{\omega_B^2 * \omega_S^2}{\omega_B^2 + \omega_S^2}} \qquad (15)$$

ω_B is the fundamental natural frequency consisting of bending displacements, calculated using the equation [21, 33] below:

$$\omega_B^2 = \frac{\int_0^1 EI(\varepsilon)*[y''(\varepsilon)]^2*d\varepsilon}{H^4*\int_0^1 \rho*A(\varepsilon)*[y(\varepsilon)]^2*d\varepsilon} + \frac{\int_0^1 s*[y(\varepsilon)]^2*d\varepsilon}{\int_0^1 \rho*A(\varepsilon)*[y(\varepsilon)]^2*d\varepsilon} \qquad (16)$$

In Eq. (16), if Eq. (13) is written instead of $I(\varepsilon)$, Eq. (9) instead of $A(\varepsilon)$, and Eq. (17) instead of y, Eq. (18) is obtained.

$$y = 1 - \cos\left(\frac{\Pi\varepsilon}{2}\right) \qquad (17)$$

Eq. (17) is the approximate first mode shape of a cantilever bending beam [33].

$$\omega_B^2 = \frac{\Pi^4*\int_0^1 EI_o*\left[e^{-3a\varepsilon}\right]*\left[\cos\left(\frac{\Pi\varepsilon}{2}\right)\right]^2*d\varepsilon}{16*H^4\int_0^1 \rho A_0*\left[e^{-a\varepsilon}\right]*\left[1-\cos\left(\frac{\Pi\varepsilon}{2}\right)\right]^2*d\varepsilon} + \frac{\int_0^1 s*\left[1-\cos\left(\frac{\Pi\varepsilon}{2}\right)\right]^2*d\varepsilon}{\int_0^1 \rho A_0*\left[e^{-a\varepsilon}\right]*\left[1-\cos\left(\frac{\Pi\varepsilon}{2}\right)\right]^2*d\varepsilon} \qquad (18)$$

Eq. (18) can be written as follows:

$$\omega_B^2 = k_1 \frac{EI_o}{H^4 \rho A_0} + k_2 \frac{s}{\rho A_0} \qquad (19)$$

where k_1 and k_2 are written as follows:

$$k_1 = \frac{\Pi^4 * \int_0^1 [e^{-3a\varepsilon}] * \left[\cos\left(\frac{\Pi\varepsilon}{2}\right)\right]^2 * d\varepsilon}{16 \int_0^1 [e^{-a\varepsilon}] * \left[1-\cos\left(\frac{\Pi\varepsilon}{2}\right)\right]^2 * d\varepsilon} \qquad (20)$$

$$k_2 = \frac{\int_0^1 \left[1-\cos\left(\frac{\Pi\varepsilon}{2}\right)\right]^2 * d\varepsilon}{\int_0^1 [e^{-a\varepsilon}] * \left[1-\cos\left(\frac{\Pi\varepsilon}{2}\right)\right]^2 * d\varepsilon} \qquad (21)$$

The fundamental frequency consisting of shear displacements is found according to the Rayleigh method as follows:

$$\omega_S^2 = \frac{\int_0^1 GA'(\varepsilon) * [y'(\varepsilon)]^2 * d\varepsilon}{H^2 * \int_0^1 \rho * A(\varepsilon) * [y(\varepsilon)]^2 * d\varepsilon} + \frac{\int_0^1 s * [y(\varepsilon)]^2 * d\varepsilon}{\int_0^1 \rho * A(\varepsilon) * [y(\varepsilon)]^2 * d\varepsilon} \qquad (22)$$

In Eq. (22), if the Eq. (9) is written instead of $A(\varepsilon)$ and if Eq. (23) is assumed for the cantilever shear beam as the first mode shape, Eq. (24) is written as follows:

$$y = \sin\left(\frac{\Pi\varepsilon}{2}\right) \qquad (23)$$

$$\omega_S^2 = \frac{\Pi^2 * \int_0^1 GA'_0 * [e^{-a\varepsilon}] * \left[\cos\left(\frac{\Pi\varepsilon}{2}\right)\right]^2 * d\varepsilon}{4 * H^2 * \int_0^1 \rho A_0 * [e^{-a\varepsilon}] * \left[\sin\left(\frac{\Pi\varepsilon}{2}\right)\right]^2 * d\varepsilon} + \frac{\int_0^1 s * \left[\sin\left(\frac{\Pi\varepsilon}{2}\right)\right]^2 * d\varepsilon}{\int_0^1 \rho A_0 * [e^{-3a\varepsilon}] * \left[\sin\left(\frac{\Pi\varepsilon}{2}\right)\right]^2 * d\varepsilon} \qquad (24)$$

Eq. (24) can be written as follows:

$$\omega_S^2 = k_3 \frac{GA'_o}{H^2 \rho A_0} + k_4 \frac{s}{\rho A_0} \qquad (25)$$

where k_3 and k_4 are defined as follows:

$$k_3 = \frac{\Pi^2 * \int_0^1 [e^{-a\varepsilon}] * \left[\cos\left(\frac{\Pi\varepsilon}{2}\right)\right]^2 * d\varepsilon}{4 * \int_0^1 [e^{-a\varepsilon}] * \left[\sin\left(\frac{\Pi\varepsilon}{2}\right)\right]^2 * d\varepsilon} \qquad (26)$$

$$k_4 = \frac{\int_0^1 \left[\sin\left(\frac{\Pi\varepsilon}{2}\right)\right]^2 * d\varepsilon}{\int_0^1 [e^{-3a\varepsilon}] * \left[\sin\left(\frac{\Pi\varepsilon}{2}\right)\right]^2 * d\varepsilon} \qquad (27)$$

In this study, the integrals in Eqs (20), (21), (26) and (27) are solved numerically using the trapezoidal rule, and the change of the calculated k values depending on the ratio of v_t/v_b is given in Table 1. However, the k values can be obtained easily from the curves given in Figure (3).

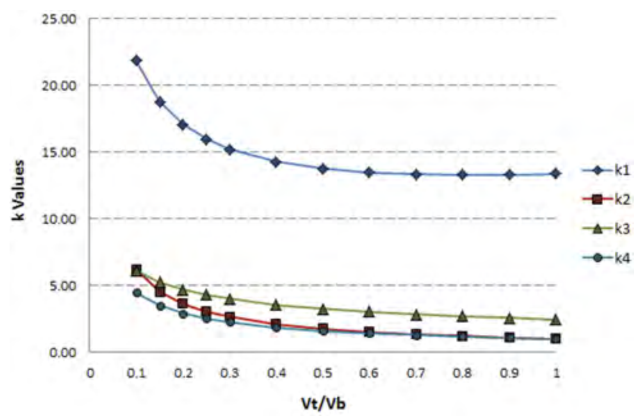

Figure 3. k-coefficient curves depending on v_t/v_b values.

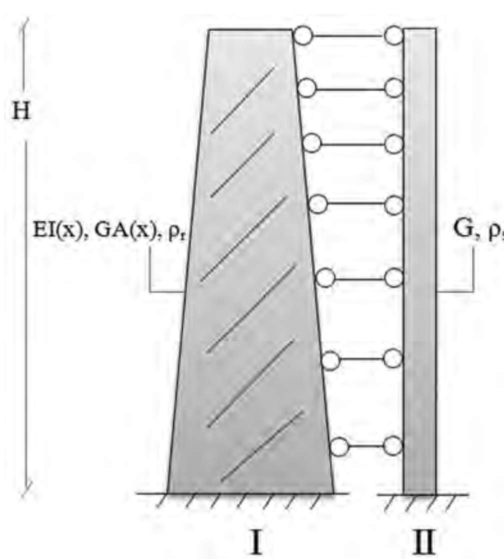

Figure 4. Coupled beam model representing the retaining wall.

Table 1. Change of k coefficients depending on v_t/v_b.

a	1	0.9	0.8	0.7	0.6	0.5	0.4	0.3	0.25	0.2	0.15	0.1
k_1	13.40	13.32	13.29	13.34	13.48	13.76	14.28	15.20	15.97	17.07	18.78	21.85
k_2	1.00	1.09	1.20	1.34	1.52	1.76	2.10	2.64	3.05	3.63	4.54	6.20
k_3	2.46	2.57	2.70	2.84	3.03	3.26	3.56	4.00	4.29	4.69	5.24	6.12
k_4	1.00	1.08	1.16	1.16	1.42	1.61	1.87	2.26	2.54	2.92	3.50	4.47

2.2 Second method

In this approach, the retaining wall can be modeled as an equivalent variable Timoshenko beam, whereas the soil part can be modeled as an equivalent shear beam, as in Figure 4.

In this case, the following equation can be written according to Southwell's theorem [32].

$$\omega^2 = \omega_I^2 + \omega_{II}^2 \qquad (28)$$

The fundamental natural period of the soil is written as follows, as is known from the literature.

$$T_{II} = \frac{4*H}{v_s} \qquad (29)$$

where v_s is the shear velocity of the soil.

Using Eq. (29), the square of the fundamental natural frequency can be calculated using the equation below.

$$\omega_{II}^2 = \frac{2.467*{v_s}^2}{H^2} \qquad (30)$$

The fundamental natural frequency of the retaining wall represented by the Timoshenko beam I can be written as follows using the Föppl-Papkovich theorem [31, 32].

$$\omega_I^2 = \frac{k_1 \frac{EI_O}{H^4 \rho A_0} k_3 \frac{GA'_O}{H^2 \rho A_0}}{k_1 \frac{EI_O}{H^4 \rho A_0} + k_3 \frac{GA'_O}{H^2 \rho A_0}} = \frac{k_1 k_3 \frac{EI_O GA'_O}{H^6 (\rho A_0)^2}}{k_1 \frac{EI_O}{H^4 \rho A_0} + k_3 \frac{GA'_O}{H^2 \rho A_0}} \qquad (31)$$

Table 1 can be used to find k_1 and k_3.

If Eqs (30) and (31) are replaced in Eq. (28), the fundamental natural frequency of the system is written as follows:

$$\omega = \sqrt{\frac{2.467*{v_s}^2}{H^2} + \omega_I^2} \qquad (32)$$

If the presented model is made with a program that performs finite-element analysis, the following modification should be made instead of the soil shear modulus so that Southwell's theorem can be used. In addition, pA will be taken as the mass per unit length in the shear beam representing the soil part.

$$G_s = G_s \frac{\rho A_0}{\rho_s} \qquad (33)$$

where G_s and ρ_s represent the shear modulus and density of the soil, respectively.

3 APPLICATION STEPS OF THE METHODS

The process steps of the method presented in this study are briefly summarized below:

- v_t/v_b ratio is determined
- Using Table 1, the k_1, k_2, k_3, and k_4 parameters are determined.
- For method 1, the fundamental natural frequency of the retaining wall is determined with the help of Eqs. (19), (25) and (15).
- For method 2, the fundamental natural frequency of the retaining wall is determined with the help of Eq. (32).

The flow chart of the two methods presented in this study is given in Figure 5 (next page).

4 EVALUATION AND VERIFICATION BY EXAMPLE

To investigate the suitability of the methods presented in this study, three samples taken from the literature were solved and the results were compared.

4.1 Example 1

The fundamental natural frequency of the retaining-wall example taken from the literature [21] was solved with the methods presented in this study and the results were compared with the literature [21]. The properties of the retaining wall are given in Table 2.

Table 2. Properties of Example 1.

Properties of retaining wall	
H (m)	3/4/5/6/8/10
v_s (m)	1
v_b (m)	0.4
v_b/v_s	0.4
a	0.916
Modulus of elasticity (GPa)	26
Poisson's ratio	0.2
ρ (kg/m^3)	2320
Properties of backfill	
C (kPa)	0
φ (°)	30
ρ (kg/m^3)	1900

With the help of Table 1, the k coefficients for a = 0.916 value were determined and the fundamental natural frequency values were determined for different H values with the help of Eqs. (19), (25), (15) and (32). In the study, in addition, the given retaining wall was modeled with the SAP2000 program. In SAP 2000, the retaining wall and the soil are modeled with shell elements. Figure 6 presents a view of the SAP 2000 model.

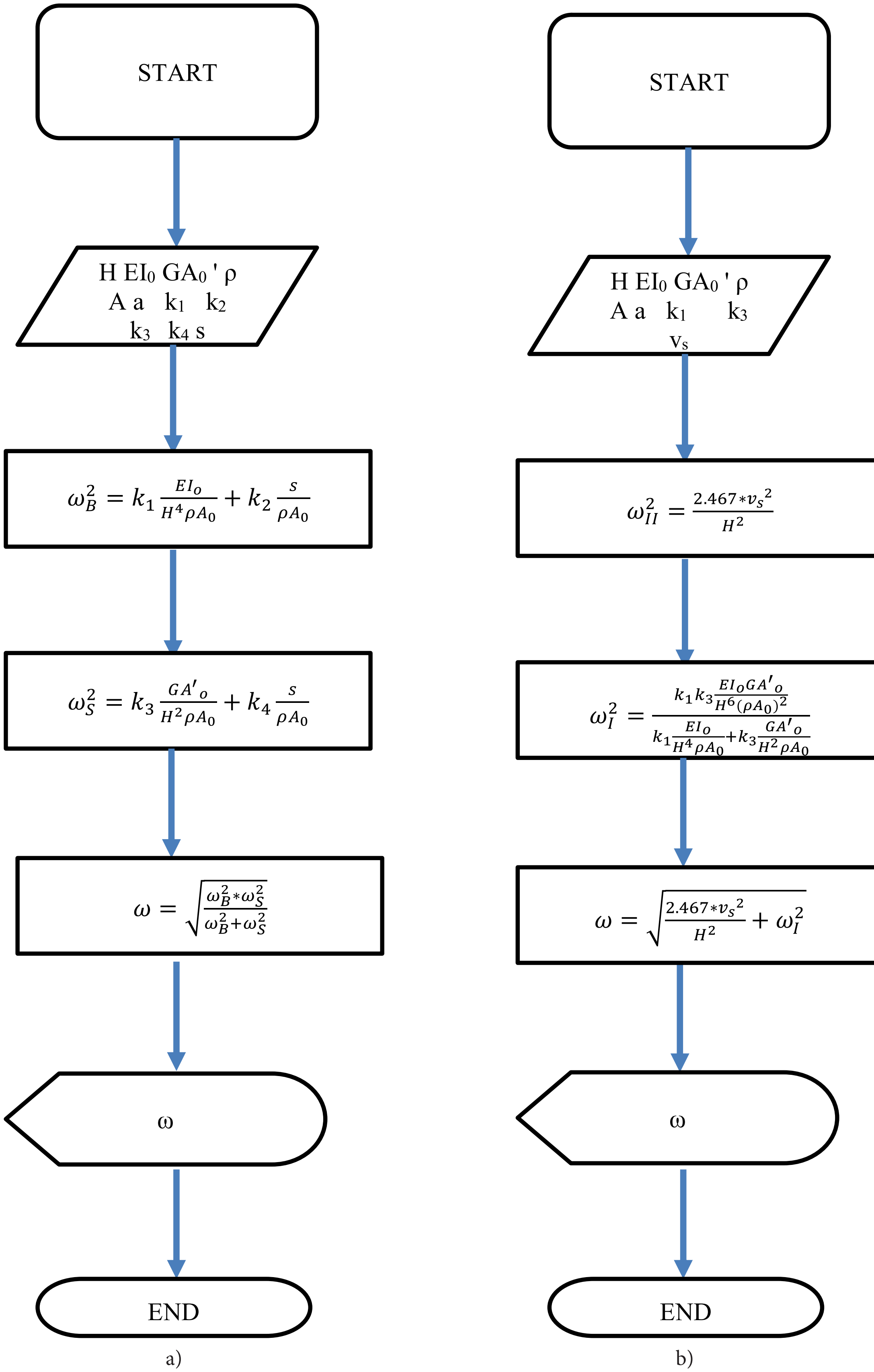

Figure 5. Flow chart of proposed method a) First method b) Second method.

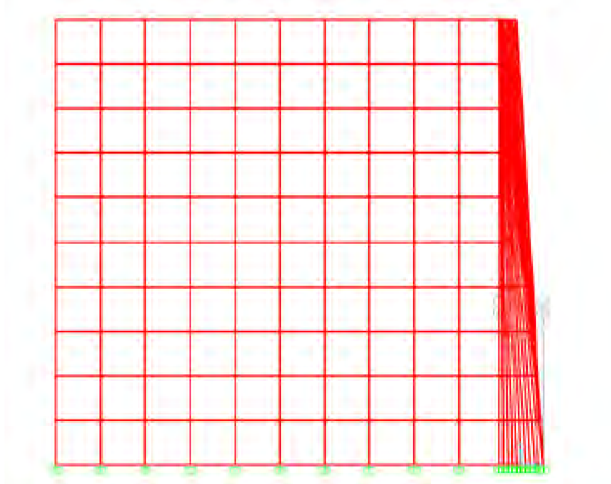

Figure 6. Modeling the retaining wall with SAP 2000.

The step-by-step application of the two methods presented in this study for H = 3 m is shown below.

1. First method

First of all, the k values for a = 0.916 were found from Table 1 as follows:

$$k_1 = 13.33,\ k_2 = 1.080,\ k_3 = 2.55 \text{ and } k_4 = 1.07$$

Using equation (19), ω_b^2 is calculated as follows:

$$\omega_B^2 = 13.33 * \frac{2.6*10^7*0.0833}{3^4*2.32*1} + 1.080 * \frac{3100}{2.32*1} = 155072.91\, rad^2/s^2$$

Using equation (25), ω_s^2 is calculated as follows:

$$\omega_S^2 = 2.55\frac{10833333.33*1*0.86}{3^2*2.32*1} + 1.07 * \frac{3100}{2.32*1} = 1139241.0\ rad^2/s^2$$

According to the first method, the angular frequency for the H = 3 retaining wall is found using Equation (15), as follows:

$$\omega = \sqrt{\frac{155072.91 * 1139241.0}{155072.91 + 1139241.0}} = 369.45\, rad/s$$

2. Second method

For H = 3 m with the second method, first Equation (31) is applied as follows:

From the given data, the shear wave velocity is obtained as follows:

$$v_s = \sqrt{\frac{G}{\rho_s}} = \sqrt{\frac{17300}{2*(1+0.3)*1.5}} = 66.603\, m/s$$

For the soil part, if Equation (30) is applied, ω_{II}^2 is found as follows:

$$\omega_{II}^2 = \frac{2.467*66.602^2}{3^2} = 1215.9093\, rad^2/s^2$$

$$\omega = \sqrt{1215.9093 + 135354.01} = 369.55\, rad/s$$

For the other heights the fundamental natural frequencies were calculated using the two methods presented in this study and compared with the literature and SAP 2000 results in Table 3.

Since the soil effect is modeled more realistically in Abaqus, the closest result to the exact result is the result obtained with Abaqus. For this reason, Abaqus is taken as a basis for calculating the error.

As can be seen from Table 3, the fundamental natural frequencies obtained in this study are closer to the results obtained from the Abaqus program, compared to the results found using the method proposed by Ghanbari et al. [21]. It was indicated in Figure 7 that

Table 3. Comparison of results for H = 3 m, 4 m, 5 m, 6 m, 8 m, and 10 m.

Study		Natural frequency (rad/sec)					
	H (m)	3	4	5	6	8	10
	s (kN/m/m)	3100	2320	1860	1550	1160	930
First method (a)		369.45	214.74	140.62	99.81	59.16	40.63
Second method (b)		369.55	214.15	139.37	97.94	56.15	36.59
Ghanbari et al. [21] (c)		434.22	246.23	159.65	112.97	67.25	46.69
Ghanbari et al. [21] (Abaqus) (d)		374.63	205.32	131.05	100.53	60.24	40.45
SAP2000 (e)		396.42	229.48	151.48	105.96	61.14	39.76
Error of the first method ,% (a-d)/d		-1.38%	4.59%	7.30%	-0.72%	-1.79%	0.44%
Error of the second method, % (b-d)/d		-1.33%	4.30%	6.35%	-2.58%	-6.79%	-9.54%

$$\omega_I^2 = \frac{13.33 * 2.55 * \dfrac{2.6 * 10^7 * 0.0833 * 10833333.33 * 1 * 0.86}{3^6 * 2.32^2 * 1}}{13.33 * \dfrac{2.6 * 10^7 * 0.0833}{3^4 * 2.32 * 1} + 2.55 * \dfrac{10833333.33 * 1 * 0.86}{3^2 * 2.32 * 1}} = 135354.01$$

compared to the Abaqus results [21], in 3 m ≤ H ≤ 10 m ranges the magnitude of the fundamental natural frequencies obtained from the second method are 0.90–1.06 times, the natural frequencies obtained from the first proposed method are 0.99 and 1.07 times, and the natural frequencies obtained from the Ghanbari et al. [21] proposed method are between 1.16 and 1.22 times. Both proposed methods give close values compared to the Abaqus results.

It was indicated from Figure 8, in 3 m ≤ H ≤ 10 m ranges according to the results obtained by Abaqus the error values of the first method are changed from 0.44 % to 7.30 %, and the error values of the second method are changed from -1.33 to 9.54. As can be seen, the error values of the first method are less than the second method.

It was also indicated from Figure 9, in 3 m ≤ H ≤ 10 m ranges the magnitude of the fundamental natural

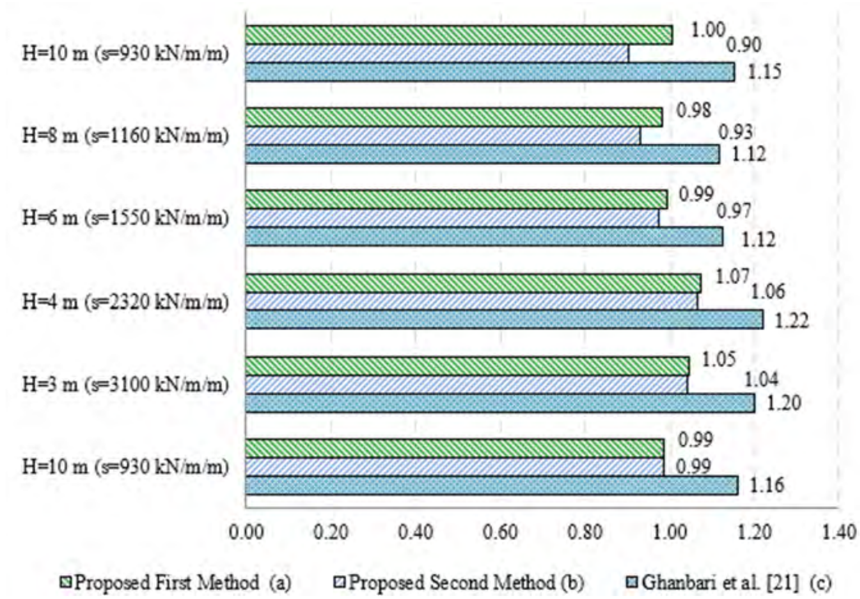

Figure 7. Natural frequencies that result from rates compared to the Abaqus results [21].

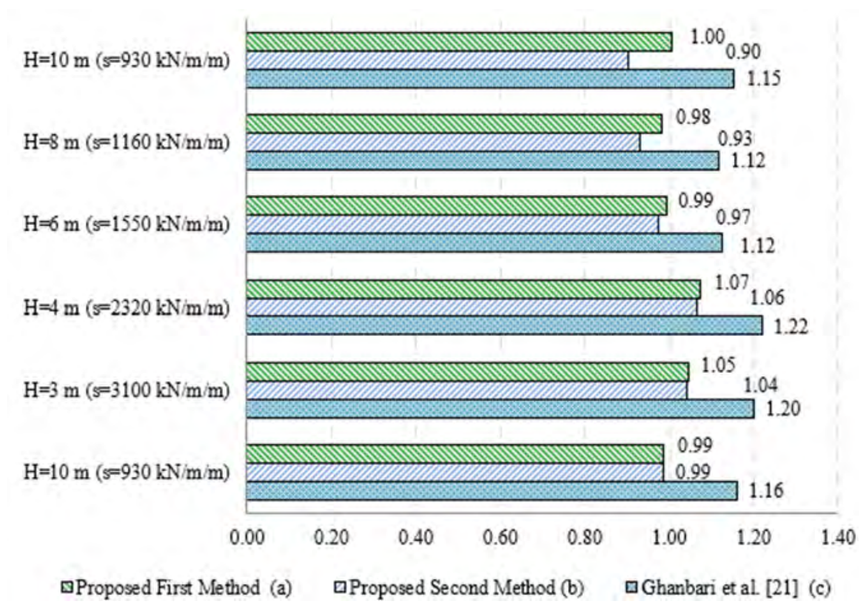

Figure 8. Error-values of the proposed method compared to the Abaqus results (Ghanbari et al. [21]).

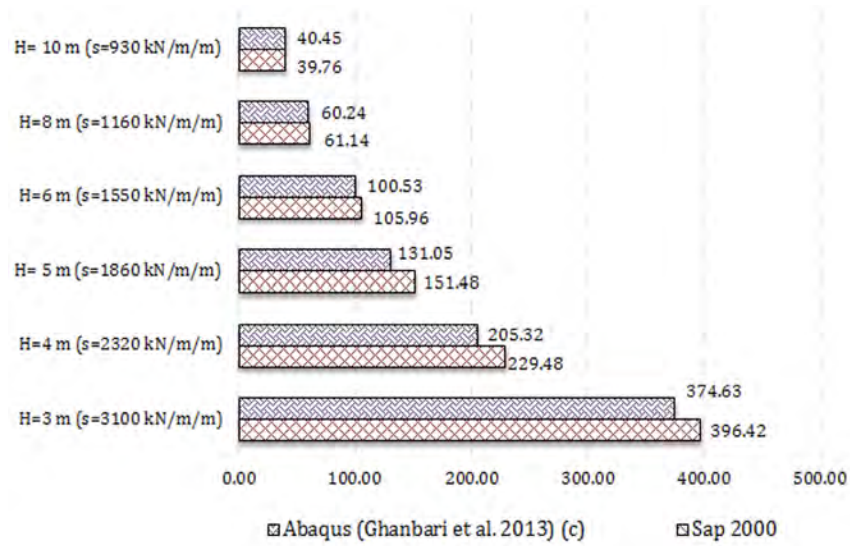

Figure 9. Natural frequencies obtained from Sap 2000 compared to the Abaqus results [21].

frequencies obtained from Sap 2000 are very close to the Abaqus results [21].

4.2 Example 2

In this example, the properties of the retaining-wall sample taken from the literature are given in Table 4. The given retaining-wall sample was solved by the methods presented in this study and the results obtained were compared with field-test results and numerical simulation results in the literature [35].

Comparison of the frequency value obtained with the methods presented in this study with the literature is presented in Table 5.

Table 5. Comparison of results for Example 2.

Method	Fundemantal frequency (Hz)
First method	9.31
Second method	9.43
Field test (Klymenkov et al., 2016)	8
Numerical simulation (Klymenkov et al. 2016)	9.46

As can be seen, the results obtained by the two methods presented in this study gave results consistent with the numerical analysis in the literature.

Table 4. Properties of Example 2.

Properties of retaining wall	
H (m)	5
v_s (m)	0.40
v_b (m)	0.40
v_b/v_s	1.0
a	0
Modulus of elasticity (GPa)	25
Poisson’s ratio	0.2
ρ (kg/m^3)	2300
Properties of backfill	
E (MPa)	19
Poisson’s ratio	0.15
ρ (kg/m^3)	1900

Table 6. Properties of Example 3.

Properties of retaining wall	
H (m)	2.2
v_s (m)	0.20
v_b (m)	0.20
v_b/v_s	1.0
a	0
Modulus of elasticity (GPa)	21.1
Poisson’s ratio	0.2
ρ (kg/m^3)	2500
Properties of backfill	
E (MPa)	15.4
Poisson’s ratio	0.30
ρ (kg/m^3)	1900

4.3 Example 3

In this example, the fundamental frequency value of the retaining-wall sample taken from the literature was solved with the methods presented in this study and compared with the field-test results and the transfer -matrix method given in the literature. The properties of the retaining wall are given in Table 6 (previous page).

A comparison of the fundamental frequencies of the given retaining wall found by the methods presented in this study with the literature is given in Table 7.

As can be seen from Table 7, the second method presented in this study gave results closer to field test and the numerical solution.

Table 7. Comparison of results for Example 3.

Method	Fundemantal frequency (Hz)
First method	24.28
Second method	21.07
Field test (Xu [36])	22.41
Transfer-matrix method (Xu and Jiang [26])	21.37

5 CONCLUSIONS

In this study, two practical methods have been developed for determining the fundamental natural frequency of the retaining walls commonly used in practice in a free--vibration analysis. Although integral calculations are used in the development of the presented methods, no integral calculation is required in the application of the methods. With the table and curves given in the study, it is possible to reach the results practically and quickly without any integration. In the presented methods, shear displacements on the retaining wall are also taken into account in the analysis. The methods presented from the example solved at the end of the study are sufficiently compatible with the finite-element method. The methods presented in this study gave results closer to the results obtained with Abaqus than the analytical method given in the literature. In the methods presented in this study, considering the shear deformations in the retaining wall beside the flexural deformations is considered as the main reason for this.

It was observed that the second of the presented methods gave closer results to the finite-element method. The main reason for this was evaluated as the more realistic modeling of the effect of the soil in the second model.

The presented methods are useful in the preliminary stage and to give an idea about the behavior of the retaining wall by using a few parameters.

REFERENCES

[1] Sitar, N., Geraili Mikola, R. and Candia, G. 2012. Seismically induced lateral earth pressures on retaining structures and basement walls. Geotechnical Engineering State of the Art and Practice: Keynote Lectures from GeoCongress, pp. 335-358.

[2] Okabe, S. 1924. General theory of earth pressure and seismic stability of retaining wall and dam. Journal of the Japanese Society of Civil Engineers, 10(5): 1277-1323.

[3] Seed, H.B. and Whitman, R.V. 1970. Design of earth retaining structures for dynamic loads. ASCE Specialty Conference, Lateral Stresses in the Ground and Design of Earth Retaining Structures, Cornell Univ., Ithaca, New York, pp. 103-147.

[4] Whitman, R.V. 1990. Seismic design and behavior of gravity retaining walls. Proceedings of Specialty Conference on Design and Performance of Earth-Retaining Structures, ASCE Special Publication No. 25: 817–842.

[5] Duzgun, M. and Bozdag, O. 2003. Distribition of seismic earth presure acting on retaining walls. Teknik Dergi,Turkey.

[6] Wang, L., Chen, G. and Chen, S. 2015. Experimental study on seismic response of geogrid reinforced rigid retaining walls with saturated backfill sand. Journal of Geotextiles and Geomembranes, 43(1): 35-45.

[7] Xu, Q. 2016. Damage identification investigation of retaining wall structures based on a virtual impulse response function. Shock and Vibration, Volume 2016 Article ID 1346939.

[8] Darvishpour, A.,Ghanbari, A., Husseini, S.A.A., Nekooei, M. and Darvishpour, T. 2018. An analytical model for determining the effect of damping on 3D natural frequency of reinforced walls. Jornal Of Measurements in Engineering , 6(1):36-52

[9] Bakr, J., Ahmad, S.M., Lombardi, D. 2019. Finite-element study for seismic structural and global stability of cantilever-type retaining walls. International Journal of Geomechanics (ASCE),19(10): 04019117.

[10] Mononobe, N. and Matsuo, H. 1929. On the determination of earth pressures during earthquakes. Proceedings of World Engineering Congress, 9:177- 185.

[11] Choudhury, D. and Nimbalkar, S.S. 2006. Pseudo-dynamic approach of seismic active earth pressure

behind retaining wall. Geotechnical and Geological Engineering, 24:1103-1113.

[12 Nimbalkar, S. and Choudhury, D. 2007.Sliding stability and seismic design of retaining wall by pseudo-dynamic method for passive case. Soil Dynamics and Earthquake Engineering, 27 (6):497–505.

[13] Dewaikar, D.M. and Halkude, S.A.2002. Seismic passive/active thrust on retaining wall- point of application. Soils and Foundations, 42(1): 9-15.

[14] Madhav, M.R. and Kameswara Rao, N.S.V. 1969. Earth Pressures under Seismic Conditions. Soils and Foundations. 9(4):33-47.

[15] Choudhury, D. and Nimbalkar, S.S. 2006. Pseudo-dynamic approach of seismic active earth pressure behind retaining wall. Geotechnical and Geological Engineering, 24: 1103–1113.

[16] Choudhury, D. 2004. Seismic passive resistance at soil-wall interface. 17th ASCE Engineering Mechanics.

[17] Subba Rao, K.S., Choudhury, D. 2005. Seismic passive earth pressures in Soils. Journal of Geotechnical and Geoenvironmental Engineering, ASCE, 131(1): 131-135.

[18] Steedman, R.S and Zeng, X. 1990. The influence of phase on the calculation of pseudo-static earth pressure on a retaining wall", Geotechnique, 1:103-112.

[19] Matsuo, H. and Ohara, S. 1960. Lateral earth pressure and stability of quay walls during earthquakes. Proceedings of the 2nd World Conference on Earthquake, Tokyo-Kyoto, Japan,.1: 165-81.

[20] Wood, J.H. 1973. Earthquake-induced earth pressures on structures. Report No. EERL 73-05, California Institute of Technology, Pasadena, California.

[21] Ghanbari, A., Hoomaan, E. and Mojallal, M. 2013. An analytical method for calculating the natural frequency of retaining walls", International Journal of Civil Engineering, 11(1): 1-9.

[22] Scott, R.F. 1973. Earthquake-induced earth pressures on retaining walls. Proceedings of the 5th World Conference on Earthquak Engineering. Rome, Italy, 2: 1611-20.

[23] Wu, G. and Finn, W.D.L. 1996. Seismic pressures against rigid walls. Proceedings of the ASCE Specialty Conference on Analysis and Design of Retaining Structures against Earthquakes, pp. 1-18. Washington, DC, USA.

[24] Nakamura, S. 2006. Reexamination of Mononobe-Okabe theory of gravity retaining walls using centrifuge model tests. Soils and Foundations, 46(2):135-146.

[25] Huang, C.C., Horng, J.C., Chang, W.J., Chiou, J.S. and Che,n C.H. 2011. Dynamic behavior of reinforced walls-horizontal displacement response. Geotextiles and Geomembranes, 29(3): 257-267.

[26] Xu, P. and Jiang, G. 2019. Calculation of natural frequencies of retaining walls using the transfer matrix method. Advances in Civil Engineering, Volume 2019, Article ID 2156475, 8 pages.

[27] Maheshwari, B.K., Truman, K.Z., Gould, P.L. and El Naggar, M.H. 2005. Three-dimensional nonlinear seismic analysis of single piles using finite element model: effects of plasticity of soil. International Journal of Geomechanics, 5(1): 35-44.

[28] Dey, S., Mukhopadhyay, T., Khodaparast, H.H. and Adhikari, S. 2015. Stochastic natural frequency of composite conical shells. Acta Mechanica, 226(8) 2537-2553.

[29] Real, T., Zamorano, C., Ribes, F. and Real, J.I. 2015. Train-induced vibration prediction in tunnels using 2D and 3D FEM models in time domain. Tunnelling and Underground Space Technology, 49: 376–383.

[30] Hatami, K. and Bathurst, R.J. 2000. Effect of structural design on fundamental frequency of reinforced soil retaining walls. Soil Dynamics and Earthquake Engineering; 19: 137-157.

[31] Tarnai, T. 1995. Summation theorems in structural stability. Springer Verlag-Wien GmbH, Udine.

[32] Kaviani, P., Rahgozar, R. and Saffari, H. 2008. Approximate analysis of tall buildings using sandwich beam models with variable cross-section. The Structural Design of Tall And Special Buildings, 17:401-418.

[33] Dym, C.L. and Williams, H.E. 2012. Analytical Estimates of Structural Behavior. CRC press, Boca Raton,

[34] SAP2000, 2020. Structural Software for Analysis and Design, Evaluation Version. Computers and Structures.

[35] Klymenkov, O.A., Trofymchuk, A.N., Khavkin, K.A. and Berchun, I.A. 2016. Experimental diagnostics and mathematical modelling of stress-strain state of a railway retaining wall. Bulletin of the Belarusian-Russian University, 1(50), 140–148.

[36] Xu, Q. 2015. Damage identification and alarming for pile plate retaining wall. Chongqing University, Chongqing, Chongqing.

NAVODILA AVTORJEM

Vsebina članka

Članek naj bo napisan v naslednji obliki:

- Naslov, ki primerno opisuje vsebino članka in ne presega 80 znakov.
- Izvleček, ki naj bo skrajšana oblika članka in naj ne presega 250 besed. Izvleček mora vsebovati osnove, jedro in cilje raziskave, uporabljeno metodologijo dela, povzetek izidov in osnovne sklepe.
- Največ 6 ključnih besed, ki bi morale biti napisane takoj po izvlečku.
- Uvod, v katerem naj bo pregled novejšega stanja in zadostne informacije za razumevanje ter pregled izidov dela, predstavljenih v članku.
- Teorija.
- Eksperimentalni del, ki naj vsebuje podatke o postavitvi preiskusa in metode, uporabljene pri pridobitvi izidov.
- Izidi, ki naj bodo jasno prikazani, po potrebi v obliki slik in preglednic.
- Razprava, v kateri naj bodo prikazane povezave in posplošitve, uporabljene za pridobitev izidov. Prikazana naj bo tudi pomembnost izidov in primerjava s poprej objavljenimi deli.
- Sklepi, v katerih naj bo prikazan en ali več sklepov, ki izhajajo iz izidov in razprave.
- Vse navedbe v besedilu morajo biti na koncu zbrane v seznamu literature, in obratno.

Dodatne zahteve

- Vrstice morajo biti zaporedno oštevilčene.
- Predložen članek ne sme imeti več kot 18 strani (brez tabel, legend in literature); velikost črk 12, dvojni razmik med vrsticami. V članek je lahko vključenih največ 10 slik. Isti rezultati so lahko prikazani v tabelah ali na slikah, ne pa na oba načina.
- Potrebno je priložiti imena, naslove in elektronske naslove štirih potencialnih recenzentov članka. Urednik ima izključno pravico do odločitve, ali bo te predloge upošteval.

Enote in okrajšave

V besedilu, preglednicah in slikah uporabljajte le standardne označbe in okrajšave SI. Simbole fizikalnih veličin v besedilu pišite poševno (npr. v, T itn.). Simbole enot, ki so sestavljene iz črk, pa pokončno (npr. Pa, m itn.). Vse okrajšave naj bodo, ko se prvič pojavijo, izpisane v celoti.

Slike

Slike morajo biti zaporedno oštevilčene in označene, v besedilu in podnaslovu, kot sl. 1, sl. 2 itn. Posnete naj bodo v katerem koli od razširjenih formatov, npr. BMP, JPG, GIF. Za pripravo diagramov in risb priporočamo CDR format (CorelDraw), saj so slike v njem vektorske in jih lahko pri končni obdelavi preprosto povečujemo ali pomanjšujemo.

Pri označevanju osi v diagramih, kadar je le mogoče, uporabite označbe veličin (npr. v, T itn.). V diagramih z več krivuljami mora biti vsaka krivulja označena. Pomen oznake mora biti razložen v podnapisu slike.

Za vse slike po fotografskih posnetkih je treba priložiti izvirne fotografije ali kakovostno narejen posnetek.

Preglednice

Preglednice morajo biti zaporedno oštevilčene in označene, v besedilu in podnaslovu, kot preglednica 1, preglednica 2 itn. V preglednicah ne uporabljajte izpisanih imen veličin, ampak samo ustrezne simbole. K fizikalnim količinam, npr. t (pisano poševno), pripišite enote (pisano pokončno) v novo vrsto brez oklepajev. Vse opombe naj bodo označene z uporabo dvignjene številke[1].

Seznam literature

Navedba v besedilu

Vsaka navedba, na katero se sklicujete v besedilu, mora biti v seznamu literature (in obratno). Neobjavljeni rezultati in osebne komunikacije se ne priporočajo v seznamu literature, navedejo pa se lahko v besedilu, če je nujno potrebno.

Oblika navajanja literature

V besedilu: Navedite reference zaporedno po številkah v oglatih oklepajih v skladu z besedilom. Dejanski avtorji so lahko navedeni, vendar mora obvezno biti podana referenčna številka.

Primer: »..... kot je razvidno [1,2]. Brandl and Blovsky [4], sta pridobila drugačen rezultat…«

V seznamu: Literaturni viri so oštevilčeni po vrstnem redu, kakor se pojavijo v članku. Označimo jih s številkami v oglatih oklepajih.

Sklicevanje na objave v revijah:

[1] Jelušič, P., Žlender, B. 2013. Soil-nail wall stability analysis using ANFIS. Acta Geotechnica Slovenica 10(1), 61-73.

Sklicevanje na knjigo:
[2] Šuklje, L. 1969. Rheological aspects of soil mechanics. Wiley-Interscience, London
Sklicevanje na poglavje v monografiji:
[3] Mitchel, J.K. 1992. Characteristics and mechanisms of clay creep and creep rupture, in N. Guven, R.M. Pollastro (eds.), Clay-Water Interface and Its Rheological Implications, CMS Workshop Lectures, Vol. 4, The clay minerals Society, USA, pp. 212-244..
Sklicevanje na objave v zbornikih konferenc:
[4] Brandl, H., Blovsky, S. 2005. Slope stabilization with socket walls using the observational method. Proc. Int. conf. on Soil Mechanics and Geotechnical Engineering, Bratislava, pp. 2485-2488.
Sklicevanje na spletne objave:
[5] Kot najmanj, je potrebno podati celoten URL. Če so poznani drugi podatki (DOI, imena avtorjev, datumi, sklicevanje na izvorno literaturo), se naj prav tako dodajo.

Podatki o avtorjih

Članku priložite tudi podatke o avtorjih: imena, nazive, popolne poštne naslove, številke telefona in faksa, naslove elektronske pošte. Navedite kontaktno osebo.

Sprejem člankov in avtorske pravlce

Uredništvo si pridržuje pravico do odločanja o sprejemu članka za objavo, strokovno oceno mednarodnih recenzentov in morebitnem predlogu za krajšanje ali izpopolnitev ter terminološke in jezikovne korekture. Z objavo preidejo avtorske pravice na revijo ACTA GEOTECHNICA SLOVENICA. Pri morebitnih kasnejših objavah mora biti AGS navedena kot vir.

Vsa nadaljnja pojasnila daje:

Uredništvo
ACTA GEOTECHNICA SLOVENICA
Univerza v Mariboru,
Fakulteta za gradbeništvo, prometno inženirstvo in arhitekturo
Smetanova ulica 17, 2000 Maribor, Slovenija
E-pošta: ags@um.si

INSTRUCTIONS FOR AUTHORS

Format of the paper

The paper should have the following structure:

- A Title, which adequately describes the content of the paper and should not exceed 80 characters;
- An Abstract, which should be viewed as a mini version of the paper and should not exceed 250 words. The Abstract should state the principal objectives and the scope of the investigation and the methodology employed; it should also summarise the results and state the principal conclusions;
- Immediately after the abstract, provide a maximum of 6 keywords;
- An Introduction, which should provide a review of recent literature and sufficient background information to allow the results of the paper to be understood and evaluated;
- A Theoretical section;
- An Experimental section, which should provide details of the experimental set-up and the methods used to obtain the results;
- A Results section, which should clearly and concisely present the data, using figures and tables where appropriate;
- A Discussion section, which should describe the relationships shown and the generalisations made possible by the results and discuss the significance of the results, making comparisons with previously published work;
- Conclusions, which should present one or more conclusions that have been drawn from the results and subsequent discussion;
- A list of References, which comprises all the references cited in the text, and vice versa.

Additional Requirements for Manuscripts

- Use double line-spacing.
- Insert continuous line numbering.
- The submitted text of Research Papers should cover no more than 18 pages (without Tables, Legends, and References, style: font size 12, double line spacing). The number of illustrations should not exceed 10. Results may be shown in tables or figures, but not in both of them.
- Please submit, with the manuscript, the names, addresses and e-mail addresses of four potential referees. Note that the editor retains the sole right to decide whether or not the suggested reviewers are used.

Units and abbreviations

Only standard SI symbols and abbreviations should be used in the text, tables and figures. Symbols for physical quantities in the text should be written in Italics (e.g. v, T, etc.). Symbols for units that consist of letters should

be in plain text (e.g. Pa, m, etc.).
All abbreviations should be spelt out in full on first appearance.

Figures

Figures must be cited in consecutive numerical order in the text and referred to in both the text and the caption as Fig. 1, Fig. 2, etc. Figures may be saved in any common format, e.g. BMP, JPG, GIF. However, the use of CDR format (CorelDraw) is recommended for graphs and line drawings, since vector images can be easily reduced or enlarged during final processing of the paper.

When labelling axes, physical quantities (e.g. *v*, *T*, etc.) should be used whenever possible. Multi-curve graphs should have individual curves marked with a symbol; the meaning of the symbol should be explained in the figure caption. Good quality black-and-white photographs or scanned images should be supplied for the illustrations.

Tables

Tables must be cited in consecutive numerical order in the text and referred to in both the text and the caption as Table 1, Table 2, etc. The use of names for quantities in tables should be avoided if possible: corresponding symbols are preferred. In addition to the physical quantity, e.g. *t* (in Italics), units (normal text), should be added on a new line without brackets.
Any footnotes should be indicated by the use of the superscript[1].

LIST OF references

Citation in text

Please ensure that every reference cited in the text is also present in the reference list (and vice versa). Any references cited in the abstract must be given in full. Unpublished results and personal communications are not recommended in the reference list, but may be mentioned in the text, if necessary.

Reference style

Text: Indicate references by number(s) in square brackets consecutively in line with the text. The actual authors can be referred to, but the reference number(s) must always be given:

Example: "... as demonstrated [1,2]. Brandl and Blovsky [4] obtained a different result ..."

List: Number the references (numbers in square brackets) in the list in the order in which they appear in the text.

Reference to a journal publication:
[1] Jelušič, P., Žlender, B. 2013. Soil-nail wall stability analysis using ANFIS. Acta Geotechnica Slovenica 10(1), 61-73.

Reference to a book:
[2] Šuklje, L. 1969. Rheological aspects of soil mechanics. Wiley-Interscience, London

Reference to a chapter in an edited book:
[3] Mitchel, J.K. 1992. Characteristics and mechanisms of clay creep and creep rupture, in N. Guven, R.M. Pollastro (eds.), Clay-Water Interface and Its Rheological Implications, CMS Workshop Lectures, Vol. 4, The clay minerals Society, USA, pp. 212-244.

Conference proceedings:
[4] Brandl, H., Blovsky, S. 2005. Slope stabilization with socket walls using the observational method. Proc. Int. conf. on Soil Mechanics and Geotechnical Engineering, Bratislava, pp. 2485-2488.

Web references:
[5] As a minimum, the full URL should be given and the date when the reference was last accessed. Any further information, if known (DOI, author names, dates, reference to a source publication, etc.), should also be given.

Author information

The following information about the authors should be enclosed with the paper: names, complete postal addresses, telephone and fax numbers and E-mail addresses. Indicate the name of the corresponding author.

Acceptance of papers and copyright

The Editorial Committee of the Slovenian Geotechnical Review reserves the right to decide whether a paper is acceptable for publication, to obtain peer reviews for the submitted papers, and if necessary, to require changes in the content, length or language.
On publication, copyright for the paper shall pass to the ACTA GEOTECHNICA SLOVENICA. The AGS must be stated as a source in all later publication.

For further information contact:

Editorial Board
ACTA GEOTECHNICA SLOVENICA
University of Maribor,
Faculty of Civil Engineering, Transportation Engineering and Architecture
Smetanova ulica 17, 2000 Maribor, Slovenia
E-mail: ags@um.si

NAMEN REVIJE

Namen revije ACTA GEOTECHNICA SLOVENICA je objavljanje kakovostnih teoretičnih člankov z novih pomembnih področij geomehanike in geotehnike, ki bodo dolgoročno vplivali na temeljne in praktične vidike teh področij.

ACTA GEOTECHNICA SLOVENICA objavlja članke s področij: mehanika zemljin in kamnin, inženirska geologija, okoljska geotehnika, geosintetika, geotehnične konstrukcije, numerične in analitične metode, računalniško modeliranje, optimizacija geotehničnih konstrukcij, terenske in laboratorijske preiskave.

Revija redno izhaja dvakrat letno.

AVTORSKE PRAVICE

Ko uredništvo prejme članek v objavo, prosi avtorja(je), da prenese(jo) avtorske pravice za članek na izdajatelja, da bi zagotovili kar se da obsežno razširjanje informacij. Naša revija in posamezni prispevki so zaščiteni z avtorskimi pravicami izdajatelja in zanje veljajo naslednji pogoji:

Fotokopiranje

V skladu z našimi zakoni o zaščiti avtorskih pravic je dovoljeno narediti eno kopijo posameznega članka za osebno uporabo. Za naslednje fotokopije, vključno z večkratnim fotokopiranjem, sistematičnim fotokopiranjem, kopiranjem za reklamne ali predstavitvene namene, nadaljnjo prodajo in vsemi oblikami nedobičkonosne uporabe je treba pridobiti dovoljenje izdajatelja in plačati določen znesek.

Naročniki revije smejo kopirati kazalo z vsebino revije ali pripraviti seznam člankov z izvlečki za rabo v svojih ustanovah.

Elektronsko shranjevanje

Za elektronsko shranjevanje vsakršnega gradiva iz revije, vključno z vsemi članki ali deli članka, je potrebno dovoljenje izdajatelja.

ODGOVORNOST

Revija ne prevzame nobene odgovornosti za poškodbe in/ali škodo na osebah in na lastnini na podlagi odgovornosti za izdelke, zaradi malomarnosti ali drugače, ali zaradi uporabe kakršnekoli metode, izdelka, navodil ali zamisli, ki so opisani v njej.

AIMS AND SCOPE

ACTA GEOTECHNICA SLOVENICA aims to play an important role in publishing high-quality, theoretical papers from important and emerging areas that will have a lasting impact on fundamental and practical aspects of geomechanics and geotechnical engineering.

ACTA GEOTECHNICA SLOVENICA publishes papers from the following areas: soil and rock mechanics, engineering geology, environmental geotechnics, geosynthetic, geotechnical structures, numerical and analytical methods, computer modelling, optimization of geotechnical structures, field and laboratory testing.

The journal is published twice a year.

COPYRIGHT

Upon acceptance of an article by the Editorial Board, the author(s) will be asked to transfer copyright for the article to the publisher. This transfer will ensure the widest possible dissemination of information. This review and the individual contributions contained in it are protected by publisher's copyright, and the following terms and conditions apply to their use:

Photocopying

Single photocopies of single articles may be made for personal use, as allowed by national copyright laws. Permission of the publisher and payment of a fee are required for all other photocopying, including multiple or systematic copying, copying for advertising or promotional purposes, resale, and all forms of document delivery.

Subscribers may reproduce tables of contents or prepare lists of papers, including abstracts for internal circulation, within their institutions.

Electronic Storage

Permission of the publisher is required to store electronically any material contained in this review, including any paper or part of the paper.

RESPONSIBILITY

No responsibility is assumed by the publisher for any injury and/or damage to persons or property as a matter of product liability, negligence or otherwise, or from any use or operation of any methods, products, instructions or ideas contained in the material herein.

9771854017001

University of Maribor

Faculty of Civil Engineering, Transportation Engineering and Architecture

www.fgpa.um.si

University of Ljubljana

Faculty of Civil and Geodetic Engineering

Faculty of Natural Sciences and Engineering

www.fgg.uni-lj.si

www.ntf.uni-lj.si

SLOVENSKO GEOTEHNIŠKO DRUŠTVO • SLOVENIAN GEOTECHNICAL SOCIETY

www.sloged.si

SLOVENSKO DRUŠTVO ZA PODZEMNE GRADNJE

SLOVENIAN SOCIETY FOR UNDERGROUND STRUCTURES

www.ita-slovenia.si